

NASA/TP-2002-211943



# Simulation Study of Impact of Aeroelastic Characteristics on Flying Qualities of a High Speed Civil Transport

*David L. Raney, E. Bruce Jackson, and Carey S. Buttrill  
Langley Research Center, Hampton, Virginia*

---

October 2002

## The NASA STI Program Office . . . in Profile

Since its founding, NASA has been dedicated to the advancement of aeronautics and space science. The NASA Scientific and Technical Information (STI) Program Office plays a key part in helping NASA maintain this important role.

The NASA STI Program Office is operated by Langley Research Center, the lead center for NASA's scientific and technical information. The NASA STI Program Office provides access to the NASA STI Database, the largest collection of aeronautical and space science STI in the world. The Program Office is also NASA's institutional mechanism for disseminating the results of its research and development activities. These results are published by NASA in the NASA STI Report Series, which includes the following report types:

- **TECHNICAL PUBLICATION.** Reports of completed research or a major significant phase of research that present the results of NASA programs and include extensive data or theoretical analysis. Includes compilations of significant scientific and technical data and information deemed to be of continuing reference value. NASA counterpart of peer-reviewed formal professional papers, but having less stringent limitations on manuscript length and extent of graphic presentations.
- **TECHNICAL MEMORANDUM.** Scientific and technical findings that are preliminary or of specialized interest, e.g., quick release reports, working papers, and bibliographies that contain minimal annotation. Does not contain extensive analysis.
- **CONTRACTOR REPORT.** Scientific and technical findings by NASA-sponsored contractors and grantees.
- **CONFERENCE PUBLICATION.** Collected papers from scientific and technical conferences, symposia, seminars, or other meetings sponsored or co-sponsored by NASA.
- **SPECIAL PUBLICATION.** Scientific, technical, or historical information from NASA programs, projects, and missions, often concerned with subjects having substantial public interest.

**TECHNICAL TRANSLATION.** English-language translations of foreign scientific and technical material pertinent to NASA's mission.

Specialized services that complement the STI Program Office's diverse offerings include creating custom thesauri, building customized databases, organizing and publishing research results . . . even providing videos.

For more information about the NASA STI Program Office, see the following:

- Access the NASA STI Program Home Page at <http://www.sti.nasa.gov>
- Email your question via the Internet to [help@sti.nasa.gov](mailto:help@sti.nasa.gov)
- Fax your question to the NASA STI Help Desk at (301) 621-0134
- Telephone the NASA STI Help Desk at (301) 621-0390
- Write to:  
NASA STI Help Desk  
NASA Center for AeroSpace Information  
7121 Standard Drive  
Hanover, MD 21076-1320

NASA/TP-2002-211943



# Simulation Study of Impact of Aeroelastic Characteristics on Flying Qualities of a High Speed Civil Transport

*David L. Raney, E. Bruce Jackson, and Carey S. Buttrill  
Langley Research Center, Hampton, Virginia*

National Aeronautics and  
Space Administration

Langley Research Center  
Hampton, Virginia 23681-2199

---

October 2002

The use of trademarks or names of manufacturers in this report is for accurate reporting and does not constitute an official endorsement, either expressed or implied, of such products or manufacturers by the National Aeronautics and Space Administration.

---

Available from:

NASA Center for AeroSpace Information (CASI)  
7121 Standard Drive  
Hanover, MD 21076-1320  
(301) 621-0390

National Technical Information Service (NTIS)  
5285 Port Royal Road  
Springfield, VA 22161-2171  
(703) 605-6000

# Contents

Nomenclature.....	vii
Summary .....	1
Introduction.....	1
Test Objectives and Approach .....	2
Experimental Design and Apparatus .....	3
Aeroelastic HSCT Simulation Model.....	3
General Configuration Description, Propulsion, and Gear Models.....	3
Dynamic Aeroservoelastic Model.....	4
Control Laws .....	4
Variation of Dynamic Aeroelastic Characteristics .....	5
Variation of Structural Stiffness .....	5
Variation of Modal Damping.....	6
Elimination of Control Excitation of Selected Modes .....	7
Elimination of DASE Visual Cues .....	8
Variation of Turbulence Level.....	8
Test Matrix and Evaluation Procedure .....	8
Evaluation Maneuvers .....	9
Nominal Approach and Landing.....	9
IAG Lateral Offset Landing.....	9
Composite Flight Director Tracking.....	10
Data Collected.....	10
Transcribed Cooper-Harper Ratings and Comments .....	10
ASE Ride Quality and Control Influence Ratings.....	10
Digital Time Histories .....	11
Videotape Recordings .....	11
Langley Visual Motion Simulator.....	12
Cab Arrangement and Control Inceptor.....	12
Visual Projection and Display Formats .....	12
Motion Characteristics and Responses .....	12
Results and Discussion.....	14
Configuration Rankings by Pilot Preference Based on DASE Ratings.....	14
DASE Ride Quality Ratings Versus Pilot Preference.....	14
Control Influence Ratings Versus Pilot Preference.....	15
Biodynamic Coupling .....	15
Configuration Ranking Based on Cooper-Harper Ratings .....	17
Impact of Structural Stiffening.....	18
Impact of Display Compensation.....	18
Impact of Damping Level.....	19
Impact of Cancellation.....	19
Impact of Increasing Turbulence Level.....	20
Correlation of Ride Quality Ratings With Cockpit Vibration Spectra.....	20
Concluding Remarks .....	21
Appendix A— Test Pilot Biographies .....	60
Appendix B— Flight Cards.....	61
Appendix C— HUD Symbology .....	68
Appendix D— Flight Director Implementation for Task 3115 .....	74
References.....	78



## List of Tables

Table 1. Modal Frequencies for Stiffened Configuration.....	23
Table 2. Damping Levels and Targeted Modes for Damped Configurations .....	23
Table 3. Description of Modal-Cancellation Portion of Test Matrix .....	23
Table 4. Parametric Configurations Used in LaRC.3 Simulation Experiment .....	24
Table 5. Randomized Order of Configuration Evaluations .....	25
Table 6. CHRs Assigned by Test Pilots to Task Segment 1 for Each Configuration and Maneuver Task.....	26
Table 7. CHRs Assigned by Test Pilots to Task Segment 2 for Each Configuration and Maneuver Task.....	28
Table 8. CIRs and RQRs Provided by Test Pilots for Each Configuration and Maneuver Task.....	29
Table 9. Pilot Preference Ranking for Configuration Based on Average DASE CIR and RQR Scores.....	31
Table 10. Pilot Preference Ranking for Configuration Based on Average CHR Scores and Ranking Based on Average DASE Scores.....	32
Table 11. Results for Configurations With and Without Display Compensation.....	33
Table 12. Effect of Turbulence Variation on Average CHR, CIR, and RQR Values.....	33
Table D1. Flight-Path Angle and Heading Angle Command Sequences for Go-Around Plus Spiral Descent Task.....	74
Table D2. Flight-Path Angle and Heading Angle Command Sequences for Glide-Slope Intercept Task.....	75
Table D3. Flight-Path Angle and Heading Angle Command Sequences for Localizer Intercept Task.....	75
Table D4. Values of Time Constants.....	76

## List of Figures

Figure 1. Potential dynamic aeroelastic solutions that were examined. ....	34
Figure 2. Reference-H configuration arrangement. ....	34
Figure 3. Mode shapes and in vacuo frequencies for baseline dynamic aeroelastic model. ....	35
Figure 4. Migration of elastic mode poles with structural stiffness variation. ....	35
Figure 5. Migration of the dynamic elastic poles with varying damping level. ....	36
Figure 6. Frequency response of normal acceleration at pilot station to elevator inputs for various damping modes.....	36
Figure 7. Migration of transfer function zeros of dynamic elastic modes with elimination of control excitation. ....	37
Figure 8. Effect of eliminating control excitation of first symmetric and first antisymmetric modes on frequency response to elevator inputs. ....	37
Figure 9. Task definition and performance tolerances for nominal approach and landing. ....	38
Figure 10. Cooper-Harper flying qualities rating scale and definition of associated terminology. ....	39
Figure 11. Supplemental pilot rating scales developed to target pilot opinion of DASE effects.....	40
Figure 12. Composite video image recorded during all piloted evaluations. ....	40
Figure 13. External view of Langley Visual Motion Simulator.....	41
Figure 14. Frequency response of Langley Visual Motion Simulator as documented in reference 8. ....	42
Figure 15. Time history of commanded and actual vertical accelerations recorded during aeroelastic maneuver task. ....	43
Figure 16. Time history of commanded and actual lateral accelerations recorded during aeroelastic maneuver task. ....	44

Figure 17. Pilot preference ranking of parametric aeroelastic configurations based on DASE ratings.....	45
Figure 18. Average ride quality rating versus overall pilot preference ranking of parametric configurations.....	46
Figure 19. Average control influence rating versus overall pilot preference ranking of parametric configurations.....	46
Figure 20. Power-spectral analysis of biodynamic coupling incident for pilot B.....	47
Figure 21. Examples of biodynamic coupling incidents for pilots B, E, and C.....	48
Figure 22. Variation of average RQR with increasing structural stiffness.....	49
Figure 23. Variation of average CIR with increasing structural stiffness.....	49
Figure 24. Variation of average CHR with increasing structural stiffness.....	50
Figure 25. Variation of average RQR with increasing modal damping.....	50
Figure 26. Variation of average CIR with increasing modal damping.....	51
Figure 27. Impact of mode-canceling control on RQR.....	51
Figure 28. Impact of mode-canceling control on average CIR.....	52
Figure 29. Variation of average CHR with increasing damping and modal cancellation.....	52
Figure 30. Measured lateral accelerations from last 15 s of one example run performed with STIF2 configuration.....	53
Figure 31. Lateral vibration spectrum plot for example time history.....	54
Figure 32. Lateral vibration spectra plots for all lateral-offset time histories given RQR of 5.....	55
Figure 33. Lateral vibration spectral envelope based on maximum and minimum rms spectrum values for all runs given RQR of 5.....	56
Figure 34. Lateral vibration spectral envelopes for various RQR levels.....	57
Figure 35. Vertical vibration spectral envelopes for various RQR levels.....	58
Figure 36. Vertical vibration spectral envelopes based on ride quality rating plotted with ISO vertical vibration standard.....	59
Figure B1. Composite flight director tracking task.....	64
Figure B2. Nominal approach and landing.....	65
Figure B3. IAG lateral offset landing.....	66
Figure B4. Task rating card.....	67
Figure C1. HUD display.....	68
Figure C2. Bank angle scale with roll pointer and sideslip indicator.....	69
Figure C3. Heading scale-horizon line.....	69
Figure C4. Airspeed tape display.....	69
Figure C5. Altitude display tape.....	70
Figure C6. Velocity vector cluster.....	71
Figure C7. Pitch grid, reference waterline, and heading scale.....	71
Figure C8. ILS glide-slope and localizer displays.....	72
Figure C9. Analog-digital angle of attack display.....	72
Figure C10. Analog-digital acceleration tape display.....	72
Figure C11. Takeoff climb guidance system.....	73
Figure C12. Depressed glide-slope reference line.....	73
Figure C13. Tail-scrape bar.....	73
Figure C14. Reference waterline.....	73
Figure C15. Digital information selective display.....	73
Figure D1. Flight-path angle and heading angle time histories.....	74
Figure D2. Flight-path angle time history for glide-slope intercept task.....	75
Figure D3. Heading angle command time history for localizer intercept task.....	76
Figure D4. Flight director symbol.....	77

## Nomenclature

AGL	above ground level, ft
ALT	altitude
AN	antisymmetric
AOA	angle of attack, deg
ARI	aileron-rudder interconnect
A/T	autothrottle
Amp	amplitude
Avg	average
BDC	biodynamic coupling
CDU	cockpit display unit
C.G.	center of gravity, percentage of mean aerodynamic chord
CGI	computer generated imagery
CHR	Cooper-Harper rating
CIR	control influence rating
CRT	cathode-ray tube
Config	aircraft configuration
DASE	dynamic aeroservoelastic
DH	decision height
DIA	Denver International Airport
DME	distance measuring equipment (distance to runway threshold)
Dir	directional
EAS	equivalent airspeed
EPR	exhaust pressure ratio (shorthand for throttle position)
FAA	Federal Aviation Administration

F/D	flight director
fpm	feet per minute
ft/sec, ft/s	feet per second
G, <i>g</i>	acceleration due to gravity, 32.2 ft/s <sup>2</sup>
GEAR	landing gear position
GS	glide slope (part of instrument landing system)
GW	gross weight
HSCT	High Speed Civil Transport
HSD	horizontal situation display
HSR	high speed research
HUD	head-up display
IAG	Niagra Falls International Airport
IC	initial condition
ILS	instrument landing system
KEAS/m	equivalent airspeed, knots
kn, kts	knots
LaRC	Langley Research Center
Lat	lateral
LEF	leading-edge flaps, deg
LOC	localizer (part of instrument landing system)
M	Mach number
MAC	mean aerodynamic chord
MFC	final cruise mass condition
MIC	initial cruise mass condition
MTE	mission task element

MTOGW	maximum takeoff gross weight
MZFW	maximum zero-fuel weight
Max	maximum
Min	minimum
ms	millisecond
M13	Mass case 13—maximum taxi weight at forward C.G.
N/A	not applicable
NASA	National Aeronautics and Space Administration
$N_y$	lateral acceleration, $g$ units
$N_z$	normal acceleration, $g$ units
nmi	nautical miles
OM	outer marker
PF	pilot flying (evaluation pilot)
PFD	primary flight display
PIO	pilot-induced oscillation
PNF	pilot not flying (test engineer)
PSCAS	Pitch Stability and Control Augmentation System
ps	pilot station
$p/\beta$	lateral-directional control law
QSAE	quasi-static aeroelastic
R/C	rate of climb
RCB	ride comfort boundary
RQR	ride quality rating
Ref-H	Boeing Reference-H supersonic transport design
Rwy	runway

rms	root mean square
$R1, R2$	constant value during a run, either +1 or -1
SCAS	stability and control augmentation system
SPD	surface position display
SVS	synthetic vision system
SY	symmetric
ss	stall speed
TCA	Technology Concept Aircraft
TEF	trailing-edge flaps, deg
TIFS	total in-flight simulator
TOGA	takeoff go-around
Trim	indicates this parameter should be set to value required to achieve trimmed (unaccelerated) initial conditions
VFR	visual flight rules
VMS	Langley Visual Motion Simulator
$V_{app}$	approach speed
$V_{app1}$	approach speed, first approach segment
$V_{app2}$	approach speed, second approach segment
$V_{g/a}$	go-around speed
$V_{min}$	minimum operating speed
$V_{mo}, M_{mo}$	maximum operating speeds
$V_r$	takeoff rotation speed, knots
$V_{ref}$	reference speed
$V_1$	takeoff decision speed
$V_2$	takeoff safety speed

$X_{TD}$	number of feet from threshold
XVS	external vision system
$x$	longitudinal displacement of simulator cockpit
$Y_{TD}$	number of feet from centerline
$y$	lateral displacement of simulator cockpit
$z$	vertical displacement of simulator cockpit
$\alpha$	angle of attack
$\dot{\gamma}/V$	longitudinal control law
$\sigma$	standard deviation
$\phi$	bank angle, deg
$\psi$	yaw angle, deg

## Summary

A piloted simulation study was conducted in the Langley Visual Motion Simulator to address the impact of dynamic aeroservoelastic effects on flying qualities of a High Speed Civil Transport. The intent of the investigation was to determine the effectiveness of measures that can be taken to reduce the impact of aircraft flexibility on piloting tasks. Potential solutions examined consisted of increasing the frequency of elastic modes through structural stiffening, increasing the damping of elastic modes through active control, eliminating control effector excitation of the lowest frequency elastic modes, and eliminating visual cues associated with the elastic modes. The various configurations were evaluated by six test pilots who performed three types of maneuvers: a nominal approach and landing task, a landing that required correction for a lateral offset from the runway centerline, and a subsonic maneuvering task. During the investigation, several incidents were encountered in which cockpit vibrations due to elastic modes fed back into the control stick through involuntary motions of the pilot's upper body and arm. Structural stiffening and compensation of the visual display were of little benefit in alleviating the impact of elastic dynamics on piloting tasks, whereas increased damping and elimination of control effector excitation of the lowest frequency modes both offered great improvements when applied in sufficient degree.

## Introduction

As commercial transport aircraft designs become larger and more flexible, the impact of aeroelastic vibration on a vehicle's flight dynamics, flight control, and flying qualities increases in prominence. The consideration of such effects is likely to assume unprecedented significance in the design of a High Speed Civil Transport (HSCT). Constraints imposed by flight at supersonic speeds and the need for economical commercial operation will result in a very large but relatively light and slender HSCT design that will exhibit unusually low-frequency elastic modes. Great potential exists for such low-frequency structural dynamics to impact a pilot's ability to maneuver an aircraft, not only because of the degradation of ride quality but also because of adverse coupling between human pilot control dynamics and elastic modes of the aircraft structure.

A piloted simulation experiment was conducted in the Langley Visual Motion Simulator (VMS) facility to address the impact of dynamic aeroservoelastic (DASE) effects on flying qualities of the HSCT. An earlier piloted simulation assessment of a preliminary dynamic elastic HSCT model, which was also performed in the VMS, revealed that the flexible modes of the configuration caused great difficulty in performing several approach and landing tasks (ref. 1). The intent of the present investigation was to determine the effectiveness of measures that can be taken to reduce the impact of aircraft flexibility on such tasks.

Potential solutions examined were (1) increasing the frequency of the elastic modes by stiffening the aircraft structure, (2) active structural mode control to increase damping levels of various combinations of elastic modes, (3) active structural mode control to reduce pilot excitation of structural vibration, and (4) active synthetic vision system (SVS) compensation that would remove vibratory effects from the out-the-window scene as presented to the pilot. An HSCT simulation model containing six dynamic elastic modes was parameterized so that structural stiffness, modal damping, and other characteristics could be directly varied to represent the effect of each potential solution.

Twenty parametric configurations were evaluated by six test pilots representing the Federal Aviation Administration (FAA), The Boeing Company, National Aeronautics and Space Administration (NASA), and Veridian Corporation (formerly Calspan Corporation). The pilots evaluated each configuration with three types of maneuvers consisting of a nominal approach and landing task, a landing that required

correction for a lateral offset from the runway centerline, and a subsonic maneuvering task. Pilot ratings and cockpit vibration measurements were analyzed to provide insight regarding the effectiveness of each potential solution considered.

## **Test Objectives and Approach**

The primary objective of this investigation was to determine the effectiveness of measures that can be taken to reduce the impact of aircraft flexibility on piloting tasks for an HSCT. The secondary objective was to establish preliminary guidelines for designing a structural mode control system for an HSCT concept. An earlier simulation study that used a preliminary dynamic aeroelastic HSCT model was performed in the VMS. That study, referred to as the “LaRC.1 Piloted Simulation Assessment” in the High Speed Research Program, revealed an increase in the difficulty of approach and landing tasks when dynamic elastic modes were included in the simulation (ref. 1). The approach of the present investigation, referred to as the “LaRC.3 Aeroelastic Simulation Experiment” in the High Speed Research Program, was to parametrically vary certain aspects of the aeroelastic model to provide a simplified representation of several potential means of reducing the impact of dynamic aeroelasticity on piloting tasks. These potential solutions are depicted in figure 1 and described subsequently.

The first potential solution considered was to stiffen the vehicle structure. Structural stiffening tends to increase the modal frequencies and was approximated in the experiment by simply applying a stiffening factor to the frequencies associated with each DASE mode in the existing model. In vacuo frequencies of the dynamic elastic modes were multiplied by a given frequency ratio to represent a stiffer aircraft structure without altering the aerodynamic characteristics, mass characteristics, or in vacuo mode shapes of the configuration. This experimental approach therefore represents an idealization in which structural stiffness is added without the associated weight penalty. In this way we sought to gain insight into how stiff the structure must be to avoid difficulties in flying qualities caused by aeroelasticity.

The second potential solution was to increase modal damping, as could be achieved by employing an active mode suppression control system. The effect of such a system was approximated by increasing the damping of the existing elastic modes. By simply varying the damping ratios associated with selected elastic modes, the experiment examined the level of damping augmentation that an active mode suppression system must provide to restore acceptable flying qualities.

An idealized mode-canceling control system may also be envisioned that could use multiple control effectors at the tail, wing, and/or nose of the aircraft to pitch, roll, or yaw the vehicle while avoiding any excitation of the lowest frequency elastic modes. This mode-canceling system would represent a higher risk structural mode control concept, and it is the third potential solution considered in the investigation. The term “mode-canceling control” is used here to refer to input shaping for distributed control effectors that would avoid excitation of selected modes. The modal dynamics would remain, however, and would be subject to excitation by turbulence. Such a solution was approximately represented in the experiment by eliminating the ability of control effector inputs to excite the first symmetric and first antisymmetric modes. This approach provided information regarding the effectiveness of such a control concept and the relative importance of modal cancellation versus modal damping.

Compensation of the pilot’s visual display to eliminate perturbations due to structural vibration was the fourth potential solution considered in the investigation. This factor had been considered by Waszak, Davidson, and Schmidt in an earlier investigation where compensation of visual cues was used to eliminate bouncing of the horizon relative to the head-up display (HUD) due to dynamic elasticity (ref. 2).

Such compensation was found to have a positive effect on the pilots' opinion of a flexible B-1 aircraft simulation. A similar approach was represented in the existing aeroelastic HSCT simulation by simply eliminating the display perturbations due to aeroelasticity that were nominally included in the simulation.

By exploring the parametric variations just described, information was gained regarding the effectiveness of each approach and the degree to which it must be exercised in order to achieve the desired flying qualities. The means of approximating the various approaches by directly manipulating characteristics of the dynamic aeroelastic model permitted timely execution of an experiment that captured the fundamental effects of interest without having to design and implement candidate solutions.

## **Experimental Design and Apparatus**

The following sections of this report describe the mathematical aircraft simulation model, the test matrix of aeroelastic configurations, the piloted evaluation maneuvers and data collected, and the test procedures used in this experiment, as well as the motion-based simulation facility in which the evaluations were conducted.

### **Aeroelastic HSCT Simulation Model**

This experiment used a mathematical simulation of the so-called Cycle 3 version of the Boeing Reference-H (Ref-H) supersonic transport design (ref. 3). The model was published by Boeing Commercial Airplane Group in the summer of 1996 as the fourth major release in a series of increasingly detailed math models of the Ref-H configuration. The simulation model is based upon a combination of wind tunnel and computational fluid dynamics studies of the Ref-H design, ranging from low subsonic to Mach 2.4 supersonic wind tunnel studies.

The Cycle 3 release has improved fidelity over previous releases for aerodynamics, inertia, engines, landing gear, and actuation systems. The geometry of the Ref-H configuration was modeled in the simulation so that an accurate assessment of tail, nacelle, and wingtip strike incidents (inadvertent contact with ground) could be made during landing evaluations. In addition, finite-element structural models were used to predict the effect of steady flight loads upon aerodynamic stability derivatives, referred to as quasi-static aeroelastic (QSAE) effects. A key feature of the math model is the inclusion of DASE effects, which requires additional states to represent the dynamic flexing of the aircraft structure.

### ***General Configuration Description, Propulsion, and Gear Models***

The Ref-H vehicle design has a cranked-arrow planform, a conventional aft tail, and four underslung engines as shown in figure 2. The control devices include an independently actuated horizontal stabilizer and elevator, a three-segment rudder on a fixed vertical fin, eight trailing-edge flaperons (four per wing), four leading-edge flaps (two per wing), and a vortex fence device and two spoiler-slot deflectors on each wing. The elevator and horizontal tail are geared 2:1 by software in the current pitch control law. The fuselage has a maximum diameter on the order of 12 ft and is expected to carry approximately 300 passengers in three seating classes. The configuration is approximately 310 ft long with a wingspan of 130 ft.

The aircraft has an operating empty weight of 280 000 lb and a maximum taxi weight of 650 000 lb. Final cruise weight is expected to be approximately 385 000 lb. Maximum takeoff gross weight (MTOGW) is 650 000 lb and maximum zero-fuel weight (MZFW) is 350 000 lb. The center of gravity (C.G.) can vary from as far forward as 48.1 percent mean aerodynamic chord (MAC) to as far aft as

56.6 percent MAC. The tasks that were performed during this experiment used the final cruise weight of 384 862 lb with a C.G. at 53.2 percent MAC. The MAC is approximately 86 ft.

The Ref-H design includes two mixed-flow turbofan engines under each wing capable of 53 500 lb of gross thrust at takeoff. The axisymmetric inlet includes a translating centerbody spike to adjust the location of the shock wave during supersonic cruise. The outboard engines are located 31.2 ft from the centerline of the aircraft and are canted inward at 2.4° and upward 3.25° relative to the centerline of the aircraft. The inboard engines are located 17.4 ft from the centerline and are canted inward 1° and upward 5.7°.

The landing gear model contained in the Cycle 3 simulation consists of three sets of main gear, located just behind the C.G. envelope and arranged in left, center, and right sets of tires abreast of each other, and a nose gear. The main gear are located approximately 156 ft behind the cockpit and have a 17.7-ft stance. The nose gear is located approximately 56 ft behind the cockpit. Turning angle of the nose gear is 75°. The dynamic aeroelastic model used in this experiment cannot accurately represent the aeroelastic excitation that would occur during landing rollouts since there are no aeroelastic inputs for gear reaction forces. Aeroelastic perturbations at the cockpit station in response to gear touchdown also could not be accurately represented in this simulation. Therefore, pilots participating in this experiment did not consider the derotation or landing rollout in their aeroelastic evaluations.

### ***Dynamic Aeroservoelastic Model***

The dynamic aeroservoelastic portion of the model used in this simulation experiment contained six flexible aircraft modes, three symmetric (SY) and three antisymmetric (AN). The general mode shapes and their associated in vacuo frequencies are shown in figure 3. The aeroelastic model was based on a NASTRAN version of the Elfini 892-STR-E finite-element model. The model was generated at three different flight conditions: Mach 0.24 at a weight of 384 862 lb and a C.G. location of 53.2 percent MAC (landing), Mach 2.4 at a weight of 384 862 lb and a C.G. location of 53.2 percent MAC (final supersonic cruise), and Mach 0.24 at a weight of 649 914 lb and a C.G. location of 48.1 percent MAC (takeoff). Only the landing case was used in this experiment.

Dynamic aeroelastic modes contained in the model could be excited by turbulence and by control effector movements. No inputs from landing gear or engine pylon reaction forces were included in the model. Visual effects of the structural flexibility were provided in the simulation. The out-the-window scene presented on the cockpit monitors moved in relation to the HUD to represent the local perturbations in pitch and yaw at the pilot station. The overall effect was that the out-the-window scene appeared to bounce slightly both vertically and laterally in response to elastic excitation. These visual perturbations were typically approximately  $\pm 0.1^\circ$  during maneuvers performed with DASE effects.

### ***Control Laws***

The simulation model used control laws referred to as the  $\dot{\gamma}/V$  system in the longitudinal axis and the  $p/\beta$  system in the lateral-directional axis (refs. 4 and 5). These designs allowed the pilot to command flight-path rate with longitudinal stick inputs, roll rate with lateral stick inputs, and sideslip angle with rudder inputs. The longitudinal  $\dot{\gamma}/V$  system also included an autothrottle for airspeed regulation. When the stick was in or very near the neutral position (detent), the control laws maintained constant flight path, bank angle, and airspeed. These control laws were developed by The Boeing Company and were implemented in the Langley simulation model. As a whole, the combined control laws are referred to as the “stability and control augmentation system,” or SCAS. The SCAS is designed to provide stabilization

and control authority sufficient to perform the various maneuver tasks included in the LaRC.3 experiment. The design of the SCAS is somewhat optimistic in that it uses ideal feedback signals that reflect the motions of the mean body axis, a coordinate system that tracks the centroid of the vibrating aircraft structure. The aeroelastic dynamics therefore influenced stability of the closed-loop system only to the extent that the mean axis motions were influenced. In reality, local aeroelastic perturbations would influence sensor feedbacks, creating the potential for adverse interactions between elastic modes and the stability augmentation system. The potential for such interactions will present a major challenge to designers of the vehicle flight control systems. Further explanation of the control law strategy, architecture, and implementation is provided in references 4 and 5.

The need to operate within the existing airspace system mandates that the HSCT mix with subsonic traffic in the terminal environment and operate at subsonic speeds. This operation requires the design to fly most approaches on the “backside” of the drag curve; that is, an increase in power is required to trim for a reduction in airspeed. This unconventional throttle operation would probably necessitate extensive retraining of flight crews. However, the backside characteristic can be masked by using an autothrottle system. An autothrottle is an integral part of the Boeing  $\dot{\gamma}/V$  control law, and landings were always performed with the autothrottle active during this investigation.

The method of using available control surfaces for various flight control functions (control allocation) is based on the information provided in reference 3, along with actuator rate limits that were applied to the control surfaces. In the LaRC.1 simulation assessment, several incidents of pilot-induced oscillation (PIO) were encountered during tasks executed without DASE effects present. The data indicated that flaperon rate limiting was probably the cause of these incidents. Flaperon actuator rate limits of 50 deg/s were used during the LaRC.1 assessment, and the HSR Guidance and Flight Control Integrated Technology Team concluded that a rate limit of 90 deg/s might eliminate the PIO difficulty. Therefore, the (LaRC.3) simulation experiment described in this paper used the faster (90 deg/s) flaperon actuator rates.

## **Variation of Dynamic Aeroelastic Characteristics**

The baseline model was modified to allow parametric variation of several characteristics associated with the DASE effects. These modifications allowed the impact of structural stiffening, modal damping, modal cancellation, and visual cues to be evaluated from a piloted control standpoint.

### ***Variation of Structural Stiffness***

The effect of structural stiffening was represented in the simulation by increasing the frequencies of all six dynamic elastic modes included in the model. The in vacuo frequencies of the modes were multiplied by a given frequency ratio to represent a stiffer aircraft structure without altering the aerodynamic characteristics, mass characteristics, or in vacuo mode shapes of the configuration. This experimental approach therefore represents an idealization in which structural stiffness is added without the associated weight penalty. The representation of structural stiffening by directly manipulating the model in this fashion was clearly approximate, but was sufficient to capture the basic effect. Frequency ratios of 1.0 (BASE0 configuration), 1.16 (STIF1 configuration), 1.36 (STIF2), and 1.60 (STIF3) were chosen. This selection produced frequencies for the first symmetric bending mode of 1.25, 1.45, 1.70, and 2.0 Hz. The corresponding stiffness increases for the STIF1, STIF2, and STIF3 configurations are 35, 85, and 156 percent, respectively. The method of increasing modal frequency without modifying mode shape assumes that the stiffness increase is applied uniformly throughout the entire aircraft structure. The resulting frequencies of all six modes for each configuration are shown in table 1.

Linearized models of the dynamic aeroelastic simulation were produced for each stiffness condition. Migration of the elastic poles of the linear model that occurred as the stiffness level was varied is shown in figure 4. The total range of stiffness variation probably extends beyond the conditions that would be physically practical for this design because of weight penalties associated with producing the stiffer structure. The *STIF1* condition, with a frequency of 1.45 Hz for the first symmetric mode, was deemed most representative of the actual design because the original finite-element structural model was considered to have slightly underpredicted stiffness of the overall configuration.

The original baseline aeroelastic configuration (*BASE0*) had a first symmetric fuselage bending mode at 1.25 Hz in the final cruise weight condition. But work with the more mature Technology Concept Aircraft (TCA) finite-element structural model indicated that the first mode frequency was likely to be closer to 1.45 Hz at the final cruise weight condition and that this frequency was more likely to be representative of the actual aircraft. For this reason, the *STIF1* configuration was used as a baseline condition for all other parametric variations and is referred to as the “modified baseline” configuration. Time histories from the real-time simulation were used to verify that the parameterization method produced the desired effect.

### ***Variation of Modal Damping***

Ten parametric configurations were included in the portion of the test matrix that addressed the variation of modal damping levels. Damping levels applied to various modes, along with the associated configuration names, are shown in table 2. This portion of the investigation actually targeted three related issues.

The first issue was the level of modal damping required to achieve acceptable pilot evaluations. Damping ratios of 0.07, 0.15, and 0.30 were selected based on feedback obtained during discussions with Boeing flight control researchers. The damping ratios of various modes contained in the model were set to these values for various configurations.

The second issue dealt with the frequency range of the modes to which these damping levels were applied. The intent was to gain insight into the relative importance of suppressing only the first fuselage bending modes as opposed to the first and second fuselage harmonics. In one variation, damping was applied only to elastic modes with frequencies less than 2 Hz. For the modified baseline configuration (*STIF1*), this frequency range included the first symmetric mode shape and the first antisymmetric mode shape shown in figure 3. The frequencies of these two modes for the *STIF1* configuration were 1.45 Hz (*SY1*) and 1.61 Hz (*AN1*). The configurations, *DAMP1*, *DAMP2*, and *DAMP3*, shown in table 2, set the damping ratios of these first two modes to 0.07, 0.15, and 0.30, respectively. In a second variation, damping was applied to elastic modes with frequencies less than 3 Hz. This range included the *SY1* and *AN1* mode shapes shown in figure 3. The configurations, *DAMP6*, *DAMP7*, and *DAMP8*, also shown in table 2, set the damping ratios of these four modes to 0.07, 0.15, and 0.30, respectively.

Figure 5 illustrates the pole migrations of the dynamic elastic modes as the various damping levels were applied in these two frequency ranges. The plots shown in figure 6 illustrate normal acceleration at the pilot station in response to elevator inputs and lateral acceleration at the pilot station in response to rudder inputs. These frequency response plots show the attenuation of the elastic response to control inputs that results from increased damping levels.

A third issue addressed by this portion of the investigation was the relative importance of damping symmetric modes versus antisymmetric modes. In both frequency ranges, a damping ratio of 0.3 was

applied to the symmetric modes alone and then the antisymmetric modes alone. The configuration entitled DAMP4 in table 2 applied a damping ratio of 0.30 to the first symmetric mode only, and the configuration entitled DAMP5 applied a damping ratio of 0.30 to the first antisymmetric mode only. Likewise, the configurations entitled DAMP9 and DAMP10 applied a damping ratio of 0.30 to the first two symmetric modes and first two antisymmetric modes, respectively.

Again, since the model was directly manipulated to produce desired damping levels, the representation of an active mode suppression system is approximate and lacks nonlinearities and additional filter dynamics that might be present in the actual system. But the representation is sufficient to capture the fundamental effects of the variations of damping level, targeted frequency range, and symmetric versus antisymmetric mode suppression.

### *Elimination of Control Excitation of Selected Modes*

Another portion of the test matrix examined the impact of modal cancellation, which refers to elimination of the control effector excitation of a particular DASE mode or modes. It is intended to represent the effect that would be produced by using command shaping together with multiple control effectors to allow the pilot to pitch, roll, or yaw the aircraft without exciting the specifically targeted modes. Canard and elevator inputs, for instance, could be appropriately proportioned and blended to pitch the vehicle without exciting the first fuselage-bending mode. In the lateral case, rudder and chin fin effectors may be used in combination to avoid excitation of the first antisymmetric mode. The modal dynamics would remain, however, and would be subject to excitation by turbulence.

An idealized representation of such a design was achieved by eliminating elements of the B matrix (the control effect matrix) in the dynamic aeroelastic model that represent the control effector excitation inputs to the first symmetric and first antisymmetric fuselage bending modes. Control deflections commanded by the pilot during evaluation maneuvers therefore could not excite these modes. Only the first symmetric and first antisymmetric modes were canceled in this fashion because cancellation of higher fuselage harmonics would probably require more control effectors. Table 3 shows the parametric conditions and associated configuration names for the portion of the test matrix that examined mode-canceling control.

The CANC1 configuration shown in table 3 consists of the STIF1 baseline with modal cancellation applied to the first symmetric and first antisymmetric bending modes. Mode-canceling configurations were also generated for each of the three damping levels so that the test matrix would include direct comparisons of cancellation on and off for each damping condition. In this regard, the configurations labeled CANC2, CANC3, and CANC4 in table 3 are directly comparable with DAMP6, DAMP7, and DAMP8 in table 2 (with damping ratios of 0.07, 0.15, and 0.30, respectively).

Representation of the mode-canceling control design by eliminating the elements of the B matrix in the dynamic aeroelastic model is inherently approximate since it cannot convey the effect of nonlinearities (such as control saturation or rate limiting) in the actual mode suppression. This investigation makes no attempt to examine the achievability or practical limitations of such a mode-canceling control approach, but instead only evaluates the merits of an ideal representation of such a design.

Figure 7 illustrates the migration of transfer function zeros that result from elimination of the control effector excitation elements of the B matrix in the dynamic aeroelastic model. Zeros associated with the canceled modes in the transfer function of pitch rate to elevator move very near the poles. The modal dynamics remain and are subject to excitation by turbulence or by coupling from other elastic modes.

The frequency response plots shown in figure 8 illustrate that the first symmetric and first antisymmetric modes can no longer be directly excited by control effector inputs for the canceled configurations. The slight response of symmetric mode 1 that remains is due to coupling with symmetric mode 2.

### ***Elimination of DASE Visual Cues***

In order to represent an ideally compensated display, the aeroelastic perturbations in the out-the-window scene produced by structural flexing were turned off. The conformality of the horizons on the HUD and the outside visual scene was thereby restored for the display-compensated configuration. This condition was used to represent idealized compensation of an external vision system (XVS) for dynamic elastic effects. The variation was performed for only one aeroelastic condition, the DAMP1 configuration. The configuration called DISP0 represents the visual perturbations off case of the DAMP1 aeroelastic configuration. Visual perturbations due to aeroelastic effects were included in all other configurations evaluated.

### ***Variation of Turbulence Level***

Variation of turbulence level was the final factor examined in this experiment. All tasks were flown with the standard Dryden Spectra Turbulence Model. For the majority of configuration and task evaluations, an rms turbulence level of 3 ft/s was used (light turbulence). But for two configurations, pilots also performed the nominal approach and landing task with rms turbulence levels of 4.5 ft/s (moderate) and 6.0 ft/s (heavy). It was hoped that these spot evaluations of selected configurations would provide insight into the variation of configuration acceptability that could be expected to result from increasing turbulence levels. The two configurations chosen for the turbulence level variation were the QSAE0 configuration (no dynamic aeroelastic effects) and the DAMP7 configuration (0.15 damping applied to modes 1–4). This moderately damped aeroelastic configuration was selected to provide a general representation of the variation in flight characteristics that could be expected with increasing turbulence levels.

### ***Test Matrix and Evaluation Procedure***

A complete list of the parametric configurations used in the LaRC.3 experiment is shown in table 4. The test matrix contains 20 parametric configurations that target the effects of structural stiffening, modal damping level, modal cancellation, and display filtering. Also included are four additional conditions corresponding to varying turbulence levels for the QSAE0 and DAMP7 configurations.

As noted earlier, one of the stiffened cases was used as a modified baseline for the majority of the evaluations. The first stiffened parametric configuration, STIF1, was used as the baseline configuration throughout this investigation as it was considered more representative of the actual aircraft design. The STIF1 configuration had the frequency of the first symmetric mode increased to 1.45 Hz with all other modes multiplied by the corresponding frequency ratio. Therefore the parametric variations on damping and modal cancellation, as well as the display compensation case, were applied to this modified baseline with a first symmetric mode at 1.45 Hz (STIF1) rather than the original baseline configuration with its first symmetric mode at 1.25 Hz (BASE0).

Although table 4 presents the complete list of parametric configurations evaluated in this experiment, it does not indicate the order in which the six test pilots evaluated these configurations. The order of evaluation of the 20 configurations was random and differed for each pilot. The pilots were not informed which configuration they were evaluating. The exception to this practice was the turbulence variation that occurred at the end of the experiment. Pilots were informed as to the configuration and the turbulence level for those evaluations. All other evaluations were performed with mild turbulence.

The randomized order of configuration evaluations for each of the six test pilots is shown in table 5. Each pilot flew and rated all three maneuver tasks (described in the following section) for a given configuration before proceeding to the next random configuration. Simulation sessions were arranged so that pilots spent no more than 2 consecutive hours in the cockpit at a time, twice a day, with a minimum of 2 hours between sessions. Pilots were briefed prior to their first simulation sessions regarding overall test objectives and evaluation procedures, and each pilot had been provided with a written test plan at least 1 week before participation in the experiment. The test plan described the objectives, procedures, maneuver tasks, and evaluation tools of this experiment. Brief summaries of the prior flight experiences of each evaluation pilot are provided in appendix A.

## **Evaluation Maneuvers**

Three maneuver tasks were evaluated by each pilot for the parametric configurations that are presented in table 4. The maneuvers included a nominal approach and landing, a lateral offset landing, and a subsonic flight director tracking task. The turbulence-variation portion of the test matrix shown in table 4 was evaluated only with the nominal approach and landing task after the pilot completed the random portion of the test matrix in which the 20 parametric configurations were evaluated.

### ***Nominal Approach and Landing***

A flight card showing the task definition and performance criteria for the nominal approach and landing (task 4020) is provided in appendix B. The task was initiated in level flight at an altitude of 1500 ft and an airspeed of 190 knots on course for a localizer intercept of 30°. The pilot used the instrument landing system (ILS) localizer and glide-slope displays on the HUD (shown in appendix C) to perform the approach. At a distance of 7 nmi from the runway, autothrottles were commanded to reduce airspeed to the final approach speed of 159 knots. The procedure for the nominal approach included an automatic reconfiguration of leading- and trailing-edge devices that was initiated at a gear altitude of 390 ft and executed over a period of 18 s. The impetus for this automatic flap reconfiguration is the trade-off between noise restrictions imposed in the terminal area and the desire to reduce the aircraft pitch attitude at touchdown. The nominal autoflap procedure therefore configured the aircraft for a low-speed–low-noise approach down to an altitude of 390 ft, at which point the vehicle passed a critical noise-measuring station. Flaps and leading-edge devices were then automatically commanded to a high-lift–low-pitch attitude setting of 0° for leading-edge flap and 30° for trailing-edge flap for the final flare and touchdown; this configuration reduced the potential for tail strike at touchdown. During this period, thrust was increased by approximately 12 percent and pitch attitude was reduced by approximately 6° to compensate for the flap change. During the approach and landing with autothrottles engaged, these changes occurred automatically. A sketch depicting the nominal landing task segment definitions and performance criteria is shown in figure 9. A flare cue was provided on the HUD during the final portions of the landing. The flare cue used the tuning that was defined during the so-called Ames.5 simulation experiment documented in reference 6.

### ***IAG Lateral Offset Landing***

The Niagra Falls International Airport (IAG) lateral offset landing (task 4069) was the most challenging of the three evaluation maneuvers. This task was initiated at an altitude of 750 ft with a 300-ft lateral offset and 580-ft longitudinal offset of the ILS approach glide slope from the nominal approach path. The pilot was directed to fly down the offset ILS glide slope to an altitude of 250 ft. At this point, the pilot not flying (PNF) called “correct,” and the pilot executed a descending lateral correction to reacquire the runway centerline. The pilot then executed the flare and attempted to achieve

touchdown within the tolerances required for desired performance. The first segment of this task covered the approach from an altitude of 750 ft to 50 ft and included the lateral correction maneuver. The second segment began at an altitude of 50 ft and included the flare and touchdown portions of the task. The task required an aggressive lateral maneuver due to the low altitude at which the correction was initiated. A flight card showing the task definition and performance criteria for the offset landing (task 4069) is provided in appendix B.

### ***Composite Flight Director Tracking***

The composite flight director tracking (task 3115) allowed the pilot to evaluate the ability to accurately maneuver the aircraft by following flight director commands. The flight director was path oriented rather than attitude oriented. Originally, it was envisioned that either a sum-of-sines algorithm or a filtered random signal would be used to drive the flight director motions, as was used in the flexible B-1 study described in reference 2. However, references 7 and 8 suggest that greater consistency among pilot ratings was obtained when the flight director behaved in a fashion that is more representative of actual flight maneuver segments. For this reason, the decision was to drive the flight director with a composite signal containing elements from various maneuver segments examined in previous HSCT simulations. These maneuver segments included the localizer capture from the nominal approach, glide-slope capture, a descending turn, and a rapid pull-up as found in the landing go-around tasks from reference 1. Flight path and track angle command segments from these tasks were combined with varying order and sign to produce a flight director behavior that was not easily anticipated but still representative of actual flight maneuver tasks. The task was performed with mild turbulence. A flight card showing the task definition and performance criteria for the composite flight director tracking (task 3115) is provided in appendix B. Details regarding the operation of the flight director and the computation of task performance metrics are presented in appendix D.

## **Data Collected**

### ***Transcribed Cooper-Harper Ratings and Comments***

Pilots used the familiar Cooper-Harper rating (CHR) scale shown in figure 10 to assign a flying qualities rating to each parametric configuration (ref. 9). The pilot's task performance, in terms of touchdown parameters, flight-director tracking accuracy, and other information concerning maximum deviation from target values, was presented on the pilot's head-down "scorecard" display in the cockpit immediately following each task. This information provided a basis for assessing whether desired or adequate performance tolerances were achieved, which helped the pilot to navigate through the Cooper-Harper decision tree.

Pilots rated the configurations immediately following execution of a particular maneuver task using the task rating card presented in appendix B. After completing a sufficient number of runs to rate a particular configuration for a given task, the test pilot's verbal responses to the task rating card were taped using a hand-held microcassette recorder in the cockpit. The recorded pilot comments were later transcribed and organized according to configuration. A complete listing of all transcribed pilot comments collected during this experiment is provided in reference 10.

### ***ASE Ride Quality and Control Influence Ratings***

In addition to CHRs, test pilots were asked to provide a numerical assessment of the extent to which dynamic elastic effects adversely impact their control inputs and comfort (ride quality). Two supplemental rating scales were designed for this experiment to target these issues independent of deficiencies that the pilot may have perceived in the SCAS. The aeroelastic ride quality rating (RQR) scale and

control influence rating (CIR) scale are shown in figure 11. It was important to obtain an independent rating of aeroelastic deficiencies separate from evaluation of the SCAS. For instance, if a pilot awarded the nominal landing task a CHR of 4 for a particular configuration, but provided a CIR of 1 and an RQR of 1, then we could conclude that the deficient CHR was due to pilot dissatisfaction with the SCAS and not with the aeroelastic characteristics of that particular configuration. Pilot feedback regarding the design of these scales was incorporated based on preliminary assessments performed prior to the start of the experiment.

The CIR scale bears further discussion. The scale was developed based on pilot comments from the earlier (LaRC.1) preliminary piloted assessment of dynamic aeroelastic effects. During that assessment, pilots sometimes indicated that they were “reducing the gain” or “backing off” on their control inputs to avoid excitation of the dynamic elastic modes. Several time histories from the LaRC.1 test suggested that the aeroelastic cockpit vibrations had sometimes corrupted the precision of pilot control inputs or even caused occasional involuntary stick inputs. For this reason, the control influence rating scale was developed to specifically address this issue in addition to the pilot comfort or ride quality issue. The rating scales shown in figure 11 were included on the task rating card used by the pilots during their verbal configuration evaluations performed in the cockpit immediately following the maneuvers.

The dynamic aeroelastic evaluation scales shown in figure 11 included ratings that could be awarded when the dynamic aeroelastic effects resulted in a loss of control or when the cockpit vibration environment motivated the pilot to abandon the evaluation. The test pilot could depress a trigger on the sidestick control inceptor to halt the simulation if the ride quality was severe enough to warrant task abandonment. In such instances, activation of the trigger switch immediately terminated the run and the test pilot awarded the configuration a DASE RQR of 6 as described on the scale shown in figure 11. Poor task performance or an imminent landing outside the desired touchdown box was not a valid reason for use of the task abandonment trigger switch.

### ***Digital Time Histories***

A digital record of selected simulation parameters was made for each run. These parameters included flight conditions, pilot control inputs, aircraft control effector responses, and parameters describing the responses of the dynamic aeroelastic model. Time histories of the simulation parameters were recorded at a sample rate of 20 Hz. Some of the recorded parameters were analyzed immediately following the run to generate the information concerning maximum deviation from target values that was presented on the pilot’s head-down scorecard display.

### ***Videotape Recordings***

Four separate video channels were tiled together and recorded on VHS-C tape for all piloted evaluations. Figure 12 shows a single frame of the composite video image recorded during the experiment. The first channel (lower right of fig. 12) showed an exterior view of the simulator cab as it rotated and translated on its hexapod motion platform. The second channel (upper center of fig. 12) captured the view that was presented on the pilot’s forward cockpit monitor within the cab, which consisted of the HUD symbology superimposed upon the computer-generated out-the-window scene. The third channel (background image of fig. 12) contained a wide-angle video image of the interior of the cab as viewed from over the pilot’s right shoulder and behind the pilot and copilot’s seats. This angle captured the body motions of both the pilot and pilot not flying as they were jostled in their seats. The fourth video channel (lower left of fig. 12) provided a downward-looking view of the pilot’s hand on the sidestick control inceptor. Cockpit audio was also included on the videotapes. These video recordings proved extremely useful during postrun analysis of many simulated aeroelastic maneuver tasks.

## **Langley Visual Motion Simulator**

### ***Cab Arrangement and Control Inceptor***

The VMS, shown in figure 13, uses a synergistic hexapod motion system. The cockpit configuration at the time of this experiment included a left seat pilot flying (PF) station and a right seat PNF station. A throttle quadrant with four throttles was located between the pilot stations and included a cockpit display unit (CDU) that was used in this experiment to monitor and adjust various functions of the simulation. A fold-down jump seat was located behind and slightly to the left of the PNF station for an observer. Four-point harnesses were provided at all seats for motion operation.

The inceptor (control stick) used for all maneuvers performed during the LaRC.3 experiment was a McFadden left-handed side stick. The PF seat included a left-side armrest that was adjustable to provide appropriate forearm support for the left arm of the evaluation pilot.

### ***Visual Projection and Display Formats***

An Evans & Sutherland ESIG-3000 visual image generator was used to provide out-the-window scenery onto four mirror-beam-splitter monitors: a left- and a right-side view, and two forward views (one for each pilot). The terminal environment used for takeoff and landing work was a representation of the Denver International Airport (DIA). To assist the landing tasks, “desired” and “adequate” landing boxes were drawn on the image of the primary runway (DIA 35L), along with a target landing reference stripe to either side of the target touchdown aim point.

A simulated HUD was provided through an electronic video mix with the forward view. Appendix C contains a schematic of this HUD format used for the LaRC.3 experiment. Six other CRT displays were provided in the cockpit, arranged to the front and side of either pilot, in addition to the CDU. These displays provided a head-down primary flight display (PFD) and a horizontal situation display (HSD).

It is anticipated that an operational HSCT will include some enhanced XVS to eliminate the need to lower the nose for landing. Although the visual scene presented to the pilot during this experiment was not fully representative of an enhanced vision system, the display included symbology superimposed on the forward view that was similar to proposed XVS symbology. However, the forward field of view was shown at lower resolution and in a smaller field of view than that proposed for an operational XVS.

In addition, two specialized displays used in the LaRC.3 study were a surface position display (SPD) and a trim display. These displays were used to monitor the wing flap positions and the engine thrust levels, as well as to ensure proper configuration of the autothrottle and landing gear positions prior to each simulation run. A scorecard display was also provided at the completion of each run to indicate the numeric value of certain performance metrics achieved during the run to assist the evaluation pilot in assessing the configuration. The performance parameters described on the flight cards in appendix B were reported on the pilot’s scorecard display.

### ***Motion Characteristics and Responses***

The motion platform provides acceleration cues up to  $\pm 0.6g$  vertically within a 5.75-ft travel envelope; lateral and longitudinal acceleration limits are similar. The angular limits of the VMS are  $+30^\circ/-20^\circ$  pitch,  $\pm 32^\circ$  yaw, and  $\pm 22^\circ$  roll (positive pitch with the nose up).

Refinements were made to the motion drive algorithms to improve suitability of the simulator for representing the aeroelastic motion cues. Motion commands produced by the dynamic elastic portion of the aircraft model generally bypassed the motion washout filters to avoid any attenuation or delay of elastic vibration cues. Certain measures were also taken to allow implementation of the dynamic elastic model in the real-time simulation environment.

Figure 14 was taken from a 1973 report that documented the frequency response capabilities of the VMS (ref. 11). The input-output amplitude ratios for vertical and lateral sinusoidal inputs of 1.8 in. are shown, along with the resulting phase lag, for input frequencies from 0.1 to 12 rad/s. The 1.8-in. sinusoidal displacement amplitude seems particularly appropriate as data from the LaRC.1 experiment showed that pilot station displacements from the mean body axis on the order of  $\pm 2$  in. at the frequencies included in the aeroelastic model are sufficient to produce the 0.2g ringing observed during the piloted assessment. The frequency range of the dynamic elastic modes included in the LaRC.3 experiment is also shown in these plots (1.25 to 2.82 Hz).

The dynamic elastic portions of the model clearly caused the motion base to operate at the threshold of its capabilities. But at the lowest frequency bending modes for the BASE0 configuration (1.25 and 1.39 Hz), the motion base appears to give reasonable performance (amplitude ratio of 0.8 vertically and amplitude ratio of 1.0 laterally, with about  $15^\circ$  of phase loss). The next two dynamic elastic modes (at 2.01 and 2.13 Hz) still appear to be within the capabilities of the motion platform with about  $25^\circ$  of phase loss.

Figure 15 presents the normal accelerations at the pilot station that were commanded by the real-time simulation (dashed line) and those that were actually produced by the motion platform as measured by accelerometers (solid line). The time history was taken from a lateral offset landing task performed during the LaRC.3 experiment. The 60-s recording at the top of the figure shows that the magnitude of the two signals compared favorably, with the motion platform sometimes delivering incremental vertical acceleration cues as high as 0.4g and 0.6g. The two segments at the bottom of the figure provide a closer look at the frequency content and time delay between the two signals. The gross frequency content of the signals appears quite similar, although a time delay of approximately 150 ms is apparent between the command and the actual measured acceleration. The accelerometer measurements shown in the small-amplitude excerpt at the bottom left of the figure appear to contain an uncommanded high-frequency component at many of the reversal points in the time history. The cause of this small-amplitude aberration is uncertain, but it is most likely due to mechanical “slop” in structural components of the motion platform or mounting of the accelerometer package itself. This vibration is present throughout the time history, but its magnitude is small in comparison with the actual commanded accelerations.

Figure 16 gives lateral accelerations at the pilot station that were commanded by the real-time simulation (dashed line) and those that were actually produced by the motion platform as measured by accelerometers (solid line). The time history was taken from a lateral offset landing task performed during the LaRC.3 experiment. The lateral accelerations here appear similar to those of the vertical acceleration. The two segments at the bottom of the figure provide a closer look at the frequency content and time delay between the two signals. A time delay of approximately 160 to 170 ms is apparent between the command and the actual measured acceleration. This delay appears to be slightly longer than that observed in the vertical axis. The accelerometer measurements shown in the small-amplitude excerpt at the bottom left of the figure again contain an uncommanded high-frequency component at many of the inflection points in the time history. The amplitude ratio between the actual and commanded lateral accelerations is approximately 0.8. The extent to which these motion fidelity limitations impacted the assessment of dynamic aeroelastic effects is thought to be minimal, but their presence should be kept in

mind when interpreting the results of the experiment. Based on the initial dynamic aeroelastic implementation in the earlier LaRC.1 investigation (ref. 1) and the measured responses of the VMS platform, the facility appears to provide a reasonable representation of the lowest frequency modes included in the dynamic aeroelastic model.

## Results and Discussion

Time history data, subjective pilot comments, and pilot configuration ratings were examined in various combinations to provide some basic insights into the effectiveness of the differing approaches in dealing with the DASE effects studied in this experiment. The CHRs, CIRs, and RQRs of the pilots were compiled and plotted for each variation included in the test matrix. In general, CHRs did not seem to discriminate among configurations as clearly as the CIRs and RQRs, which specifically targeted DASE effects. A summary of all CHRs provided by the pilots for each configuration and task is shown in tables 6 and 7. A summary of all DASE CIR and RQR scores provided by the pilots for each configuration and task is shown in table 8. The following sections interpret the data shown in these tables.

### Configuration Rankings by Pilot Preference Based on DASE Ratings

The first approach to compiling the data was to formulate a pilot-preference ranking of the 20 parametric configurations based on the average DASE CIR and RQR scores assigned by pilots for all three maneuver tasks with a given configuration. This ranking is based only on the DASE CIR and RQR scores by using the scales shown in figure 11. (CHR's will be discussed later.) The ranking was developed simply by averaging all DASE ratings from all pilots for each configuration and then by arranging them in ascending order (larger average score meaning lower pilot preference). Pilot-preference ranking of the 20 configurations is shown in table 9 and is plotted in figure 17.

This simple approach to ranking the configurations passes a number of intuitive checks. First, the Ref-H baseline aeroelastic configuration (BASE0), with no structural stiffening or active mode suppression, was ranked the worst configuration—as one might expect. Also reassuringly, the rigid configuration without any dynamic aeroelastic effects (QSAE0, quasi-static elastic effects only) was ranked the best. Differentiation among configurations is greatest at the start of the ranking, in the most desirable region, and tapers off to near ties at the undesirable end of the spectrum. The stiffened cases without active mode suppression were all ranked poorly, suggesting that this approach was not effective at reducing the impact of dynamic elastic effects on piloting tasks. The configuration with the highest level of damping (0.3) applied to the greatest number of modes (four) and with modal cancellation (CANC4) was ranked the best of the aeroelastic configurations but was still very different from the rigid aircraft in terms of pilot ratings. The next best configuration was identical to this one with the exception of damping level, which was reduced to 0.15 (CANC3). The fourth ranked configuration had 0.3 damping on four modes, but had no cancellation (DAMP8). The order of ranking may provide some interesting insights regarding potential trades between mode-canceling control and additional damping. Another insight is gained when we compare the rankings of the configuration that had only symmetric modes damped (DAMP9, ranked 18th) with the configuration that had only antisymmetric modes damped (DAMP10, ranked 9th). It is clear that the pilots found the undamped antisymmetric motions to be more problematic than undamped symmetric motions. Many other interesting comparisons can be drawn from this configuration-ranking chart, which represents the most fundamental summation of the LaRC.3 experiment results.

### *DASE Ride Quality Ratings Versus Pilot Preference*

The overall ranking shown in figure 17 provides insight regarding the order of pilot preference for the 20 parametric configurations but does not indicate the point in ranking at which dynamic elastic

characteristics make the configuration unacceptable. Figure 18 attempts to address this issue by showing the average ride quality rating assigned by pilots for each configuration plotted against the overall pilot preference ranking from the previous figure. The subjective description of the ride quality rating assigned by pilots is shown adjacent to the ride quality axis along with shading to indicate the transition from acceptable to marginal to unacceptable configuration characteristics. On the basis of the average ride quality ratings, the first four configurations (QSAE0, CANC4, CANC3, and DAMP8) appear to be in or on the border of the acceptable ride quality region. Also shown in the plot are the maximum and minimum ride quality ratings assigned to the configurations. On the basis of the maximum rating, even the most highly mode-suppressed configuration (CANC4) provides only marginally acceptable ride quality at the pilot station. It should be noted that these ratings were provided during tasks performed with mild turbulence, and that the ride quality acceptability will probably degrade with increasing turbulence level. Figure 18 provides a subjective basis for the judgment of an acceptable level of mode suppression from a pilot's ride quality perspective. In this experiment, the damping level of 0.3 was based on the average ride quality rating.

### ***Control Influence Ratings Versus Pilot Preference***

Figure 19 provides an analogous ranking to figure 18 in terms of the CIR instead of RQR. The subjective description of the control influence rating assigned by the pilots is shown adjacent to the control influence axis, along with graduations to indicate the transition from acceptable to marginal to unacceptable configuration characteristics. The unacceptable threshold was placed at the point where cockpit vibrations impact the precision of voluntary control inputs. On the basis of the average control influence ratings, the first four configurations (QSAE0, CANC4, CANC3, and DAMP8) again lie within the acceptable region. On the basis of the maximum rating, the most highly mode-suppressed configuration (CANC4) again lies in the marginally acceptable region from a control influence perspective.

The border between acceptable and marginal control influence in this plot is somewhat arbitrary as it might be perfectly acceptable for the pilots to intentionally modify their control inputs to avoid excitation of the dynamic elastic modes as long as their ability to precisely control the aircraft is in no way hindered by this practice. However, recorded time histories of pilot stick deflections indicate that pilots were sometimes unaware that cockpit vibrations were in fact impacting their control inputs.

The potential for involuntary biodynamic feed-through of cockpit vibrations through the pilot's arm and back into the control inceptor due to aeroelastic effects of a supersonic transport was hypothesized in reference 12. The occurrence is involuntary and therefore may indeed be unnoticed by the pilot in minor instances. Use of the CIR scale shown in figure 19 requires the pilot to be aware of the occurrence, and therefore the CIRs may sometimes be optimistic. However, pilots did note a number of profound instances of frequent or sustained biodynamic feed-through of cockpit vibrations back into the control inceptor as indicated by the maximum CIRs shown in the figure. Frequent or sustained biodynamic feed-through of cockpit vibrations through the pilot's arm and back into the inceptor will be referred to as "biodynamic coupling" (BDC) in this report.

### **Biodynamic Coupling**

Figure 20 presents a power spectral analysis of a lateral offset landing run in which the pilot experienced BDC while flying the STIF1 (modified baseline) configuration with no additional damping or cancellation. The time history at the top of the figure shows lateral cockpit accelerations in  $g$  units (dashed line) and lateral stick deflections (solid line). Although the units on the two quantities differ, the scaling of  $\pm 1$  is convenient as it represents the maximum throw for lateral stick deflection and since

lateral acceleration commanded by the simulation remained in the range of  $\pm 1g$ . The plot in the lower left of the figure shows the power spectral density of lateral accelerations (dashed) and lateral stick deflections (solid) applied to a 6-s segment of the time history (from 39 to 45 s). The frequency spectrum of the pilot's voluntary control input time history during this period lies primarily below 1 Hz. The frequency spectrum of the lateral accelerations at the pilot station shows some content at the first antisymmetric mode frequency of 1.6 Hz and the second antisymmetric mode frequency of 2.5 Hz due to minor turbulence excitation of these structural modes. A clear separation exists between the frequency of the pilot's input spectrum and the frequency of cockpit accelerations due to the lateral elastic modes.

The power spectrum of a later 6-s segment of the time history (from 44 to 50 s) indicates the bulk of the pilot's input spectrum remains below 1 Hz, but it also shows some frequency content of the pilot's inputs in the range of the lateral elastic modes. Once the pilot begins to move the stick at the resonant frequency of the first antisymmetric structural mode, there is tremendous potential for the lateral mode to be excited by the control inputs and produce larger lateral accelerations at the pilot station. These lateral accelerations can move the pilot's frame in a fashion that produces involuntary control inputs that further excite the structural mode.

The third power spectrum plot is applied to a 6-s segment of the time history from 47 to 53 s. Here, the spectrum of the pilot's stick input exhibits a pronounced resonant peak at the frequency of the first antisymmetric structural mode. It is highly unlikely that the pilot inputs in this frequency range are voluntary (although they are within the pilot's voluntary bandwidth). Video footage of the cockpit interior and of the pilot's hand on the sidestick depicts a strong correlation between the involuntary motions of the pilot's upper body with the motions of his hand on the stick. A clear change in the character of the pilot's stick inputs is apparent in the time history shown in figure 20 and indicates a well-developed BDC incident as lateral accelerations feed through the pilot's frame and back into the control inceptor. The pilot would break the involuntary coupling loop if he released the stick, but he is in the midst of the flare and therefore unable to do so.

This type of adverse interaction between pilot and aircraft dynamics is not entirely unprecedented. A recent investigation performed at the Dryden Flight Research Center identified a similar phenomenon involving the use of a sidestick control inceptor (ref. 13) in the F-16XL that resulted in roll ratcheting during abrupt high-rate rolling maneuvers. Reference 14 documents these findings. Researchers produced an analytical model of the coupled system including dynamics of the pilot's frame and the control inceptor. The dynamic responses appeared quite similar to those encountered during the incidents of lateral BDC in the LaRC.3 experiment. The Dryden researchers in reference 14 identified a lateral resonant frequency of approximately 2.1 Hz for their combined pilot and control inceptor dynamical system (ref. 13).

Three of the six test pilots encountered BDC during various portions of the experiment. The phenomenon was usually encountered when test pilots flew the HSCT with no active suppression of the lateral structural modes. Encounters with BDC severely degraded the pilot's ability to control the aircraft, and sometimes resulted in termination of a run due to loss of control or uncomfortably high levels of cockpit vibration. Examples of BDC incidents for pilots B, E, and C are shown in figure 21. Power spectra of the pilot stick inputs for each case indicate a resonant peak at the frequency of the first antisymmetric elastic mode. Pilots B and E experienced BDC on many occasions and with many different configurations. Pilot C tended to experience less pronounced intermittent instances of biodynamic feed-through. Note that pilot C experienced coupling with the STIF3 configuration, which has its first antisymmetric mode at a higher frequency than the STIF1 baseline (2.2 Hz instead of 1.6 Hz).

The time histories shown for pilots B and E in figure 21 are for the DAMP9 configuration, which actually applies 0.3 damping to the symmetric modes but leaves the antisymmetric modes undamped. The presence of significant damping for symmetric modes did little to prevent the coupling because the lateral axis is far more prone to BDC for a number of reasons.

First, the pilot's seat tends to support the body longitudinally and vertically but not laterally; thus side-to-side accelerations are more difficult to resist. Symmetric modes produce vertical accelerations, whereas the stick input is fore and aft; therefore there is less tendency for the pilot's body motions to feed directly into the stick. However, antisymmetric modes produce lateral accelerations that feed directly into lateral stick deflections. A sidestick control inceptor was used in this experiment. The susceptibility of various inceptor types to biodynamic feed-through is a potential topic for future investigations. Certain measures to prevent BDC may be devised and incorporated during design of the control inceptor for the HSCT.

Another element of the control system implicated in the occurrence of BDC is the aileron-rudder interconnect (ARI). This is the control path whereby lateral stick displacements produce rudder deflections in proportion to aileron deflections to achieve turn coordination. But it is also the path whereby lateral cockpit vibrations may feed directly through the pilot-inceptor dynamics and back into rudder deflections; lateral elastic modes are further excited. Some provision may possibly be included in the design of the ARI to interrupt or prevent BDC.

To summarize, BDC is indicated when cockpit vibrations due to elastic modes feed directly through the pilot's arm and back into the control stick. The phenomenon is evidenced by a resonant peak in the power spectrum of the pilot's stick inputs at the frequency of one of the dynamic elastic modes. The tendency to couple with structural modes appears to increase when pilots tighten their grip on the stick, often in preparation for the flare as the aircraft nears the runway. The phenomenon is influenced by design of the control inceptor and control laws, piloting style, and probably even certain aspects of the pilot's physical stature.

The potential hazard posed by BDC would seem to suggest that certain elements of the HSCT active mode suppression control system, or at least some provision in the basic SCAS to prevent BDC, will need to be designated as flight critical. However, a final judgment regarding this issue should be made on the basis of evaluations performed with a high-fidelity dynamic aeroelastic model of the final aircraft configuration. The severity of the coupling sometimes observed indicates that some provision must be made to ensure that BDC is never encountered during either normal or reversionary operation of the HSCT flight control system.

### **Configuration Ranking Based on Cooper-Harper Ratings**

A configuration ranking similar to that shown in table 9 was produced with CHRs of the pilots instead of DASE ratings. The resulting configuration ranking is shown in table 10 along with the configuration ranking that was produced with the DASE scores. The overall ranking is similar, but the scores were much closer and there were a few ties. The outlined sections of the table indicate groupings of configurations that were ranked similarly. The CHR scale was not specifically designed to target DASE effects, but rather address overall control of the augmented flight dynamics provided by the SCAS. The DASE effects impacted CHRs from the perspective of increased pilot workload due to vibration environment, but the impact of DASE on pilot inputs and ride quality is not explicitly called out. Nevertheless, the results shown in table 10 indicate that good agreement exists between the two ranking methods in terms of general pilot preference for the various configurations. The summaries of all DASE ratings and the

summary of all CHRs shown in tables 6, 7, and 8 provide additional information regarding the pilots' ratings, such as whether a configuration was ranked poorly in the lateral-directional axis, or in the longitudinal axis, or in both.

## **Impact of Structural Stiffening**

Variation of average RQR and CIR with increasing structural stiffness is shown in figures 22 and 23. Maximum and minimum ratings for these configurations are also indicated on the plots. Structural stiffening did not appear to provide an effective solution to ride quality or control influence concerns posed by dynamic aeroelastic effects. The average and maximum CIR and RQR metrics fell in the unacceptable region for all structural stiffenings included in the experiment.

These findings are somewhat corroborated by results of the aforementioned investigation performed at Dryden Flight Research Center addressing biomechanically induced oscillations experienced on the F-16XL aircraft during rolling maneuvers (ref. 13). The Dryden researchers identified a lateral resonant frequency of approximately 2.1 Hz for their combined pilot and control inceptor dynamical system. We must assume that the LaRC.3 pilot and inceptor dynamical system possessed a resonant frequency in this same vicinity as figure 21 indicated lateral resonances at approximately 1.6 and 2.2 Hz for the LaRC.3 pilots. No stiffness variation examined in the LaRC.3 experiment was sufficiently high to remove all structural dynamics from this resonant frequency range. It is likely that no stiffnesses received favorable ratings because none were sufficient to raise the elastic dynamic frequencies beyond the region in which they tend to interfere with piloted flight. The ineffectiveness of increasing the frequencies of dynamic elastic modes through structural stiffening suggests that some form of active mode suppression control will be necessary.

The variation of CHRs with structural stiffening is shown in figure 24. Again, no significant improvement is apparent as a result of increasing modal frequencies through added stiffness. Each configuration received maximum CHRs that were in the Level 3 region.

## **Impact of Display Compensation**

No significant improvement due to aeroelastic display compensation was observed in this experiment in any pilot rating. To represent an ideally compensated display, the aeroelastic perturbations in the out-the-window scene produced by structural flexing were turned off. The conformality of the horizons on the HUD and the outside visual scene was thereby restored for the display-compensated configuration (DISP0). Table 11 shows the results for the configuration with display perturbations turned off and the analogous configuration with display perturbations turned on. In no instance did the pilot consistently report that the display compensation case improved the precision or ease with which maneuver tasks were performed. In most cases, the pilots did not indicate awareness that the configuration being evaluated was the display-compensated case. (Recall that the configurations were evaluated in random order and that pilots were not informed which condition was being evaluated.)

Although the display-compensated configuration was ranked slightly better than its counterpart without display compensation in terms of pilot preference, the difference in the DASE rating upon which this ranking was based is only 1 point (129 versus 130). This difference was clearly within the margin of error for the experiment, and pilot preference for the two configurations was a tie for all intensive purposes. The DAMP1 data set used only 0.07 damping for only the first two symmetric modes so that the aeroelastic vibrations experienced by the pilot were still rather vigorous. The increased workload resulting from aeroelastic vibrations likely meant that there was simply too much going on for pilots to notice

the effect of the display compensation and that the compensation provided no significant benefit for the aeroelastically active configuration.

### **Impact of Damping Level**

The variations in average RQR and CIR that resulted as damping was added to the dynamic elastic modes are shown in figures 25 and 26. The triangular symbols indicate the trend that resulted when damping was applied only to the first symmetric (SY1) and first antisymmetric (AN1) modes. The square symbols indicate the trend that resulted when damping was applied to the SY1, SY2, AN1, and AN2 modes. A clear improvement in RQRs and CIRs is apparent with increasing damping ratio. Recall that these configurations were evaluated in random order and that the order differed for each pilot; in no instance did a pilot experience a monotonic increase or decrease in damping. The figures also suggest that some additional improvement in ride quality resulted from damping the first four modes instead of only the first two. This difference is probably due to the second antisymmetric mode, which contributes significantly to the lateral accelerations experienced at the pilot station.

No definitive instances of biodynamic coupling were observed when the damping level applied to the first symmetric and first antisymmetric modes was 0.15 or greater. Several instances of biodynamic feed-through were noted for cases in which a damping ratio of 0.07 was applied to the first two and the first four elastic modes. Although the improvement in the average ratings with increasing damping is pronounced, the maximum damping level of 0.3 applied to the first four modes still produces average CIRs and RQRs that only lie on or near the border of the acceptable region. Table 8 includes the individual ratings awarded by each pilot for these configurations, along with the maximum, minimum, and standard deviation for each configuration.

### **Impact of Cancellation**

The impact of the mode-canceling control is shown in figures 27 and 28. These figures show the same data as the previous figures with the addition of mode-canceling control methods (indicated by the diamond symbols). Recall that modal cancellation in this experiment refers to the use of the canard and chin fin together with the elevator and rudder in a fashion that permits the pilot to pitch or yaw the vehicle without ever exciting the first symmetric or first antisymmetric modes. Therefore, the forward surfaces are enlisted for attitude control as well as mode suppression. The multisurface attitude control inputs must incorporate knowledge of the particular mode shapes being canceled. The modal dynamics remained, however, and were subject to excitation by turbulence. The mode-canceling methods evaluated in this experiment represented an ideal implementation of such a control scheme.

The use of modal cancellation in combination with damping applied to the first four dynamic elastic modes produced very good results. The average control influence ratings with modal cancellation shown in figure 28 were in the acceptable region for levels of damping as low as 0.07. No instances of sustained biodynamic feed-through were observed for any of the mode-canceling control methods. This result is probably attributable to the fact that mode-canceling control breaks the biodynamic coupling loop because inadvertent pilot inputs due to elastic vibrations can no longer excite elastic dynamics of the targeted modes.

The average RQRs also benefited from the use of mode-canceling control. Average RQRs for 0.15 and 0.30 damping with cancellation lie in or at the border of the acceptable region, and pilots perceived a ride quality improvement at all levels of damping. The benefit of using the forward surfaces for attitude control as well as damping is that it prevents the initial excitation of the structure from maneuver control inputs. Damping by itself is effective in attenuating the response of the structure to both turbulence

excitation and maneuver control excitation, but without cancellation the pilot still feels a large initial bump during any abrupt maneuver because the aircraft structure initially bends and snaps back while the vehicle pitches or yaws. In terms of the aircraft design, the use of modal cancellation suggests a need for true multifunction canards for attitude control and mode suppression rather than diminutive ride control vanes, which would only provide modal damping as in the B-1. The CHRs shown in figure 29 depict much less variation with increased damping and modal cancellation than did the RQRs or CIRs.

## **Impact of Increasing Turbulence Level**

Variation of turbulence level was the final factor examined in this experiment. For the majority of configuration and task evaluations, an rms Dryden spectral turbulence level of 3 ft/s was used (light turbulence). But for two configurations, the pilots also performed the nominal approach and landing task with rms turbulence levels of 4.5 ft/s (moderate) and 6.0 ft/s (heavy). These spot evaluations of selected configurations were intended to provide insight into the variation of configuration acceptability that could be expected to result from increasing turbulence levels. The two configurations chosen for the turbulence level variation were the QSAE0 configuration (no dynamic aeroelastic effects) and the DAMP7 configuration (0.15 damping applied to modes SY1, AN1, SY2, and AN2).

The results shown in table 12 were inconclusive regarding the impact of turbulence level on the various pilot rating metrics. The reason for this result is uncertain, for it seems likely that increasing the turbulence excitation amplitudes of the aircraft structure would almost certainly degrade the cockpit acceleration environment. The cockpit environment degradation due to increasing turbulence levels may have been perceived as insignificant in comparison with the degradation that was experienced as a result of the other parametric variations concurrently evaluated in this experiment.

## **Correlation of Ride Quality Ratings With Cockpit Vibration Spectra**

Figure 18 provides a subjective basis for the judgment of an acceptable level of mode suppression from a pilot's ride quality perspective. An attempt was made to correlate these subjective ratings of ride quality with a quantitative characterization of the vibration environment the pilots were experiencing at the time they provided the ratings. In this way we hoped to provide insight regarding allowable vibration levels at the pilot station in response to maneuver excitation of the aeroelastic modes to achieve acceptable ride quality. This analysis was performed only for the lateral offset landing task since that task produced the greatest range of RQRs.

Measured lateral accelerations from the last 15 s of one particular run performed with the STIF2 configuration are shown in figure 30. The pilot assigned this configuration an RQR of 5. This measured cockpit acceleration time history was analyzed to produce the rms lateral vibration spectrum plot shown in figure 31. The first and second antisymmetric mode frequencies for the STIF2 configuration are 1.89 and 2.90 Hz, as indicated in table 1. These frequencies correspond to peaks in the spectrum plot of measured accelerations shown in figure 31.

Similar vibration spectrum plots were generated for each run of the lateral offset landing task performed by each evaluation pilot for each configuration. These vibration spectra were then grouped according to the RQR that a particular run was given by the pilot, regardless of the configuration. Such a grouping is shown in figure 32. Each run shown in this figure was assigned an RQR of 5, but the runs were produced by different pilots flying different configurations. The plot contains runs for the BASE0 configuration as well as the STIF1, STIF2, DAMP1, DAMP2, and CANCEL configurations, and any others that were assigned an RQR of 5 by any pilot as indicated in table 8. The maximum and minimum rms accelerations at each frequency from the complete set of runs were then used to produce a vibration spectral

envelope that encompasses the characteristics of all runs awarded an RQR of 5. This spectral envelope is shown in figure 33. In this way we have attempted to characterize the range of vibration environments the pilots in our experiment judged to have an RQR of 5.

Similar spectral envelopes were produced for time histories that were awarded RQRs from 1 to 4 as needed. These lateral vibration spectral envelopes were then superimposed to produce the plot shown in figure 34. The same procedure was used to produce the collection of vertical vibration spectral envelopes shown in figure 35. The goal is to provide insight as to the acceptance by the pilots of different levels of cockpit vibration over the range of modal frequencies that was included in this experiment. Vibration levels for a given RQR score were higher longitudinally than laterally; this result agrees with precedents in the literature and suggests that lateral vibration is less easily tolerated than vertical vibration.

Because the vibration spectral envelopes shown in figures 34 and 35 are based on a limited number of evaluations with a limited number of pilots, we cannot definitively state that all future configurations with vibration spectra penetrating the RQR 5 envelope will be awarded an RQR of 5. Also, the envelopes overlap. Much of the RQR 4 envelope lies on top of portions of the RQR 5 envelope. However, the plots do provide a general indication of the amount of vibration considered acceptable at the particular modal frequencies included in the experiment. Note that these vibration levels were incurred during piloted maneuver excitation of the dynamic elastic modes in the presence of mild turbulence. The aeroelastic responses to control excitation during the maneuvers were the dominant factor in producing the vibrations.

An important caveat to note is that figures 34 and 35 do not provide information in the frequency range where there were no dynamics present in the models or in the motion cues to the pilot. The range of motion-base fidelity for elastic responses extends from about 2.5 to 3 Hz. The drop in vibration levels beyond 3 Hz shown in the spectral plots does not mean that pilot tolerances are extremely low at this frequency. It is more likely a result of the diminishing response of the motion platform in this frequency range. The plots shown in figures 34 and 35 simply indicate the range of vibration environments experienced at the time the pilots awarded a particular RQR during this experiment. The spectral envelopes for vertical vibrations from figure 35 are plotted with the vertical vibration standard from reference 14 in figure 36.

## **Concluding Remarks**

A piloted simulation experiment was conducted in the Langley Visual Motion Simulator (VMS) to address the impact of dynamic aeroservoelastic (DASE) effects on flying qualities of the High Speed Civil Transport. The intent of the experiment was to generate information regarding measures that can be taken to reduce the impact of aircraft flexibility on piloting tasks. Potential solutions examined consisted of increasing the frequency of the elastic modes, increasing the damping of various combinations of elastic modes, eliminating control effector excitation of the lowest frequency elastic modes, and eliminating visual cues associated with the elastic modes. The various configurations were evaluated by six test pilots who performed three types of maneuvers consisting of a nominal approach and landing task, a landing task that included a low-altitude correction for a lateral offset from the runway centerline, and a subsonic maneuvering flight director tracking task.

During the investigation, several profound incidents of biodynamic coupling (BDC) were encountered in which cockpit vibrations due to elastic modes fed back into the control stick through involuntary motions of the pilot's upper body and arm. The phenomenon is evidenced by a resonant peak in the power spectrum of the pilot's stick inputs at the frequency of one of the dynamic elastic modes. The

tendency to couple with structural modes in this fashion appears to increase when pilots tighten their grip on the stick, often in preparation for the flare as the aircraft nears the runway.

Two of the six evaluation pilots encountered pronounced BDC for aeroelastic configurations that had little or no additional damping of the elastic modes. A third pilot experienced occasional or frequent feed-through of vibrations back into the control stick that impacted the precision of his inputs for certain stiffened configurations when no additional damping was present. All pilots indicated that vibrations impacted the precision of their inputs at some point in the experiment. Pilots were far more prone to experience adverse coupling with antisymmetric modes rather than symmetric modes. Some of the most extreme instances of BDC occurred with the configurations in which a damping ratio of 0.3 was applied to the symmetric modes, whereas no additional damping was applied to the antisymmetric modes. The severity of the BDC phenomenon may have implications for control stick design and for the flight criticality of an active mode suppression control system.

The results of this investigation indicate that structural stiffening and compensation of the visual display were of little benefit in alleviating the impact of elastic dynamics on piloting tasks, whereas increased damping and elimination of control-effector excitation of the lowest frequency modes both offered great improvements when applied in sufficient degree. Structural stiffening did not provide effective relief from BDC for the two pilots who appeared most prone to this type of interaction. Damping levels of 0.15 applied to the first symmetric and first antisymmetric modes appeared sufficient to prevent BDC. When damping levels of 0.3 were applied to the first two symmetric and first two antisymmetric modes, average pilot ratings indicated that a borderline-acceptable configuration was achieved. With the addition of mode-canceling control, in which control effector excitation of the first symmetric and first antisymmetric modes was eliminated, the average pilot ratings indicate that an acceptable configuration was achieved.

Table 1. Modal Frequencies for Stiffened Configuration

Config	Frequency ratio	Stiffness ratio	Stiffness increase, percent	1st frequency, Hz		2d frequency, Hz		3d frequency, Hz	
				SY	AN	SY	AN	SY	AN
BASE0	1.00	1.00	0	1.25	1.39	2.01	2.13	2.70	2.82
STIF1	1.16	1.35	35	1.45	1.61	2.33	2.47	3.13	3.27
STIF2	1.36	1.85	85	1.70	1.89	2.73	2.90	3.67	3.84
STIF3	1.60	2.56	156	2.00	2.22	3.22	3.41	4.32	4.51

Table 2. Damping Levels and Targeted Modes for Damped Configurations

Config	Damping ratio	Modes damped
STIF1	Nominal	None
DAMP1	0.07	SY1, AN1
DAMP2	0.15	SY1, AN1
DAMP3	0.30	SY1, AN1
DAMP4	0.30	SY1
DAMP5	0.30	AN1
DAMP6	0.07	SY1, SY2, AN1, AN2
DAMP7	0.15	SY1, SY2, AN1, AN2
DAMP8	0.30	SY1, SY2, AN1, AN2
DAMP9	0.30	SY1, SY2
DAMP10	0.30	AN1, AN2

Table 3. Description of Modal-Cancellation Portion of Test Matrix

Config	Modes canceled	Damping ratio of remaining modes
STIF1	None	None
CANC1	SY1, AN1	None
CANC2	SY1, AN1	0.07
CANC3	SY1, AN1	0.15
CANC4	SY1, AN1	0.30

Table 4. Parametric Configurations Used in LaRC.3 Simulation Experiment

Modification	Config	Label	Description
None	1	QSAE0	Dynamic aeroelastic effects turned off
	2	BASE0	Baseline dynamic aeroservoelastic configuration
Display filtering	3	DISP0	DAMP1 with CGI DASE perturbations relative to HUD turned off
Structural stiffening	4	STIF1 <sup>a</sup>	First mode increased to 1.45 Hz; all others by same frequency ratio
	5	STIF2	First mode increased to 1.80 Hz; all others by same frequency ratio
	6	STIF3	First mode increased to 2.00 Hz; all others by same frequency ratio
Modal damping	7	DAMP1	Modal damping increased to 0.07 for modes SY1 and AN1
	8	DAMP2	Modal damping increased to 0.15 for modes SY1 and AN1
	9	DAMP3	Modal damping increased to 0.30 for modes SY1 and AN1
	10	DAMP4	Modal damping increased to 0.30 for mode SY1
	11	DAMP5	Modal damping increased to 0.30 for mode AN1
	12	DAMP6	Modal damping increased to 0.07 for modes SY1, AN1, SY2, and AN2
	13	DAMP7	Modal damping increased to 0.15 for modes SY1, AN1, SY2, and AN2
	14	DAMP8	Modal damping increased to 0.30 for modes SY1, AN1, SY2, and AN2
	15	DAMP9	Modal damping increased to 0.30 for modes SY1 and SY2
	16	DAMP10	Modal damping increased to 0.30 for modes AN1 and AN2
Modal cancellation	17	CANC1	Modes SY1 and AN1 control excitation eliminated
	18	CANC2	Modes SY1 and AN1 control excitation eliminated; remaining modes damped to 0.07
	19	CANC3	Modes SY1 and AN1 control excitation eliminated; remaining modes damped to 0.15
	20	CANC4	Modes SY1 and AN1 control excitation eliminated; remaining modes damped to 0.30
Turbulence variation	21	QSAE0	Moderate ( $\sigma = 4.5$ ) turbulence (nominal approach and landing only)
	22	QSAE0	Heavy ( $\sigma = 6.0$ ) turbulence (nominal approach and landing only)
	23	DAMP7	Moderate ( $\sigma = 4.5$ ) turbulence (nominal approach and landing only)
	24	DAMP7	Heavy ( $\sigma = 6.0$ ) turbulence (nominal approach and landing only)

<sup>a</sup>Modified baseline.

Table 5. Randomized Order of Configuration Evaluations

Config	Order of evaluation by—					
	Pilot A	Pilot B	Pilot C	Pilot D	Pilot E	Pilot F
1	20	6	10	6	9	14
2	3	4	18	18	6	4
3	15	5	20	16	10	6
4	8	15	6	19	1	18
5	16	13	16	4	14	1
6	5	10	2	14	3	12
7	12	16	14	11	12	19
8	11	7	15	15	11	17
9	6	2	19	7	7	10
10	21	9	9	10	15	5
11	9	11	13	8	13	2
12	4	3	4	17	20	8
13	18	19	11	9	18	13
14	13	14	3	1	16	9
15	10	1	7	20	17	16
16	14	17	17	2	8	7
17	22	12	8	12	2	15
18	7	20	12	13	19	20
19	2	18	1	3	5	11
20	17	8	5	5	4	3

Table 6. CHR's Assigned by Test Pilots to Task Segment 1 for Each Configuration and Maneuver Task

Config	Task ID	Task name	Longitudinal rating									Lateral-directional rating								
			Rating by pilot						Max	Avg	$\sigma$	Rating by pilot						Max	Avg	$\sigma$
			A	B	C	D	E	F				A	B	C	D	E	F			
1 QSAE0	1001	Nominal landing	3	2	3	3	2	4	4	2.8	0.75	3	3	3	3	2	4	4	3.0	0.63
	2001	Offset landing	3	4	3	3	4	4	4	3.5	0.55	3	4	3	3	4	5	5	3.7	0.82
	3001	Director tracking	3	2	3	3	3	4	4	3.0	0.63	3	3	3	4	3	4	4	3.3	0.52
2 BASE0	1002	Nominal landing	4	3	8	3	3	5	8	4.3	1.97	4	3	8	3	3	7	8	4.7	2.25
	2002	Offset landing	4	4	10	4	5	5	10	5.3	2.34	4	6	10	5	5	7	10	6.2	2.14
	3002	Director tracking	4	7	5	5	5	5	7	5.2	0.98	5	8	5	6	5	7	8	6.0	1.26
3 DISP0	1003	Nominal landing	3	2	3	3	3	6	6	3.3	1.37	3	2	3	3	3	6	6	3.3	1.37
	2003	Offset landing	3	4	5	4	5	6	6	4.5	1.05	3	4	4	5	5	7	7	4.7	1.37
	3003	Director tracking	3	3	4	4	4	5	5	3.8	0.75	4	3	4	5	4	6	6	4.3	1.03
4 STIF1	1004	Nominal landing	3	3	4	4	3	6	6	3.8	1.17	3	3	4	4	3	6	6	3.8	1.17
	2004	Offset landing	3	5	6	6	5	6	6	5.2	1.17	3	7	6	6	5	7	7	5.7	1.51
	3004	Director tracking	5	5	4	5	4	5	5	4.7	0.52	5	5	4	6	4	7	7	5.2	1.17
5 STIF2	1005	Nominal landing	3	3	3	3	3	5	5	3.3	0.82	3	2	3	3	3	7	7	3.5	1.76
	2005	Offset landing	3	3	6	5	5	5	6	4.5	1.22	3	2	5	6	5	7	7	4.7	1.86
	3005	Director tracking	3	3	4	4	4	5	5	3.8	0.75	4	6	5	6	4	7	7	5.3	1.21
6 STIF3	1006	Nominal landing	3	3	4	3	2	4	4	3.2	0.75	3	2	4	3	2	6	6	3.3	1.51
	2006	Offset landing	3	4	6	6	5	4	6	4.7	1.21	3	6	8	7	5	8	8	6.2	1.94
	3006	Director tracking	4	5	4	5	5	5	5	4.7	0.52	4	7	6	7	5	7	7	6.0	1.26
7 DAMP1	1007	Nominal landing	3	2	3	4	3	5	5	3.3	1.03	3	3	3	3	3	5	5	3.3	0.82
	2007	Offset landing	3	4	4	6	5	5	6	4.5	1.05	3	3	4	4	5	6	6	4.2	1.17
	3007	Director tracking	3	3	3	4	4	5	5	3.7	0.82	4	3	4	5	4	6	6	4.3	1.03
8 DAMP2	1008	Nominal landing	3	2	3	3	3	4	4	3.0	0.63	3	2	3	3	3	6	6	3.3	1.37
	2008	Offset landing	3	2	5	4	5	4	5	3.8	1.17	3	2	5	4	5	6	6	4.2	1.47
	3008	Director tracking	4	2	3	4	3	4	4	3.3	0.82	4	2	4	5	3	5	5	3.8	1.17
9 DAMP3	1009	Nominal landing	3	2	3	3	2	4	4	2.8	0.75	3	3	3	3	2	4	4	3.0	0.63
	2009	Offset landing	3	4	4	4	4	5	5	4.0	0.63	3	3	4	4	5	5	5	4.0	0.89
	3009	Director tracking	3	3	3	7	3	4	7	3.8	1.60	4	3	3	5	4	5	5	4.0	0.89
10 DAMP4	1010	Nominal landing	3	3	3	3	2	5	5	3.2	0.98	3	3	3	3	2	7	7	3.5	1.76
	2010	Offset landing	3	3	5	4	6	5	6	4.3	1.21	4	6	5	4	6	7	7	5.3	1.21
	3010	Director tracking	3	3	4	3	4	4	4	3.5	0.55	4	5	5	4	5	7	7	5.0	1.10

Table 6. Concluded

Config	Task ID	Task name	Longitudinal rating									Lateral-directional rating								
			Rating by pilot						Max	Avg	$\sigma$	Rating by pilot						Max	Avg	$\sigma$
			A	B	C	D	E	F				A	B	C	D	E	F			
11 DAMP5	1011	Nominal landing	3	2	3	4	3	7	7	3.7	1.75	3	2	3	3	3	4	4	3.0	0.63
	2011	Offset landing	3	3	5	4	5	7	7	4.5	1.52	3	3	4	4	5	6	6	4.2	1.17
	3011	Director tracking	3	2	4	4	4	6	6	3.8	1.33	3	3	3	5	4	6	6	4.0	1.26
12 DAMP6	1012	Nominal landing	3	3	3	4	3	5	5	3.5	0.84	3	2	3	3	3	5	5	3.2	0.98
	2012	Offset landing	3	3	5	4	5	5	5	4.2	0.98	3	2	5	4	5	7	7	4.3	1.75
	3012	Director tracking	3	2	3	4	4	5	5	3.5	1.05	4	3	4	4	4	7	7	4.3	1.37
13 DAMP7	1013	Nominal landing	3	2	3	3	2	4	4	2.8	0.75	3	2	3	3	2	4	4	2.8	0.75
	2013	Offset landing	3	4	4	3	5	5	5	4.0	0.89	3	3	4	4	5	5	5	4.0	0.89
	3013	Director tracking	3	3	3	4	4	4	4	3.5	0.55	4	5	4	5	4	5	5	4.5	0.55
14 DAMP8	1014	Nominal landing	3	2	3	3	2	4	4	2.8	0.75	3	2	3	3	2	4	4	2.8	0.75
	2014	Offset landing	3	3	4	5	4	5	5	4.0	0.89	3	3	4	5	4	5	5	4.0	0.89
	3014	Director tracking	3	3	3	4	4	5	5	3.7	0.82	4	3	3	5	4	5	5	4.0	0.89
15 DAMP9	1015	Nominal landing	3	3	6	6	3	4	6	4.2	1.47	3	5	5	6	4	7	7	5.0	1.41
	2015	Offset landing	3	5	6	5	6	4	6	4.8	1.17	3	7	6	6	7	7	7	6.0	1.55
	3015	Director tracking	3	3	3	4	4	4	4	3.5	0.55	4	7	4	7	4	6	7	5.3	1.51
16 DAMP10	1016	Nominal landing	3	3	4	3	3	5	5	3.5	0.84	3	2	4	3	3	4	4	3.2	0.75
	2016	Offset landing	3	4	5	6	5	7	7	5.0	1.41	3	5	4	4	5	5	5	4.3	0.82
	3016	Director tracking	3	3	4	5	4	5	5	4.0	0.89	4	6	4	4	3	5	6	4.3	1.03
17 CANC1	1017	Nominal landing	3	2	3	4	3	5	5	3.3	1.03	3	2	3	3	3	7	7	3.5	1.76
	2017	Offset landing	3	4	6	4	4	5	6	4.3	1.03	3	3	5	5	4	7	7	4.5	1.52
	3017	Director tracking	3	2	4	3	3	4	4	3.2	0.75	4	3	4	3	3	7	7	4.0	1.55
18 CANC2	1018	Nominal landing	3	2	3	3	2	4	4	2.8	0.75	3	2	3	3	2	4	4	2.8	0.75
	2018	Offset landing	3	3	4	4	5	5	5	4.0	0.89	3	2	4	5	4	5	5	3.8	1.17
	3018	Director tracking	3	2	3	3	3	5	5	3.2	0.98	3	3	3	4	3	5	5	3.5	0.84
19 CANC3	1019	Nominal landing	3	1	3	3	2	4	4	2.7	1.03	3	1	3	3	2	4	4	2.7	1.03
	2019	Offset landing	3	2	4	4	4	5	5	3.7	1.03	3	2	4	4	4	5	5	3.7	1.03
	3019	Director tracking	3	2	3	3	3	4	4	3.0	0.63	4	2	3	4	3	5	5	3.5	1.05
20 CANC4	1020	Nominal landing	3	2	3	3	2	4	4	2.8	0.75	3	2	3	3	2	4	4	2.8	0.75
	2020	Offset landing	3	2	4	3	5	4	5	3.5	1.05	3	2	4	3	4	5	5	3.5	1.05
	3020	Director tracking	3	2	3	4	3	4	4	3.2	0.75	3	3	3	5	3	6	5	3.8	1.03

Table 7. CHR's Assigned by Test Pilots to Task Segment 2 for Each Configuration and Maneuver Task

Config	Task ID	Task name	Longitudinal rating									Lateral-directional rating								
			Rating by pilot						Max	Avg	$\sigma$	Rating by pilot						Max	Avg	$\sigma$
			A	B	C	D	E	F				A	B	C	D	E	F			
1	1001	Nominal landing	4	4	3	5	3	5	5	4.0	0.89	4	3	3	3	3	3	4	3.2	0.41
QSAE0	2001	Offset landing	3	4	4	5	4	5	5	4.2	0.75	3	4	3	4	4	5	5	3.8	0.75
2	1002	Nominal landing	5	4	8	5	4	5	8	5.2	1.47	4	3	8	4	4	7	8	5.0	2.00
BASE0	2002	Offset landing	5	6	10	5	5	5	10	6.0	2.00	4	6	10	6	5	7	10	6.3	2.07
3	1003	Nominal landing	3	3	4	6	5	6	6	4.5	1.38	3	4	3	4	5	6	6	4.2	1.17
DISP0	2003	Offset landing	5	4	5	6	5	6	6	5.2	0.75	4	4	4	6	5	7	7	5.0	1.26
4	1004	Nominal landing	5	5	5	7	5	6	7	5.5	0.84	4	3	4	4	5	7	7	4.5	1.67
STIF1	2004	Offset landing	6	7	6	7	5	6	7	6.2	0.75	4	7	8	6	5	7	8	6.2	1.22
5	1005	Nominal landing	4	4	4	6	4	5	6	4.5	0.84	4	2	3	4	4	7	7	4.0	1.67
STIF2	2005	Offset landing	5	5	6	5	6	5	6	5.3	0.41	4	5	5	7	5	7	7	5.5	1.22
6	1006	Nominal landing	5	4	5	5	3	5	5	4.5	0.84	4	3	5	5	3	6	6	4.3	1.21
STIF3	2006	Offset landing	5	7	6	7	5	5	7	5.8	0.98	4	6	8	6	5	8	8	6.2	1.6
7	1007	Nominal landing	5	4	3	6	5	5	6	4.7	1.03	4	3	3	3	4	5	5	3.7	0.82
DAMP1	2007	Offset landing	5	5	5	6	5	5	6	5.2	0.41	4	4	4	4	5	5	5	4.3	0.52
8	1008	Nominal landing	4	4	3	4	4	5	5	4.0	0.63	4	2	3	3	4	6	6	3.7	1.37
DAMP2	2008	Offset landing	5	4	5	5	5	5	5	4.8	0.41	4	2	5	4	5	6	6	4.3	1.37
9	1009	Nominal landing	4	3	4	6	3	5	6	4.2	1.17	4	3	3	4	3	4	4	3.5	0.55
DAMP3	2009	Offset landing	5	6	5	7	4	5	7	5.3	1.03	4	3	5	4	5	4	5	4.2	0.75
10	1010	Nominal landing	5	4	5	5	5	5	5	4.8	0.41	4	4	8	5	5	7	8	5.5	1.64
DAMP4	2010	Offset landing	5	5	5	5	6	5	6	5.2	0.41	5	7	8	5	6	7	8	6.3	1.21
11	1011	Nominal landing	5	4	4	5	4	7	7	4.8	1.17	4	2	3	4	4	4	4	3.5	0.84
DAMP5	2011	Offset landing	5	4	5	5	5	7	7	5.2	0.98	4	3	4	4	5	6	6	4.3	1.03
12	1012	Nominal landing	4	5	4	6	5	5	6	4.8	0.75	4	3	3	5	5	5	5	4.2	0.98
DAMP6	2012	Offset landing	5	5	5	5	5	5	5	5.0	0.00	4	4	5	5	5	7	7	5.0	1.10
13	1013	Nominal landing	4	4	4	4	5	5	5	4.3	0.52	4	3	4	3	5	4	5	3.8	0.75
DAMP7	2013	Offset landing	4	5	4	5	5	5	5	4.7	0.52	4	3	5	5	5	4	5	4.3	0.82
14	1014	Nominal landing	3	3	3	5	3	5	5	3.7	1.03	3	2	3	4	3	2	4	2.8	0.75
DAMP8	2014	Offset landing	4	4	4	6	4	5	6	4.5	0.84	4	4	4	5	4	5	5	4.3	0.52
15	1015	Nominal landing	4	4	6	6	4	5	6	4.8	0.98	4	5	5	8	5	7	8	5.7	1.51
DAMP9	2015	Offset landing	4	8	6	5	6	5	8	5.7	1.37	4	7	6	6	7	7	7	6.2	1.17
16	1016	Nominal landing	4	3	5	6	5	5	6	4.7	1.03	3	2	4	5	4	4	5	3.7	1.03
DAMP10	2016	Offset landing	5	6	7	6	5	7	7	6.0	0.89	4	5	4	5	5	5	5	4.7	0.52
17	1017	Nominal landing	4	3	4	5	4	5	5	4.2	0.75	4	3	3	3	4	7	7	4.0	1.55
CANC1	2017	Offset landing	5	5	6	5	4	5	6	5.0	0.63	5	4	5	5	4	7	7	5.0	1.10
18	1018	Nominal landing	4	4	4	5	3	5	5	4.2	0.75	4	2	3	5	3	5	5	3.7	1.21
CANC2	2018	Offset landing	5	4	4	6	5	5	6	4.8	0.75	4	3	4	5	4	5	5	4.2	0.75
19	1019	Nominal landing	3	2	3	3	3	5	5	3.2	0.98	3	2	3	3	3	4	4	3.0	0.63
CANC3	2019	Offset landing	5	2	4	5	4	5	5	4.2	1.17	4	2	4	5	4	5	5	4.0	1.10
20	1020	Nominal landing	3	4	3	5	3	5	5	3.8	0.98	3	3	3	4	3	4	4	3.3	0.52
CANC4	2020	Offset landing	5	4	4	5	5	5	5	4.7	0.52	4	2	3	4	4	4	4	3.5	0.84

Table 8. CIRs and RQRs Provided by Test Pilots for Each Configuration and Maneuver Task

Config	Task ID	Task name	CIR									RQR								
			Rating by pilot						Max	Avg	$\sigma$	Rating by pilot						Max	Avg	$\sigma$
			A	B	C	D	E	F				A	B	C	D	E	F			
1 QSAE0	1001	Nominal landing	1	1	1	1	1	1	1	1.0	0	2	2	1	2	1	1	2	1.5	0.55
	2001	Offset landing	1	1	1	1	1	1	1	1.0	0	2	1	1	2	1	1	2	1.3	0.52
	3001	Director tracking	1	1	1	1	1	1	1	1.0	0	1	2	1	2	1	1	2	1.3	0.52
2 BASE0	1002	Nominal landing	3	2	5	3	3	3	5	3.2	0.98	5	5	5	4	4	5	5	4.7	0.52
	2002	Offset landing	3	2	6	3	4	3	6	3.5	1.38	5	5	6	4	5	5	6	5.0	0.63
	3002	Director tracking	3	2	5	4	4	3	5	3.5	1.05	5	5	5	5	5	5	5	5.0	0
3 DISPO	1003	Nominal landing	2	2	3	2	3	3	3	2.5	0.55	5	3	5	4	4	5	5	4.3	0.82
	2003	Offset landing	2	2	3	3	3	3	3	2.7	0.52	5	4	5	4	4	5	5	4.5	0.55
	3003	Director tracking	2	2	3	4	3	3	4	2.8	0.75	4	5	5	5	4	5	5	4.7	0.52
4 STIF1	1004	Nominal landing	3	2	4	3	4	3	4	3.2	0.75	5	5	5	5	5	5	5	5.0	0
	2004	Offset landing	3	4	4	3	4	3	4	3.5	0.55	5	5	5	5	5	5	5	5.0	0
	3004	Director tracking	3	2	3	3	4	3	4	3.0	0.63	5	5	5	4	5	5	5	4.8	0.41
5 STIF2	1005	Nominal landing	2	2	4	3	3	3	4	2.8	0.75	4	4	5	4	4	5	5	4.3	0.52
	2005	Offset landing	2	2	5	4	4	3	5	3.3	1.21	4	5	5	5	5	5	5	4.8	0.41
	3005	Director tracking	1	2	5	4	4	3	5	3.2	1.47	4	5	5	5	5	5	5	4.8	0.41
6 STIF3	1006	Nominal landing	3	3	4	3	2	2	4	2.8	0.75	5	4	5	4	3	4	5	4.2	0.75
	2006	Offset landing	2	3	5	3	3	3	5	3.2	0.98	5	5	5	5	4	5	5	4.8	0.41
	3006	Director tracking	3	2	5	4	4	3	5	3.5	1.05	5	5	5	5	5	5	5	5.0	0
7 DAMP1	1007	Nominal landing	3	2	2	3	3	2	3	2.5	0.55	5	4	4	3	4	5	5	4.2	0.75
	2007	Offset landing	3	2	3	3	3	3	3	2.8	0.41	5	4	5	4	5	5	5	4.7	0.52
	3007	Director tracking	2	2	3	3	3	3	3	2.7	0.52	4	5	5	5	5	5	5	4.8	0.41
8 DAMP2	1008	Nominal landing	2	2	2	2	3	2	3	2.2	0.41	4	3	4	3	4	4	4	3.7	0.52
	2008	Offset landing	2	2	3	2	3	2	3	2.3	0.52	3	4	5	3	5	4	5	4.0	0.89
	3008	Director tracking	2	2	3	2	3	2	3	2.3	0.52	4	5	5	4	5	4	5	4.5	0.55
9 DAMP3	1009	Nominal landing	1	1	1	2	2	2	2	1.5	0.55	3	2	3	3	2	3	3	2.7	0.52
	2009	Offset landing	1	2	2	3	2	2	3	2.0	0.63	3	3	4	5	3	3	5	3.5	0.84
	3009	Director tracking	1	2	1	3	2	2	3	1.8	0.75	3	3	3	5	3	3	5	3.3	0.82
10 DAMP4	1010	Nominal landing	3	2	5	2	3	3	5	3.0	1.1	5	4	5	3	5	5	5	4.5	0.84
	2010	Offset landing	3	2	5	2	4	3	5	3.2	1.17	5	5	5	3	5	5	5	4.7	0.82
	3010	Director tracking	2	2	5	3	3	3	5	3.0	1.1	4	5	5	5	4	5	5	4.7	0.52

Table 8. Concluded

Config	Task ID	Task name	CIR									RQR								
			Rating by pilot						Max	Avg	$\sigma$	Rating by pilot						Max	Avg	$\sigma$
			A	B	C	D	E	F				A	B	C	D	E	F			
11 DAMP5	1011	Nominal landing	3	2	4	2	3	3	4	2.8	0.75	5	4	5	4	5	5	5	4.7	0.52
	2011	Offset landing	3	2	4	2	3	3	4	2.8	0.75	5	4	5	3	5	5	5	4.5	0.84
	3011	Director tracking	2	2	3	2	3	3	3	2.5	0.55	4	4	5	5	5	5	5	4.7	0.52
12 DAMP6	1012	Nominal landing	3	3	2	3	3	2	3	2.7	0.52	5	5	5	4	4	4	5	4.5	0.55
	2012	Offset landing	3	3	4	3	3	3	4	3.2	0.41	5	5	5	4	5	5	5	4.8	0.41
	3012	Director tracking	2	3	4	3	3	2	4	2.8	0.75	4	5	5	5	4	5	5	4.7	0.52
13 DAMP7	1013	Nominal landing	2	1	2	1	2	2	2	1.7	0.52	4	3	4	2	2	3	4	3.0	0.89
	2013	Offset landing	2	2	3	1	2	2	3	2.0	0.63	4	4	5	2	2	3	5	3.3	1.21
	3013	Director tracking	1	2	2	2	2	2	2	1.8	0.41	4	5	4	3	2	4	5	3.7	1.03
14 DAMP8	1014	Nominal landing	1	2	1	2	2	2	2	1.7	0.52	3	2	2	2	2	3	3	2.3	0.52
	2014	Offset landing	1	2	1	3	2	2	3	1.8	0.75	3	2	2	4	2	3	4	2.7	0.82
	3014	Director tracking	1	1	1	2	3	2	3	1.7	0.82	2	3	2	3	3	3	3	2.7	0.52
15 DAMP9	1015	Nominal landing	2	3	4	4	3	3	4	3.2	0.75	5	5	5	6	5	5	6	5.2	0.41
	2015	Offset landing	2	4	5	3	4	3	5	3.5	1.05	4	6	5	4	5	5	6	4.8	0.75
	3015	Director tracking	2	2	4	4	3	2	4	2.8	0.98	4	5	5	5	5	5	5	4.8	0.41
16 DAMP10	1016	Nominal landing	2	2	3	3	3	2	3	2.5	0.55	3	3	4	4	4	5	5	3.8	0.75
	2016	Offset landing	2	2	4	3	3	3	4	2.8	0.75	3	5	5	4	5	5	5	4.5	0.84
	3016	Director tracking	1	2	3	3	3	2	3	2.3	0.82	4	4	4	4	5	4	5	4.2	0.41
17 CANC1	1017	Nominal landing	2	4	3	2	2	3	4	2.7	0.82	4	4	5	3	3	5	5	4.0	0.89
	2017	Offset landing	1	3	4	3	3	3	4	2.8	0.98	4	5	5	5	4	5	5	4.7	0.52
	3017	Director tracking	1	2	3	2	3	3	3	2.3	0.82	4	5	5	3	4	5	5	4.3	0.82
18 CANC2	1018	Nominal landing	1	1	3	2	1	1	3	1.5	0.84	4	2	4	2	2	3	4	2.8	0.98
	2018	Offset landing	1	1	3	2	1	1	3	1.5	0.84	4	2	4	2	3	3	4	3.0	0.89
	3018	Director tracking	1	1	2	1	2	1	2	1.3	0.52	4	2	3	2	3	3	4	2.8	0.75
19 CANC3	1019	Nominal landing	1	1	1	1	1	2	2	1.2	0.41	3	1	3	2	2	3	3	2.3	0.82
	2019	Offset landing	1	1	1	2	2	2	2	1.5	0.55	4	1	3	2	2	4	4	2.7	1.21
	3019	Director tracking	1	2	1	1	2	2	2	1.5	0.55	3	2	2	2	3	4	4	2.7	0.82
20 CANC4	1020	Nominal landing	1	1	1	1	2	1	2	1.2	0.41	2	1	3	2	2	3	3	2.2	0.75
	2020	Offset landing	1	1	1	1	2	1	2	1.2	0.41	2	1	3	2	2	3	3	2.2	0.75
	3020	Director tracking	1	1	1	1	2	1	2	1.2	0.41	2	2	3	2	2	2	3	2.2	0.41

Table 9. Pilot Preference Ranking for Configuration Based on Average DASE CIR and RQR Scores

Ranking	Avg CIR	Avg RQR	Config	Description
1	1.0	1.4	QSAE0	Dynamic aeroelastic effects turned off
2	1.2	2.2	CANC4	SY1 and AN1 control excitation eliminated; 0.3 damping of remaining modes
3	1.4	2.6	CANC3	SY1 and AN1 control excitation eliminated; 0.15 damping of remaining modes
4	1.4	2.6	DAMP8	Modal damping increased to 0.30 for modes SY1, AN1, SY2, and AN2
5	1.7	2.9	CANC2	SY1 and AN1 control excitation eliminated; 0.07 damping of remaining modes
6	1.8	3.2	DAMP3	Modal damping increased to 0.30 for modes SY1 and AN1
7	1.8	3.3	DAMP7	Modal damping increased to 0.15 for modes SY1, AN1, SY2, and AN2
8	2.3	4.1	DAMP2	Modal damping increased to 0.15 for modes SY1 and AN1
9	2.6	4.2	DAMP10	Modal damping increased to 0.30 for modes AN1 and AN2
10	2.6	4.3	CANC1	SY1 and AN1 control excitation eliminated
11	2.7	4.5	DISP0	Configuration DAMP1 with CGI DASE perturbations relative to HUD turned off
12	2.7	4.6	DAMP1	Modal damping increased to 0.07 for modes SY1 and AN1
13	2.7	4.6	DAMP5	Modal damping increased to 0.30 for mode AN1
14	2.9	4.7	DAMP6	Modal damping increased to 0.07 for modes SY1, AN1, SY2, and AN2
15	3.1	4.6	DAMP4	Modal damping increased to 0.30 for mode SY1
16	3.1	4.7	STIF2	First mode increased to 1.80 Hz; all others by same frequency ratio
17	3.2	4.7	STIF3	First mode increased to 2.00 Hz; all others by same frequency ratio
18	3.2	4.9	DAMP9	Modal damping increased to 0.30 for modes SY1 and SY2
19	3.2	4.9	STIF1	First mode increased to 1.45 Hz; all others by same frequency ratio
20	3.4	4.9	BASE0	Baseline dynamic aeroservoelastic configuration

Table 10. Pilot Preference Ranking for Configuration Based on Average CHR Scores and Ranking Based on Average DASE Scores

Ranking	Preference order based on CHR scores	Avg CHR	Preference order based on DASE scores	Avg CIR	Avg RQR
1	QSAE0	3.45	QSAE0	1.0	1.4
2	CANC4	3.48	CANC4	1.2	2.2
3	CANC3	3.52	CANC3	1.4	2.6
4	DAMP8	3.67	DAMP8	1.4	2.6
5	CANC2	3.70	CANC2	1.7	2.9
6	DAMP2	3.83	DAMP3	1.8	3.2
7	DAMP3	3.88	DAMP7	1.8	3.3
8	DAMP7	3.88	DAMP2	2.3	4.1
9	CANC1	4.10	DAMP10	2.6	4.2
10	DAMP5	4.10	CANC1	2.6	4.3
11	DAMP1	4.12	DISP0	2.7	4.5
12	DAMP6	4.20	DAMP1	2.7	4.6
13	DISP0	4.28	DAMP5	2.7	4.6
14	DAMP10	4.33	DAMP6	2.9	4.7
15	STIF2	4.43	DAMP4	3.1	4.6
16	DAMP4	4.67	STIF2	3.1	4.7
17	STIF3	4.88	STIF3	3.2	4.7
18	STIF1	5.07	DAMP9	3.2	4.9
19	DAMP9	5.12	STIF1	3.2	4.9
20	BASE0	5.42	BASE0	3.4	4.9

Table 11. Results for Configurations With and Without Display Compensation

Configuration name.....		DISP0 <sup>a</sup>	DAMP1 <sup>b</sup>
Display compensation .....		On	Off
DASE rating sum.....		129.0	130.0
Pilot preference ranking.....		11.0	12.0
RQR	Max.....	5.0	5.0
	Avg.....	4.5	4.6
	Min.....	3.0	3.0
	Sum.....	81.0	82.0
CIR	Max.....	4.0	3.0
	Avg.....	2.7	2.7
	Min.....	2.0	2.0
	Sum.....	48.0	48.0
CHR	Max.....	7.0	6.0
	Avg.....	4.3	4.1
	Min.....	2.0	2.0
	Sum.....	257.0	247.0

<sup>a</sup>0.07 damping applied to SY1 and AN1 modes.

<sup>b</sup>DAMP1 configuration without DASE display perturbations.

Table 12. Effect of Turbulence Variation on Average CHR, CIR, and RQR Values

Turbulence, ft/s (rms)	CHR		CIR		RQR	
	QSAE0	DAMP7	QSAE0	DAMP7	QSAE0	DAMP7
3.0	3.0	3.5	1.0	1.7	1.5	3.3
4.5	3.1	3.6	1.0	1.8	1.5	3.8
6.0	3.5	3.9	1.2	2.3	1.7	3.8

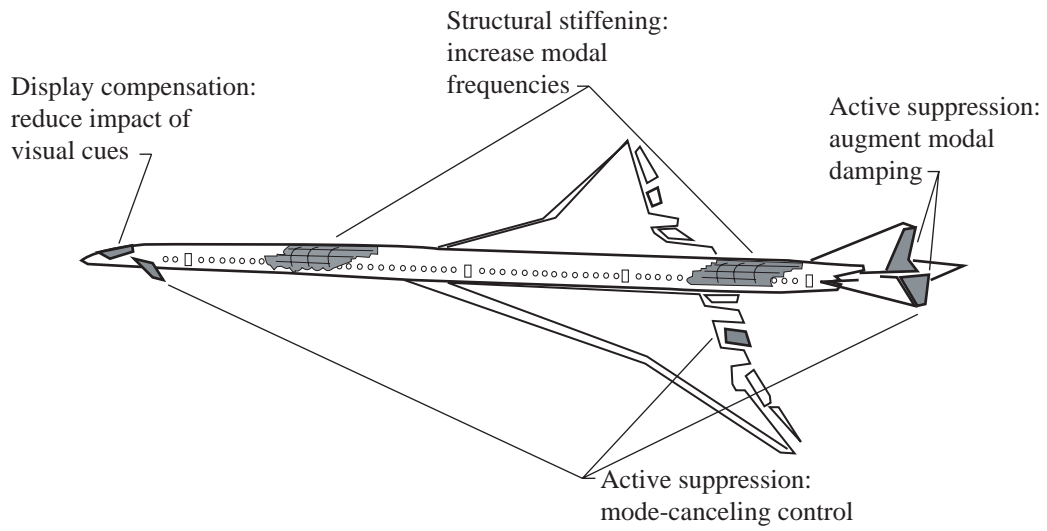


Figure 1. Potential dynamic aeroelastic solutions that were examined.

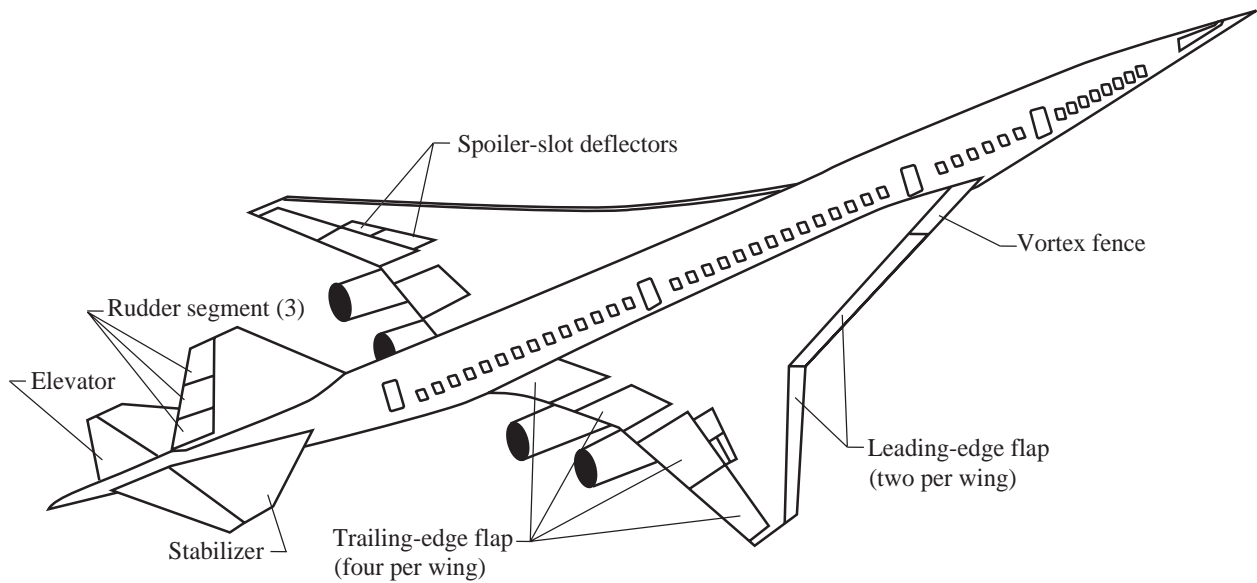


Figure 2. Reference-H configuration arrangement.

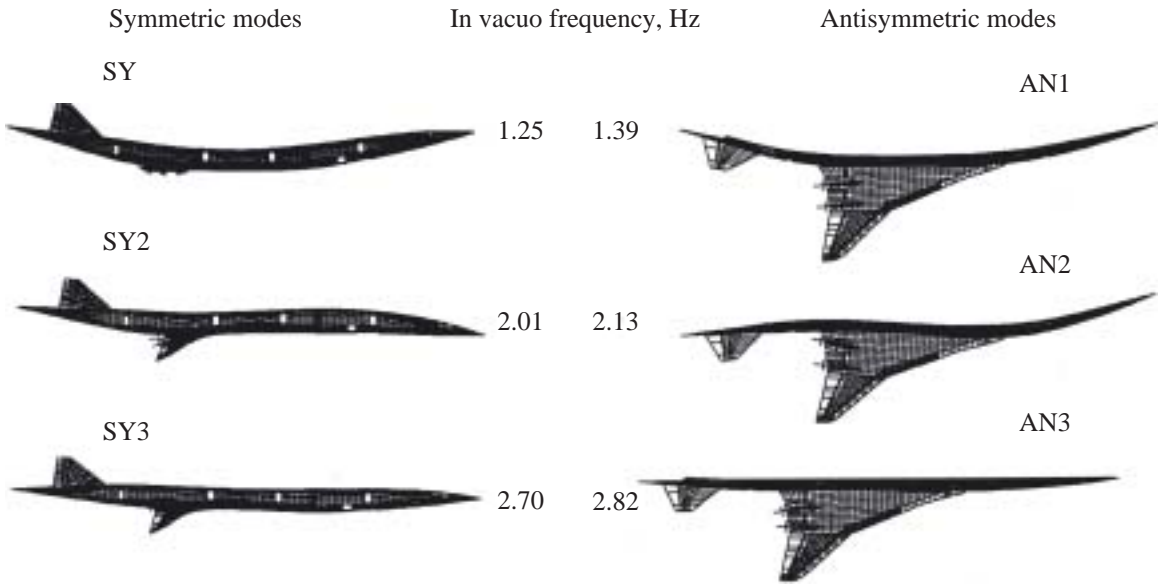


Figure 3. Mode shapes and in vacuo frequencies for baseline dynamic aeroelastic model.

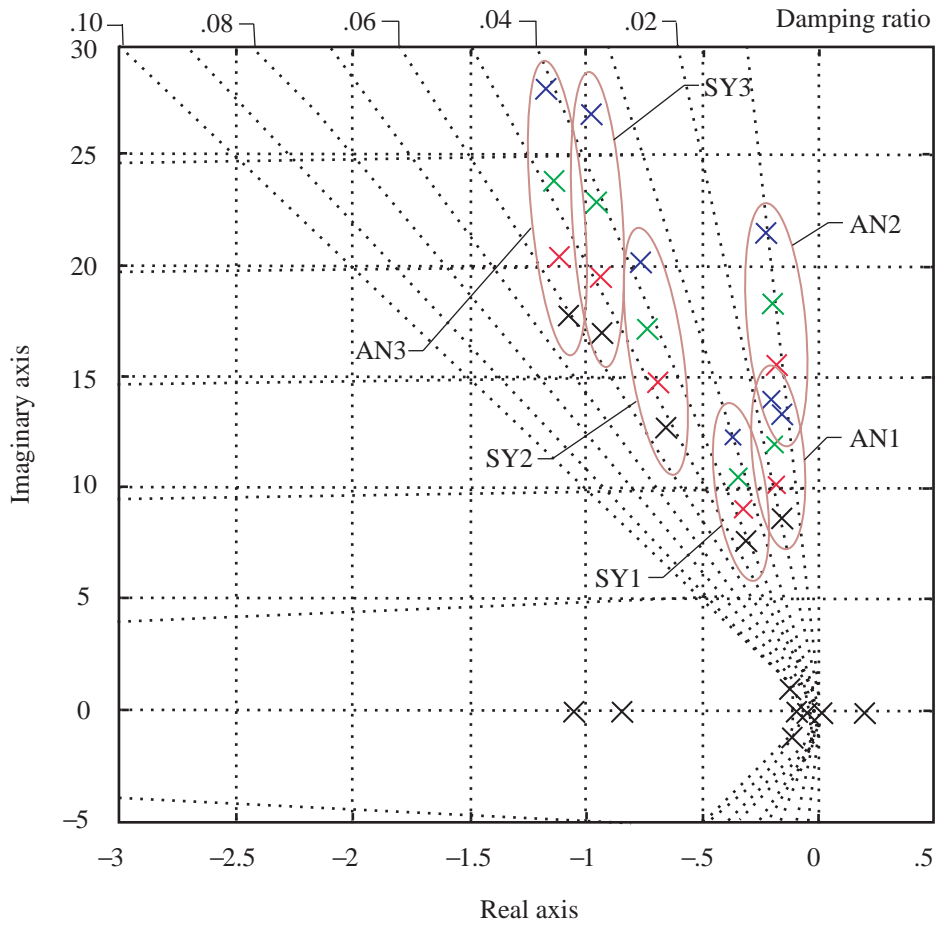


Figure 4. Migration of elastic mode poles with structural stiffness variation.

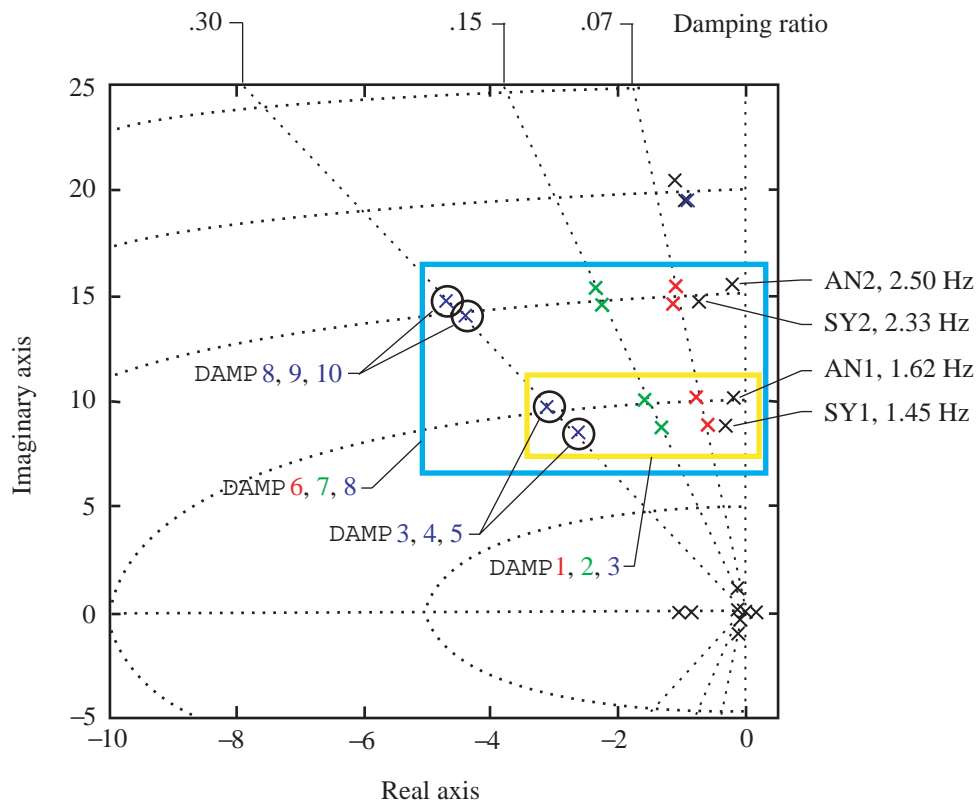


Figure 5. Migration of dynamic elastic poles with varying damping level.

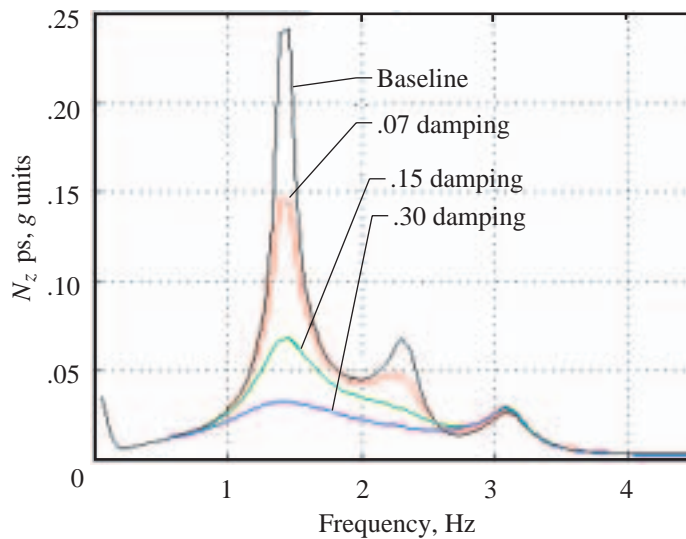


Figure 6. Frequency response of normal acceleration at pilot station to elevator inputs for various damping modes.

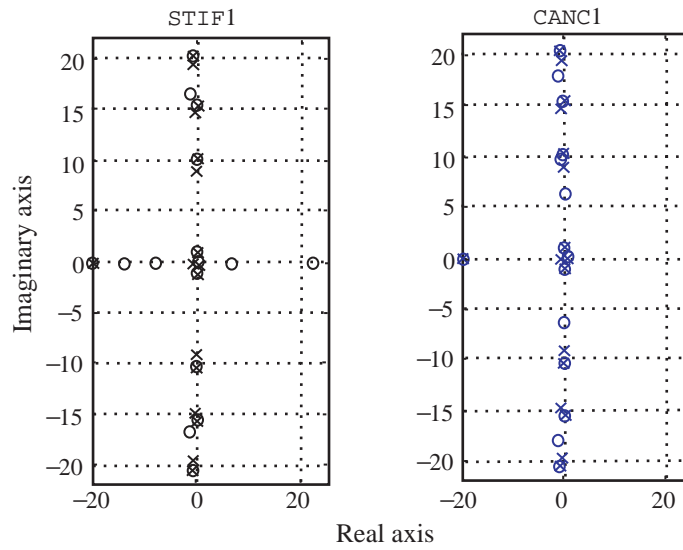


Figure 7. Migration of transfer function zeros of dynamic elastic modes with elimination of control excitation.

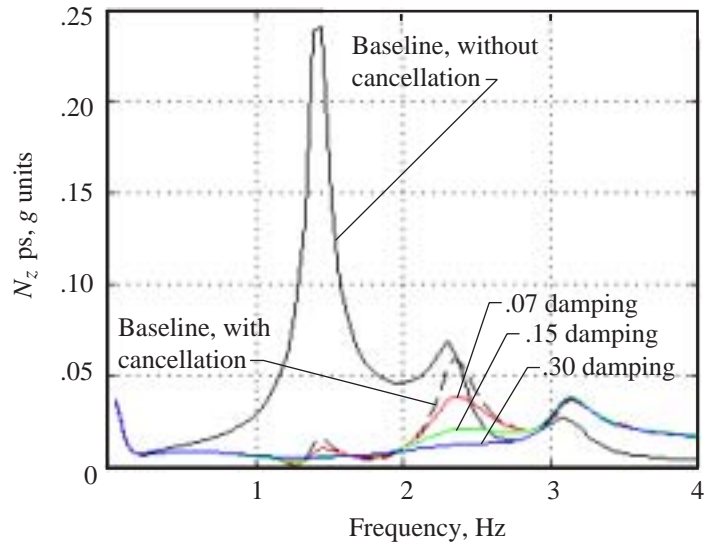


Figure 8. Effect of eliminating control excitation of first symmetric and first antisymmetric modes on frequency response to elevator inputs.

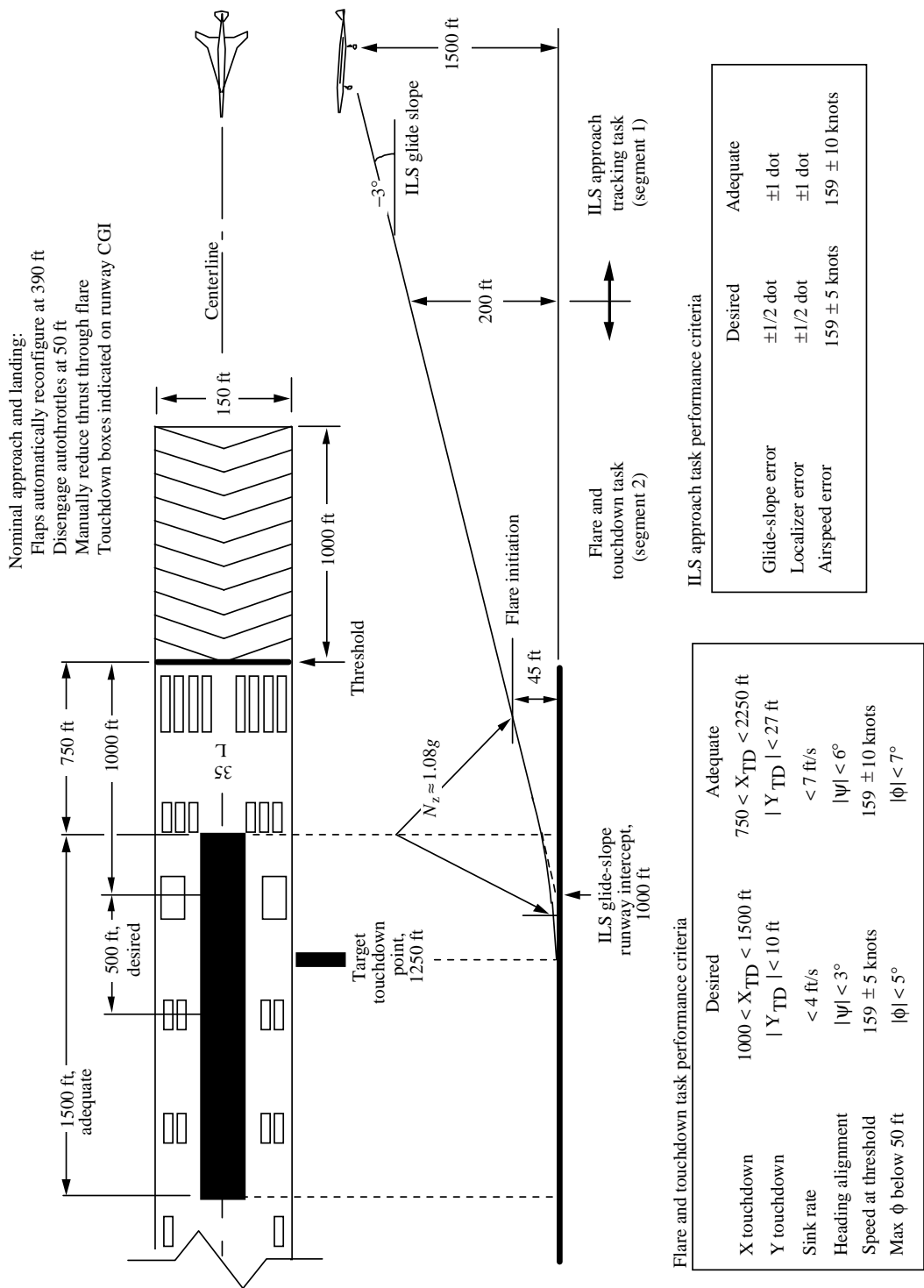


Figure 9. Task definition and performance tolerances for nominal approach and landing.

## COOPER-HARPER HANDLING QUALITIES RATING SCALE

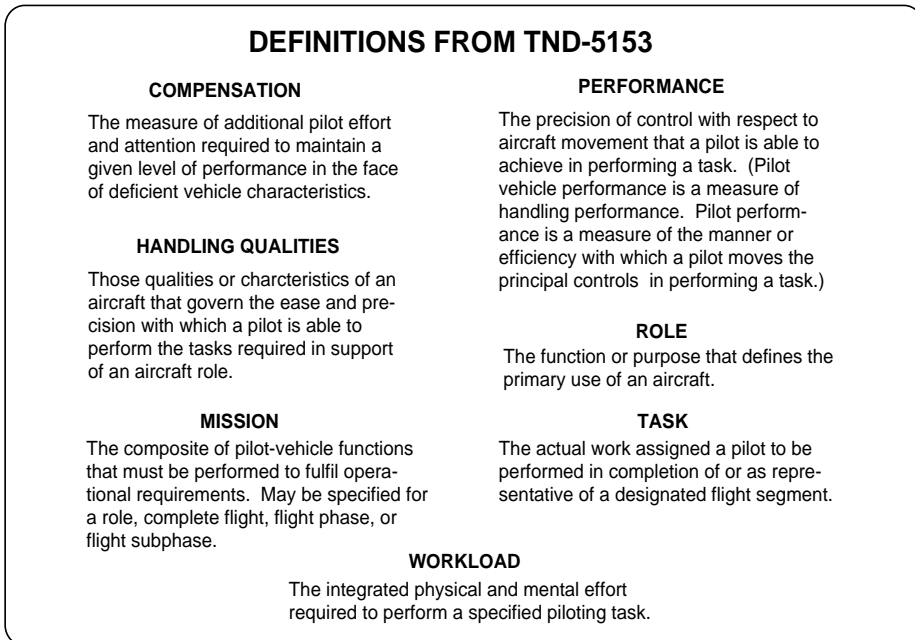
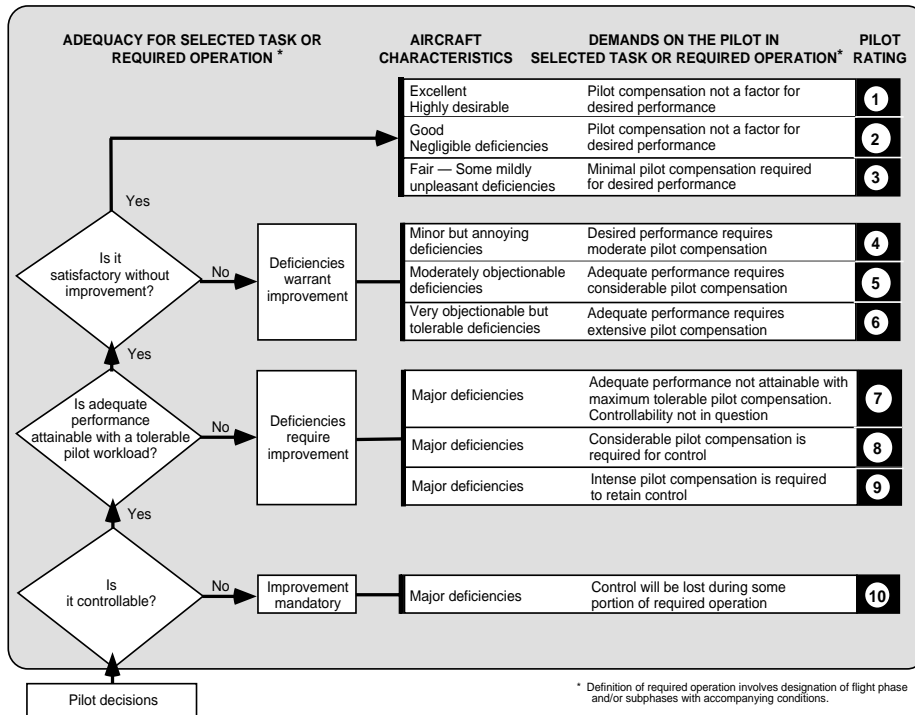


Figure 10. Cooper-Harper flying qualities rating scale and definition of associated terminology.

DASE influence on pilot's control inputs	CIR	DASE influence on ride quality	RQR
Pilot does not alter control inputs as a result of aircraft flexibility.	1	Cockpit vibrations do not impact ride quality.	1
Pilot intentionally modifies control inputs to avoid excitation of flexible modes.	2	Cockpit vibrations are perceptible but not objectionable: no improvement necessary.	2
Cockpit vibrations impact precision of voluntary control inputs.	3	Cockpit vibrations are mildly objectionable: improvement desired.	3
Cockpit vibrations cause occasional involuntary control inputs.	4	Cockpit vibrations are moderately objectionable: improvement warranted.	4
Cockpit vibrations cause frequent involuntary control inputs.	5	Cockpit vibrations are highly objectionable: improvement required.	5
Cockpit vibrations cause sustained involuntary control inputs or loss of control.	6	Cockpit vibrations cause abandonment of task: improvement required.	6

Figure 11. Supplemental pilot rating scales developed to target pilot opinion of DASE effects.



Figure 12. Composite video image recorded during all piloted evaluations.



L-1996-00132

Figure 13. External view of Langley Visual Motion Simulator.

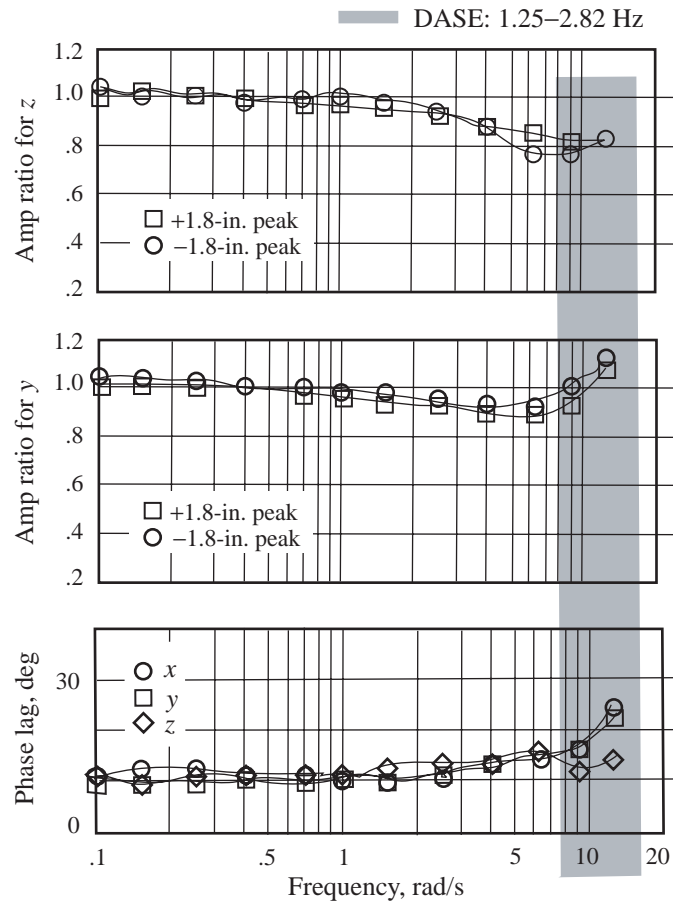


Figure 14. Frequency response of Langley Visual Motion Simulator as documented in reference 8.

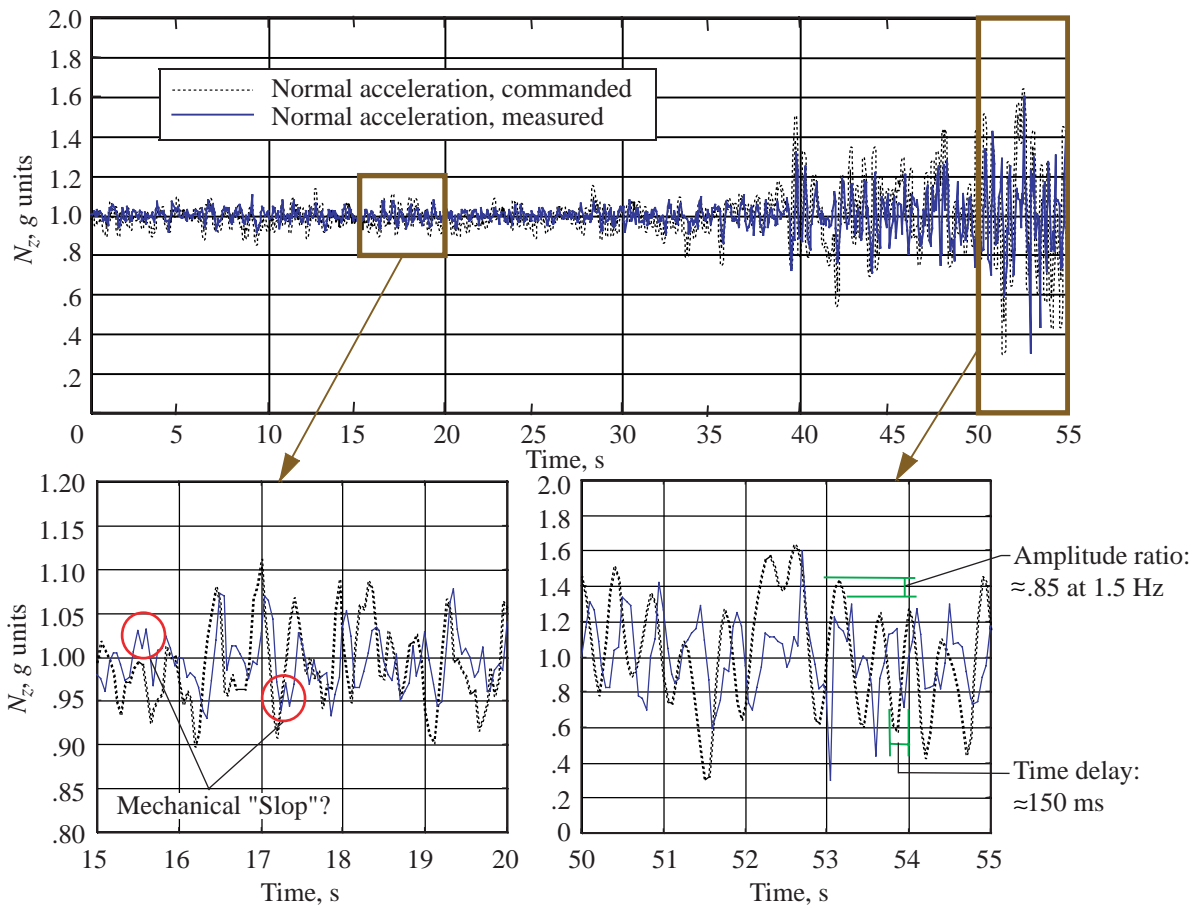


Figure 15. Time history of commanded and actual vertical accelerations recorded during aeroelastic maneuver task.

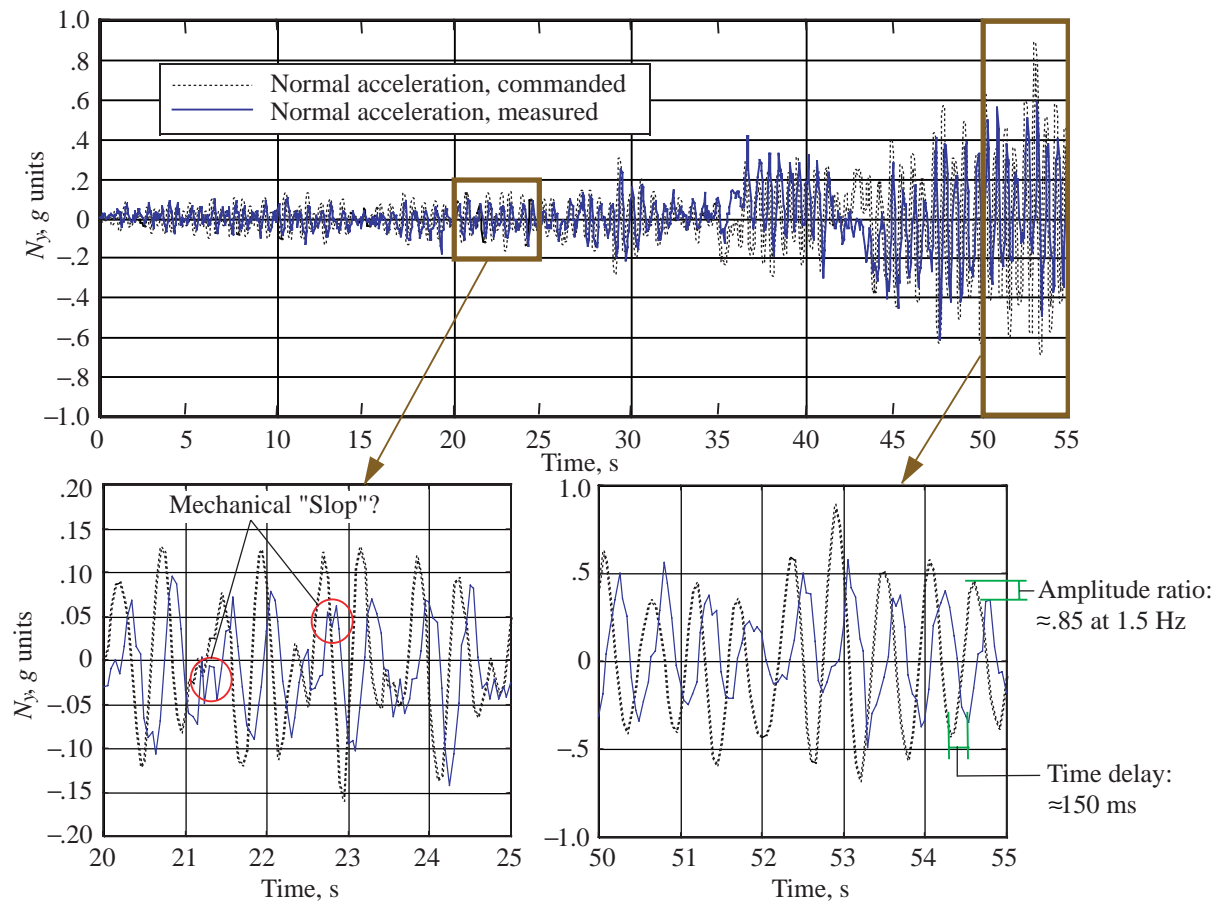


Figure 16. Time history of commanded and actual lateral accelerations recorded during aeroelastic maneuver task.

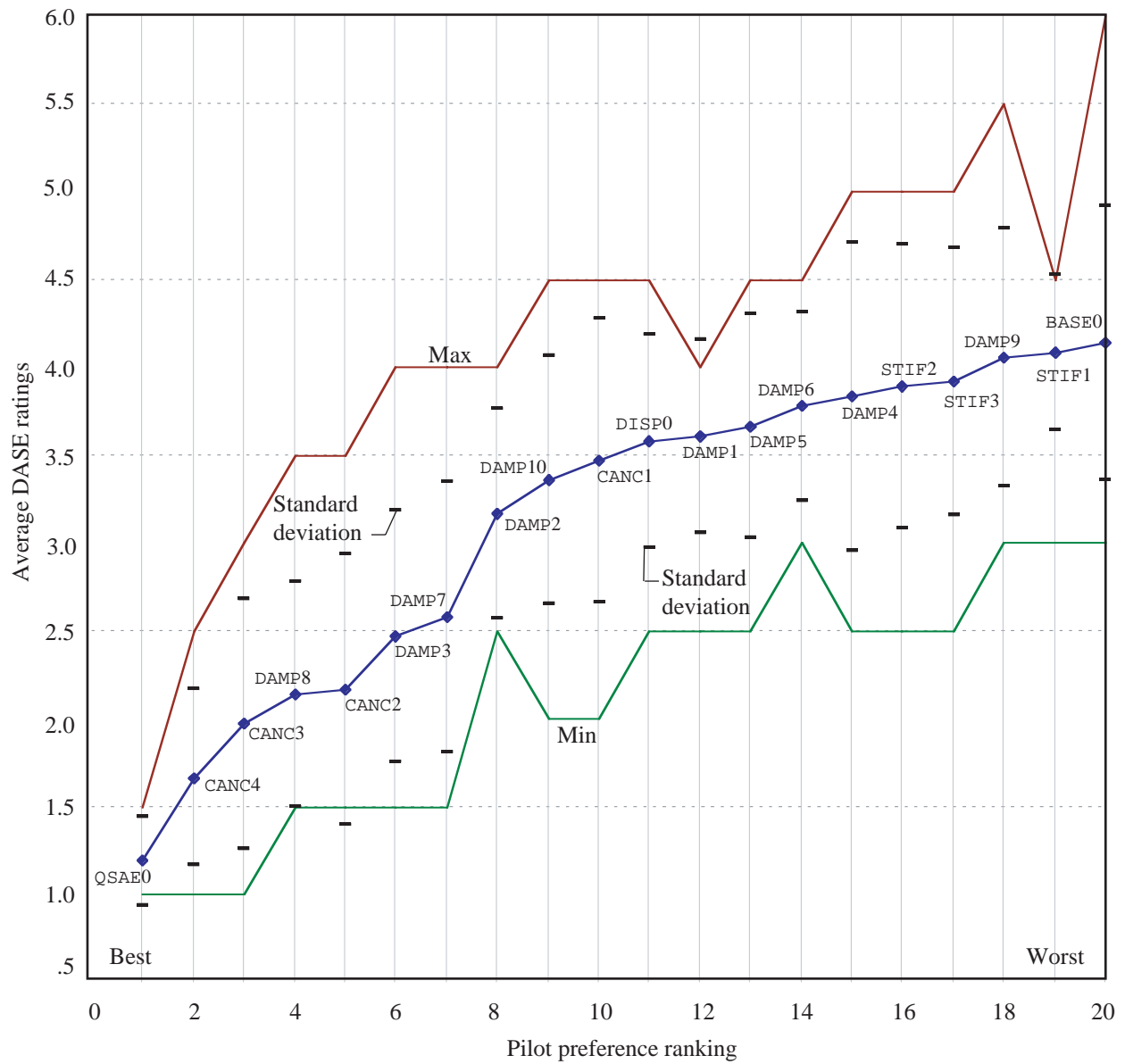


Figure 17. Pilot preference ranking of parametric aeroelastic configurations based on DASE ratings.

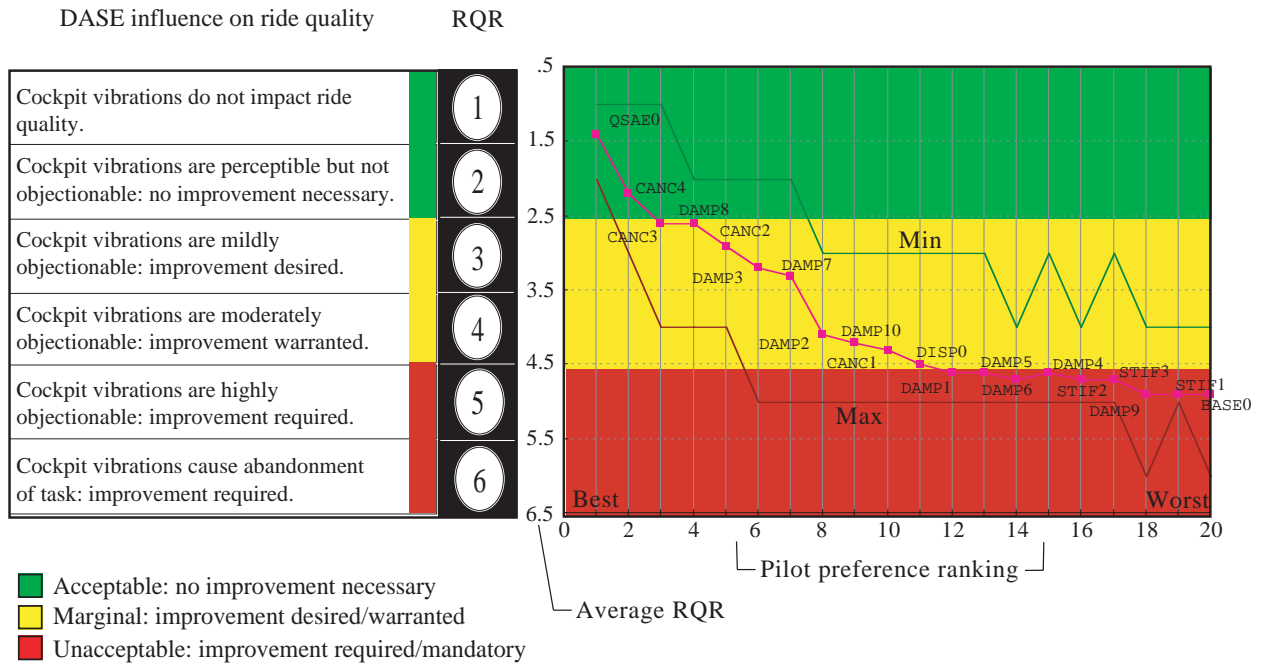


Figure 18. Average ride quality rating versus overall pilot preference ranking of parametric configurations.

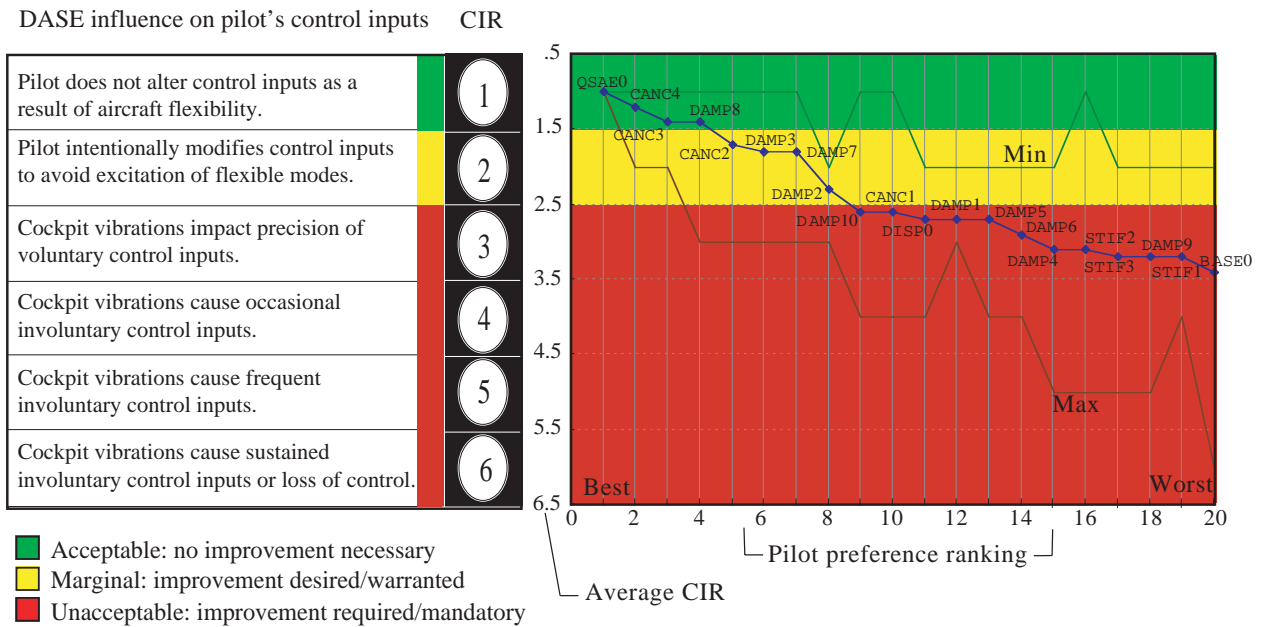


Figure 19. Average control influence rating versus overall pilot preference ranking of parametric configurations.

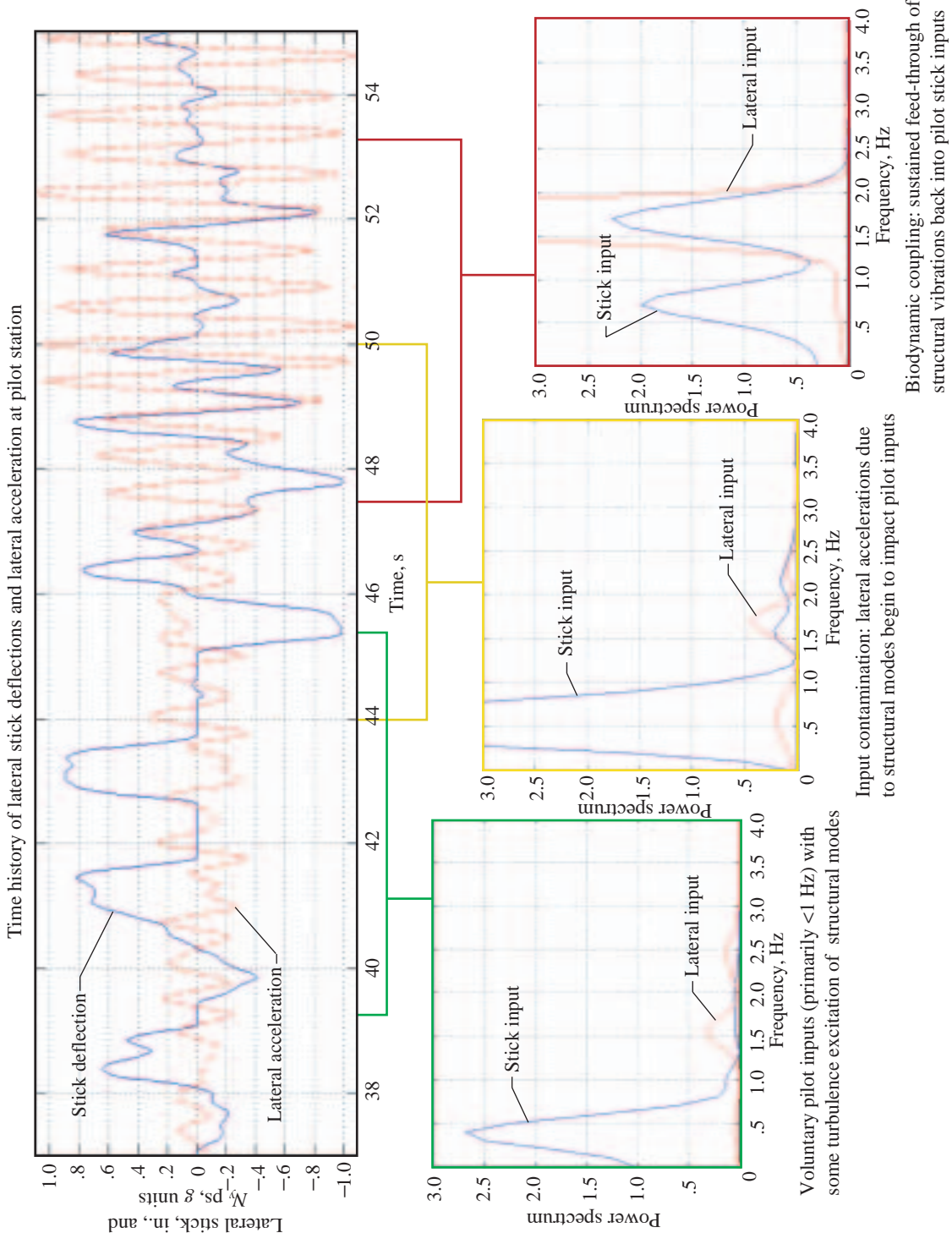
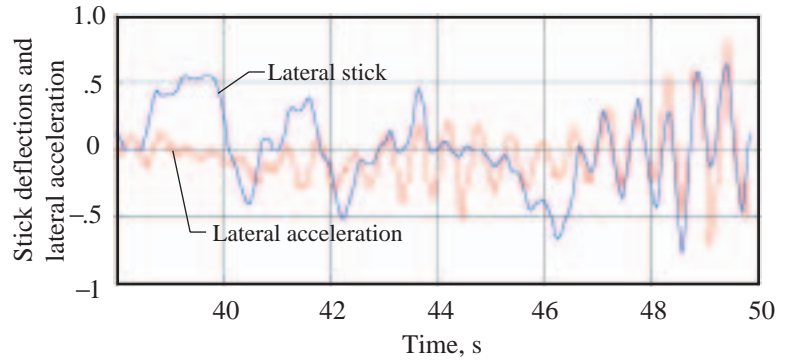
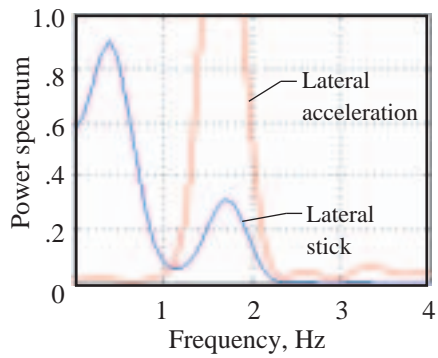
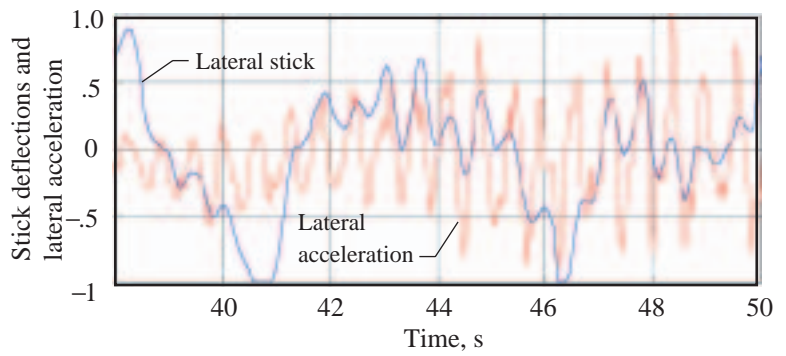
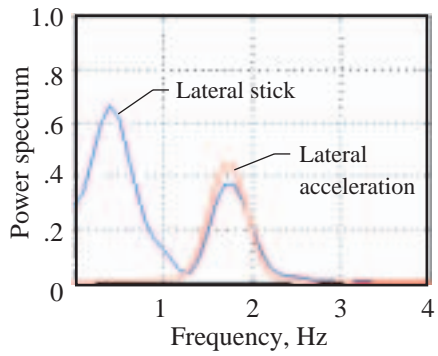


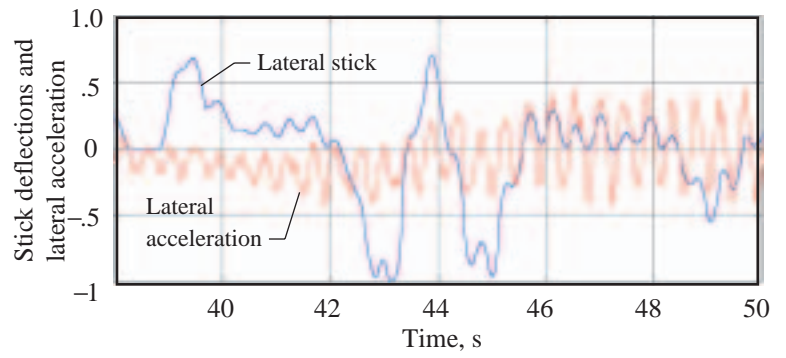
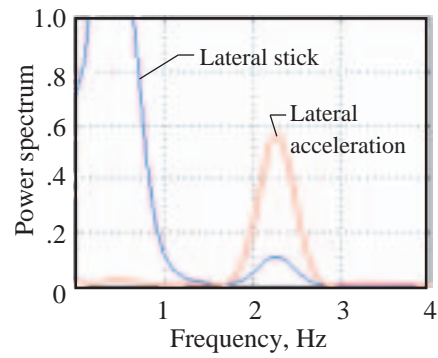
Figure 20. Power-spectral analysis of biodynamic coupling incident for pilot B.



(a) Pilot B; DAMP9 configuration; CIR: 4, RQR: 6.



(b) Pilot E; DAMP9 configuration; CIR: 4, RQR: 5.



(c) Pilot C; STIF3 configuration; CIR: 5, RQR: 5.

Figure 21. Examples of biodynamic coupling incidents for pilots B, E, and C.

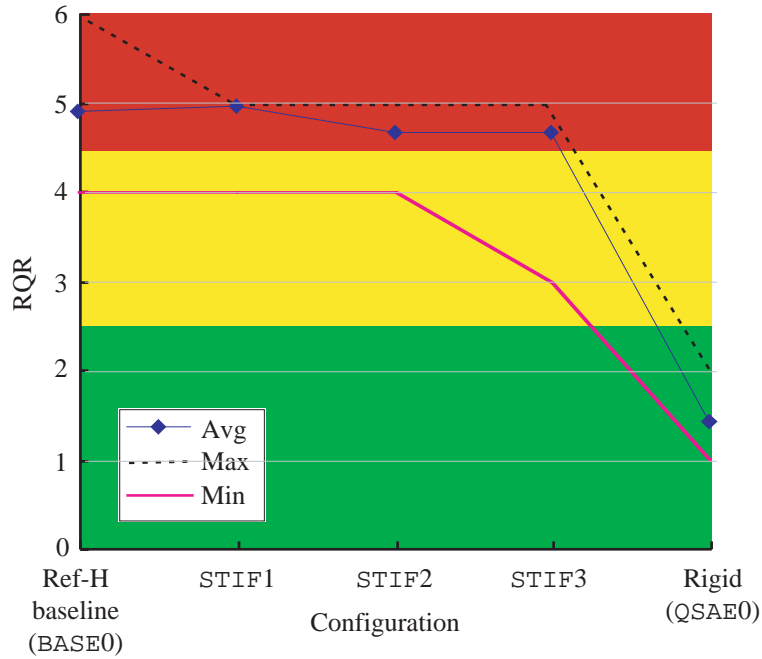


Figure 22. Variation of average RQR with increasing structural stiffness.

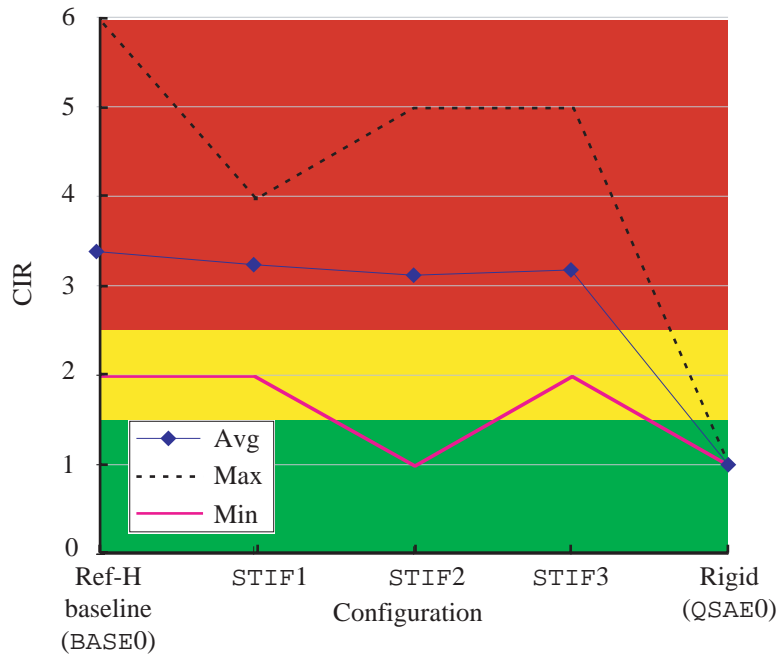


Figure 23. Variation of average CIR with increasing structural stiffness.

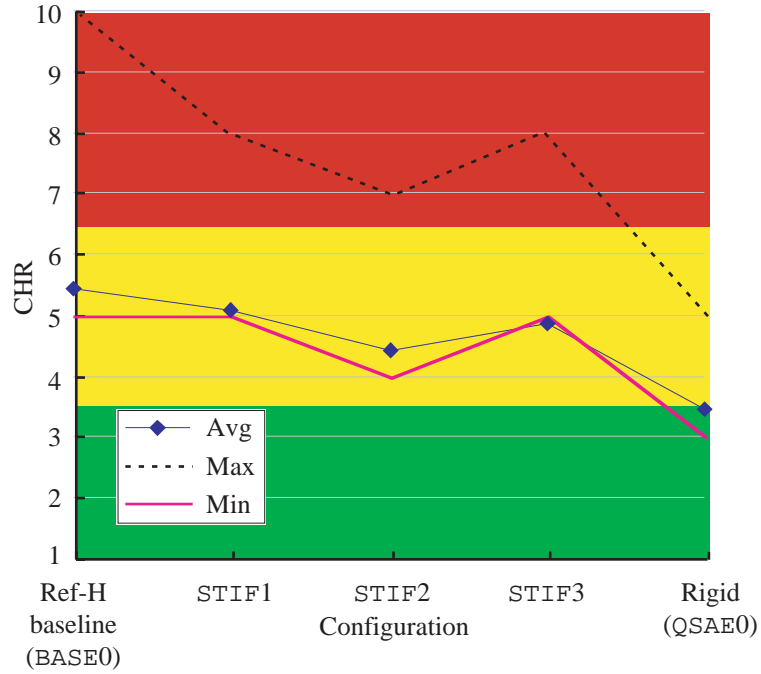


Figure 24. Variation of average CHR with increasing structural stiffness.

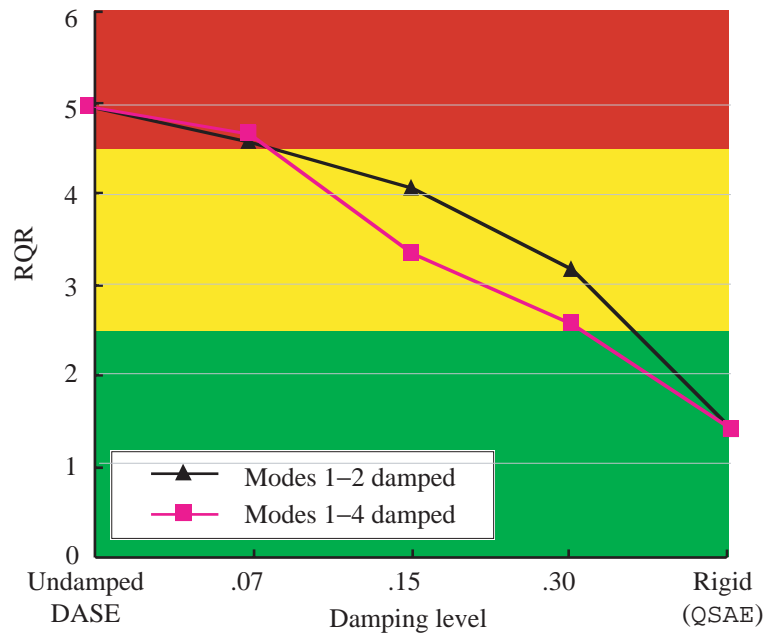


Figure 25. Variation of average RQR with increasing modal damping.

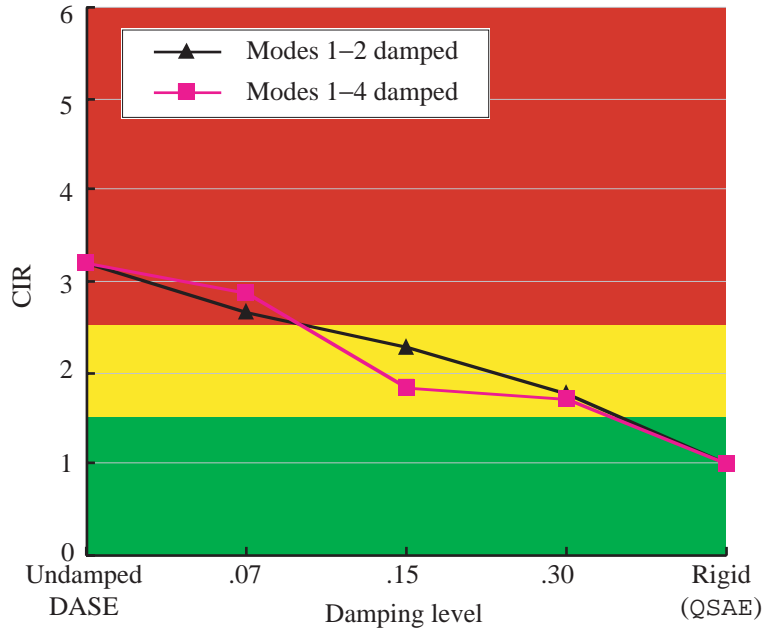


Figure 26. Variation of average CIR with increasing modal damping.

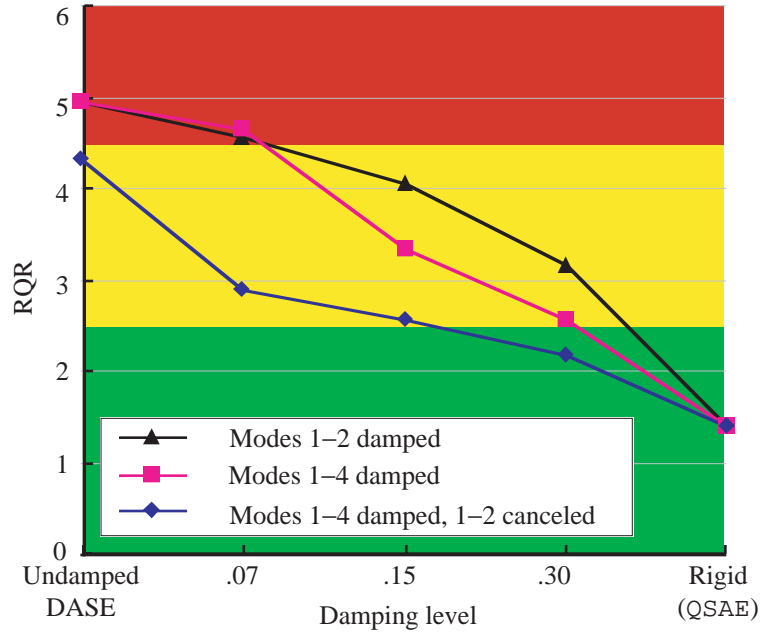


Figure 27. Impact of mode-canceling control on RQR.

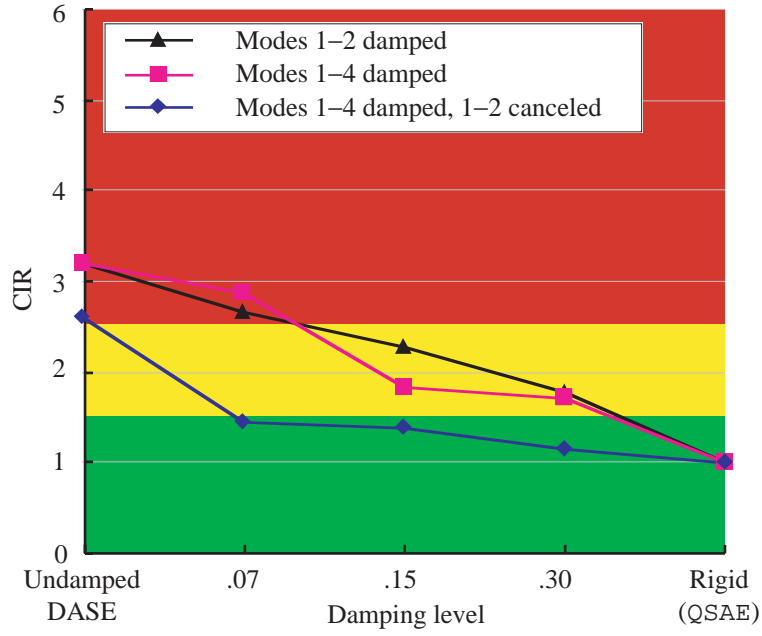


Figure 28. Impact of mode-canceling control on average CIR.

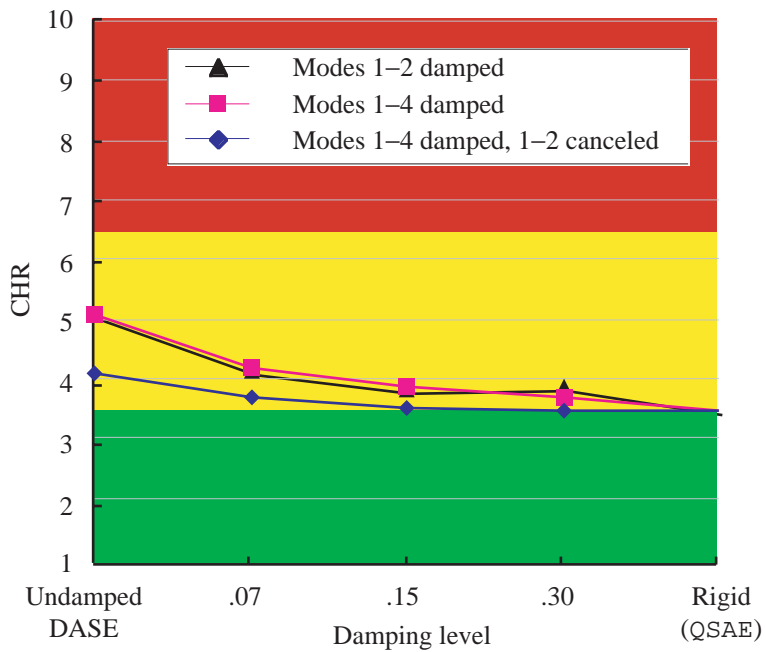


Figure 29. Variation of average CHR with increasing damping and modal cancellation.

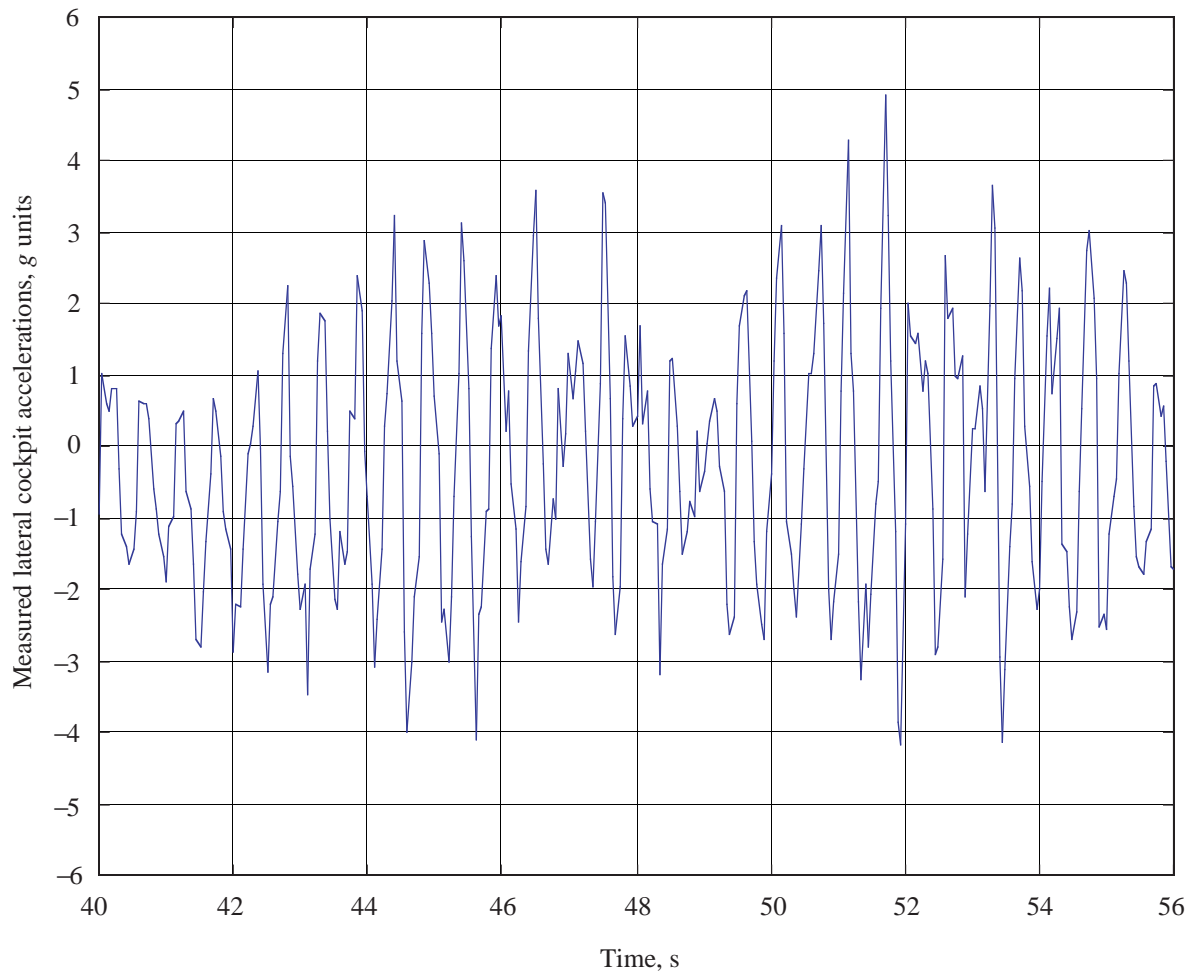


Figure 30. Measured lateral accelerations from last 15 s of one example run performed with STIF2 configuration.

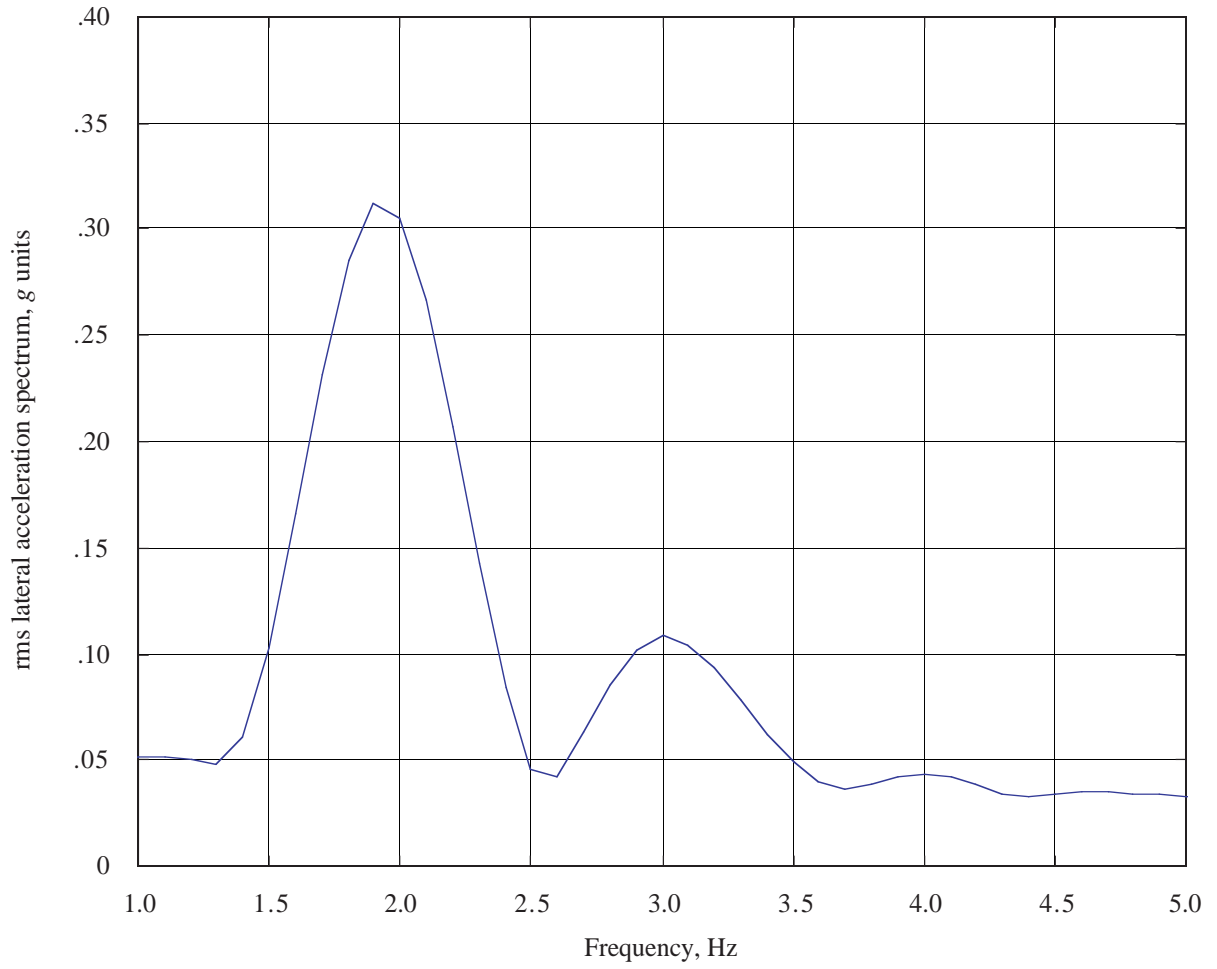


Figure 31. Lateral vibration spectrum plot for example time history.

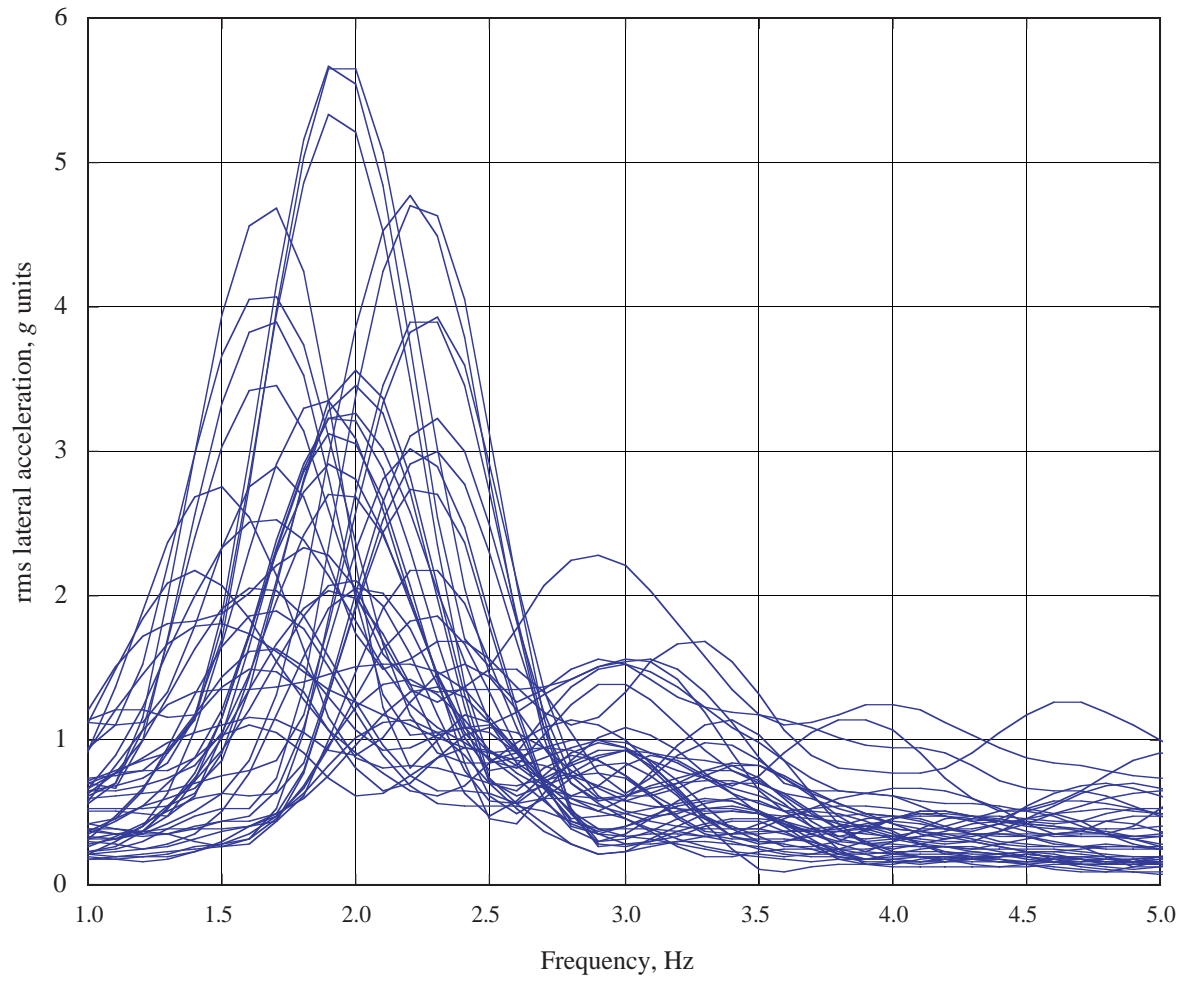


Figure 32. Lateral vibration spectra plots for all lateral-offset time histories given RQR of 5.

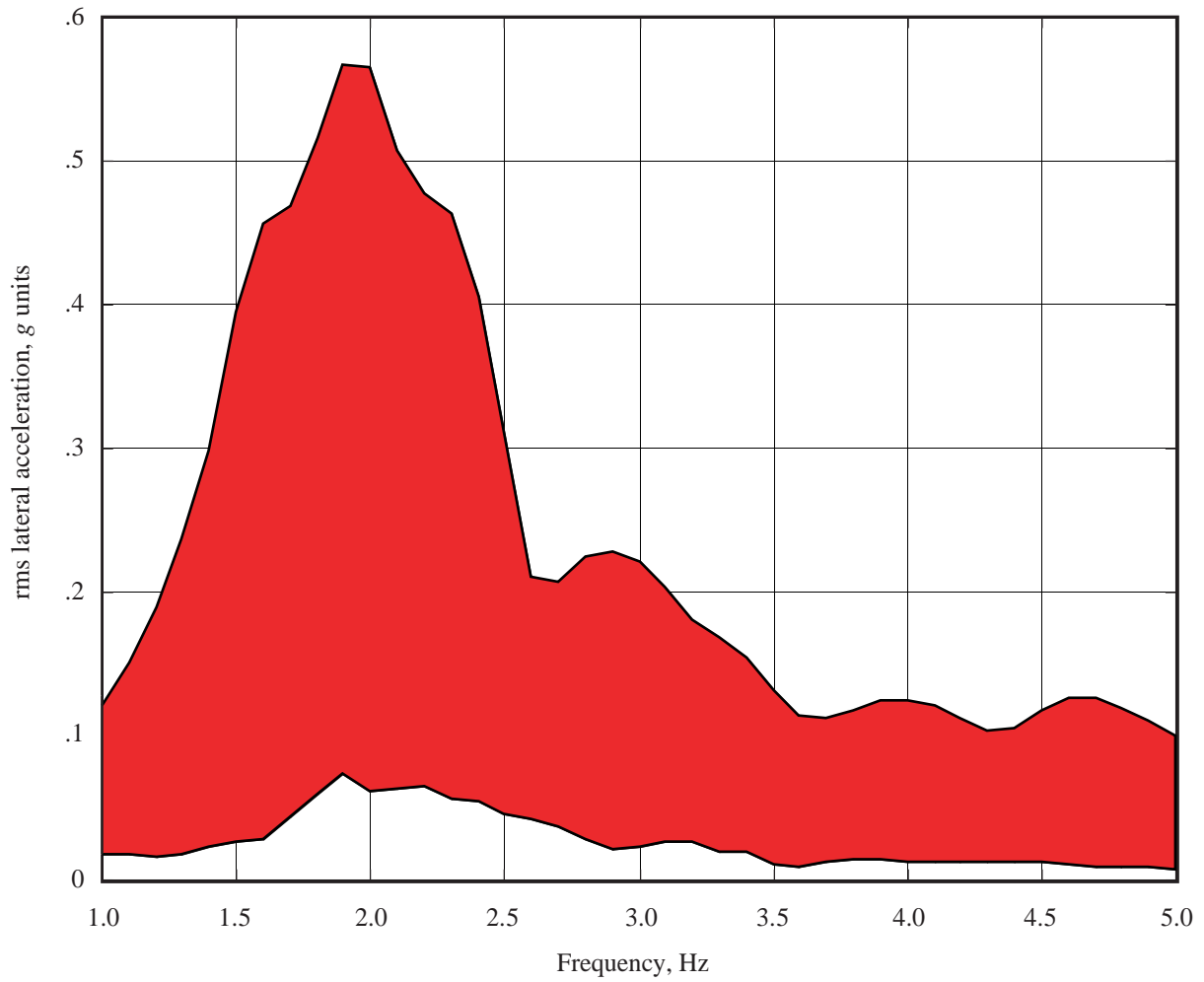


Figure 33. Lateral vibration spectral envelope based on maximum and minimum rms spectrum values for all runs given RQR of 5.

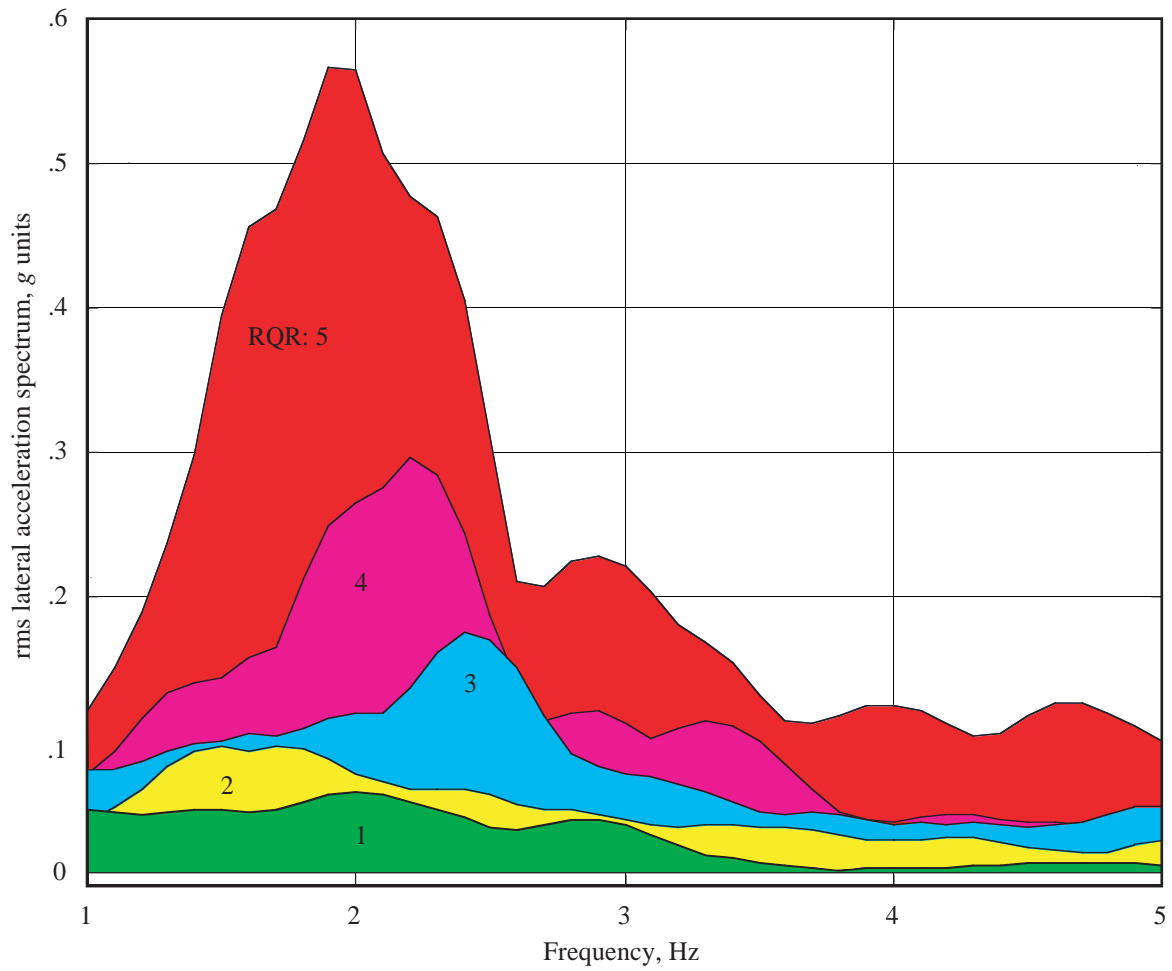


Figure 34. Lateral vibration spectral envelopes for various RQR levels.

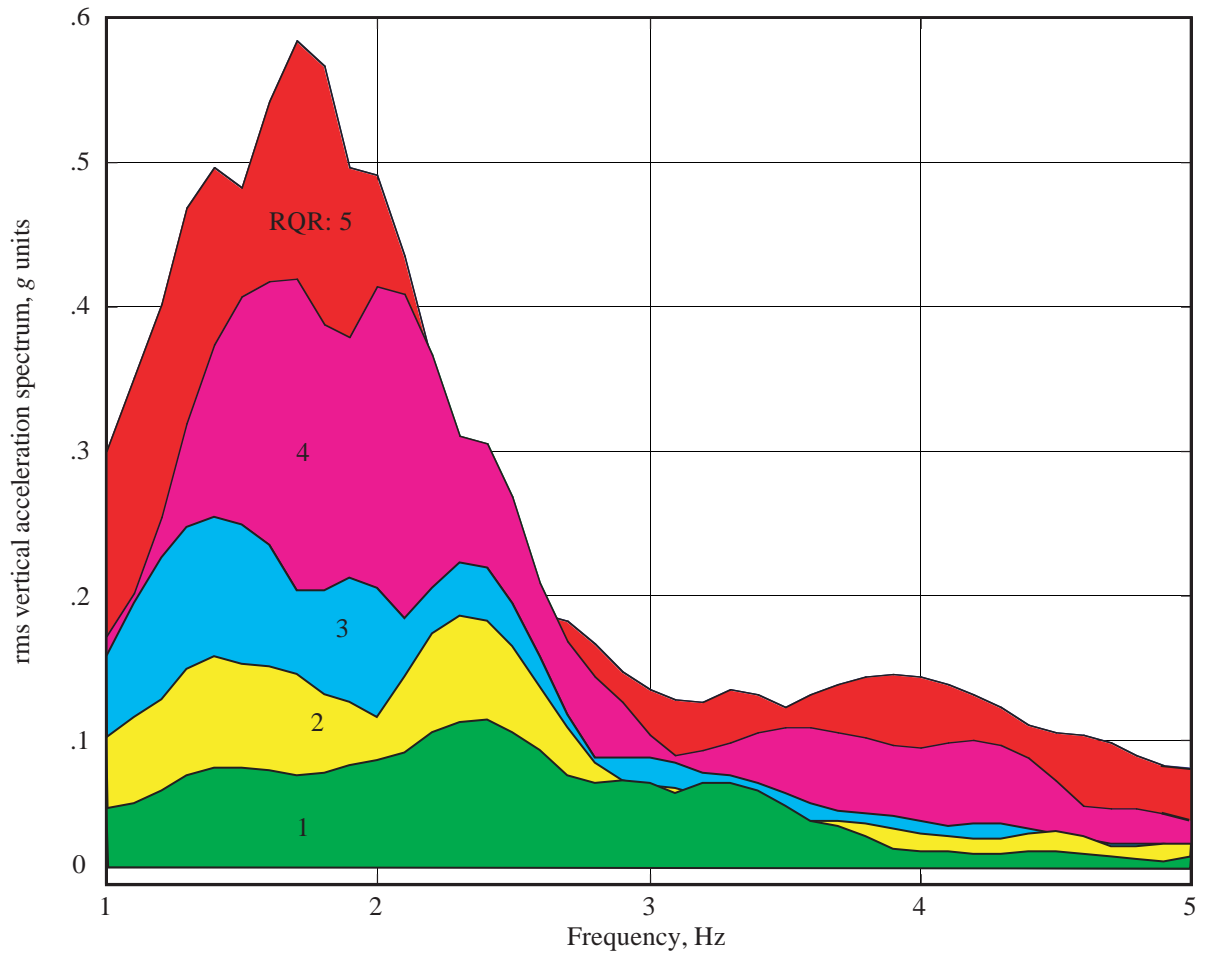


Figure 35. Vertical vibration spectral envelopes for various RQR levels.

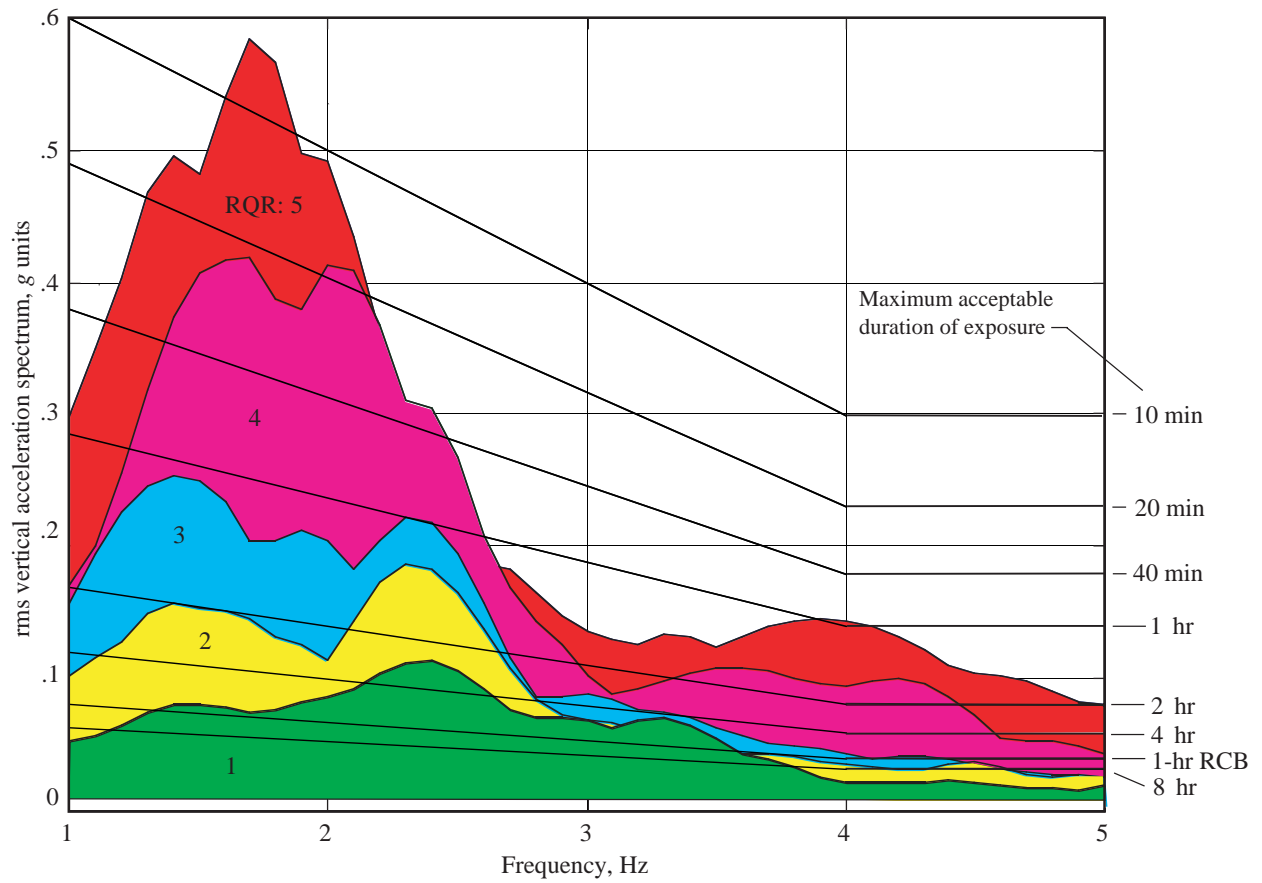


Figure 36. Vertical vibration spectral envelopes based on ride quality rating plotted with ISO vertical vibration standard.

## **Appendix A**

### **Test Pilot Biographies**

#### **Pilot A**

Pilot A was trained as a Naval Aviator and flew F-8s in both active and reserve duty. Pilot A flew with a major airline for 4 years in Boeing 727 aircraft before joining NASA as an Instructor Pilot in the Shuttle Training Aircraft; then he became a Research Pilot at a NASA Research Center. As a NASA pilot, he has flown a number of research aircraft in addition to research simulations of other vehicles. Pilot A holds a Bachelor of Science degree from the University of North Carolina at Chapel Hill and a Masters in Aerospace Engineering degree from the University of Virginia. Pilot A has accumulated over 10 000 flying hours in over 45 different aircraft including F-8, F-18, F-16, F-15, F-5, A-4, Boeing 727, Boeing 737, Gulfstream II/STA, T-38, OV-10, LR-28 aircraft, and a number of general aviation types.

#### **Pilot B**

Pilot B has a Bachelor of Science degree from the University of Washington where he attended a flight test course. Pilot B served as Engineering Test Pilot for two general aviation manufacturers and accumulated time as a test pilot on 30 different general aviation fixed wing aircraft, before joining an HSR program industry partner as a research project pilot. He is a graduate of a company-run flight test school. Pilot B holds an Airline Transport Pilot Certificate with type ratings in seven transport aircraft, and has over 16 000 hours flight time, of which nearly 10 000 hours have been in flight tests. Pilot B is a certificated flight instructor in both general aviation and transport aircraft with 3000 hours of instruction given.

#### **Pilot C**

Pilot C was trained as a Naval Aviator and graduated from the U.S. Naval Test Pilot School, Patuxent River, Maryland. Pilot C has a Ph.D. in Hypersonic Flight Dynamics from the University of Southern California. He is employed by an HSR program industry partner as the chief pilot for the High Speed Civil Transport and as a project experimental test pilot in a number of aircraft programs. He holds an Airline Transport Pilot Certificate, and has first pilot time in over 50 aircraft, including the F-14A and several transport aircraft.

#### **Pilot D**

Information not available.

#### **Pilot E**

Information not available.

#### **Pilot F**

Pilot F served with the U.S. Marine Corps from 1953 to 1962 as a single-engine fighter-bomber pilot. He has been a research pilot with NASA since 1962 and has accumulated more than 10 000 total hours in a wide variety of aircraft, including helicopter, VTOL, STOL, and light and heavy fixed wing aircraft. He has an Airline Transport Pilot Certificate with type ratings in the Convair 990 and the Douglas DC-8.

## Appendix B

### Flight Cards

This appendix presents the flight cards used in the LaRC.3 experiment.

#### Nomenclature

AGL	above ground level, ft
ALT	altitude
AOA	angle of attack, deg
A/T	autothrottle
CDU	cockpit display unit
C.G.	center of gravity, percentage of mean aerodynamic chord
CHR	Cooper-Harper pilot rating
Config	aircraft configuration
DME	distance measuring equipment (distance from runway threshold)
Dir	directional
EPR	exhaust pressure ratio (shorthand for throttle position)
F/D	flight director
FPM	feet per minute
ft/sec	feet per second
GEAR	landing gear position
G/S	glide slope (part of instrument landing system)
GW	gross weight
HUD	head-up display
ILS	instrument landing system
KEAS/m	equivalent airspeed, knots
Lat	lateral

LEF	leading-edge flaps, deg
LOC	localizer (part of instrument landing system)
M	Mach number
MFC	final cruise mass condition
MIC	initial cruise mass condition
MTE	mission task element
Mmo	maximum operating Mach number
M13	mass case 13: maximum taxi weight at forward C.G.
N/A	not applicable
OM	outer marker
PF	pilot flying
PFD	primary flight display
PIO	pilot-induced oscillation
PNF	pilot not flying
PSCAS	pitch stability and control augmentation system
R	constant value during run either +1 or -1
R/C	rate of climb
RQR	ride quality rating
RSCAS	roll stability and control augmentation system
Rwy	runway
TEF	trailing-edge flaps, deg
TIFS	total in-flight simulator
Trim	indicates this parameter should be set to value required to achieve trimmed (unaccelerated) initial conditions
VFR	visual flight rules

$V_{app}$	approach speed
$V_{app1}$	approach speed, first approach segment
$V_{app2}$	approach speed, second approach segment
$V_{g/a}$	go-around speed
$V_{min}$	minimum operating speed
$V_{ref}$	reference speed
X	cross











1. *Bank angle scale with roll pointer and sideslip indicator.* This section of the LaRC.1 HUD is specified to be the same as previously employed for the 1995 LaRC.0 assessment study. It should be noted that after initial evaluations during LaRC.0, the sideslip indicator (lower portion of roll pointer triangle) displays complementary filtered sideslip angle as the default for all tasks. The sideslip indicator will turn amber when it moves just past the edge of the roll pointer indicating a sideslip angle of  $4^\circ$ .

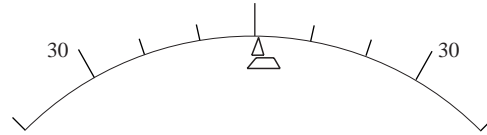


Figure C2. Bank angle scale with roll pointer and sideslip indicator.

2. *Heading scale-horizon line.* This section of the LaRC.1 HUD is specified to be the same as previously employed for LaRC.0. Smaller tick marks, without labels, are drawn at  $5^\circ$  increments.



Figure C3. Heading scale-horizon line.

3. *Airspeed tape display.* Item 3 is a totally new element for the NASA LaRC Ref-H assessment project. It displays analog and digitally filtered equivalent airspeed (EAS) that were displayed only digitally on the 1995 LaRC.0 HUD. Several airspeed bugs are required for this system. Takeoff decision speed  $V_1$ , rotation speed  $V_r$ , takeoff safety speed  $V_2$ , and maximum operating speeds  $V_{mo}$  and  $M_{mo}$  are displayed.  $V_{mo}$ ,  $M_{mo}$ , and  $V_{min}$  boundaries are indicated by red and white checkered areas on the right side of the airspeed tape reference line. Values of  $V_1$ ,  $V_r$ ,  $V_2$ ,  $V_{mo}$ ,  $M_{mo}$ , and  $V_{min}$  are read from the maneuver IC files. Speeds  $V$  are displayed on the right side of airspeed tape reference line (white). Current commanded airspeed, either from the IC file or from the CDU, are displayed by the appropriate icon shown in figure C4 on the left of the airspeed tape line (white). Digital equivalent airspeed is displayed in the highlighted area to the nearest knot (white). The airspeed trend line (green) indicates the anticipated airspeed that will exist in 10 s. It emanates from the origin of the airspeed tape. The inertial acceleration parameter from the airspeed complementary filter system is used for this purpose. A 1-s time lag is applied to this variable to smooth its response. The open areas of the airspeed indicator are not shaded.

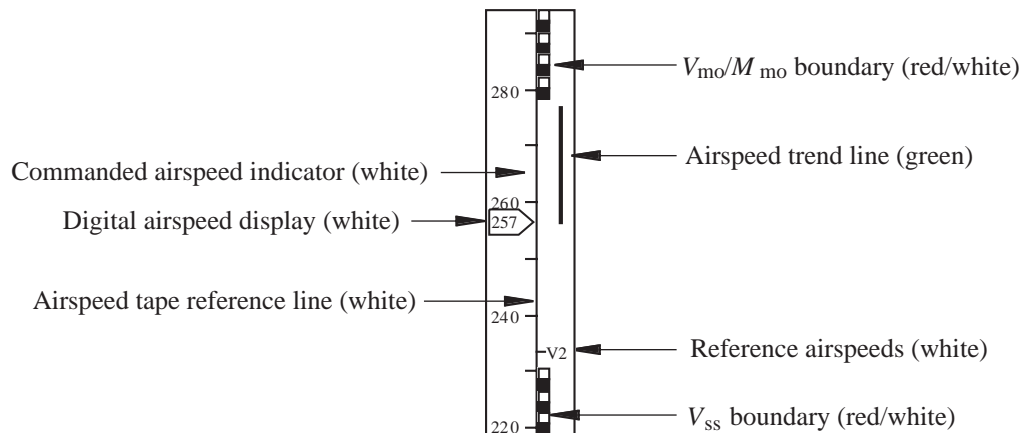


Figure C4. Airspeed tape display.

4. *Altitude display tape.* The altitude tape display is also a new HUD element. It provides detailed altitude information to the pilot. The digital altitude display (white) is different from the airspeed digital display in that the digits representing hundreds of feet scroll at a different rate than the digits representing tens of feet. For example, for altitudes between 6400 and 6500, the 064 would remain constant and the digits representing tens of feet would change. Note that the digits representing tens of feet are resolved in 20-ft increments. The color of the altitude tape reference line, tick marks, and labels is white unless the altitude is below the minimum altitude. When the altitude is below the minimum, the altitude tick marks are amber. Minimum altitude is set at 200-ft AGL. The rate of climb display (white) indicates the analog rate of climb only when the rate of climb is between +4000 and -4000 fpm. When the rate of climb is greater than  $\pm 4000$  fpm, the rate of climb will be displayed by three digits (white) at the top (or bottom) of the scale indicating rate of climb in hundreds of feet per minute (fpm). The scaling of this display is nonlinear in that the distance from 0 to 1000 fpm is twice that between 1000 and 2000 fpm, which is twice the distance between 2000 and 3000 fpm. The distance between 3000 and 4000 fpm is the same as 2000 to 3000 fpm. The minimum altitude wedge (amber) will become visible when the altitude reaches the minimum altitude (200 ft) with the base of the wedge touching the altitude scale line when the altitude reaches 0 ft. An option is given to switch between pressure altitude and radar (landing gear) altitude. When in radar altitude mode, an R (white) is displayed at the top and bottom of the altitude scale line. No indication is shown when not in radar altitude mode (i.e., a P is not displayed when not in radar mode in an attempt to reduce HUD clutter). The open areas of the altitude indicator are not shaded.

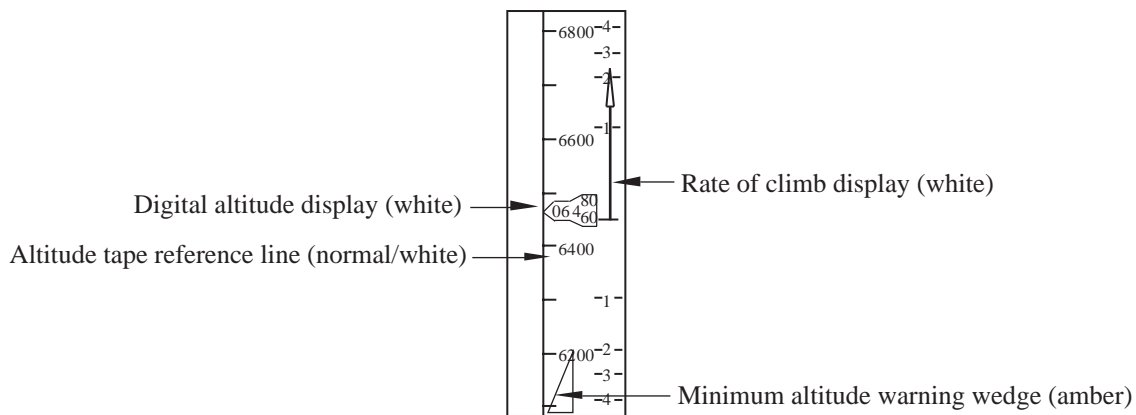


Figure C5. Altitude display tape.

5. *Velocity vector cluster.* The velocity vector cluster (white) is similar to that used in the 1995 LaRC.0 HUD and includes the velocity vector symbol (an open circle with fins), option digital airspeed, altitude and distance measuring equipment (DME) readouts, an airspeed error tape that grows above or below the left fin of the velocity vector symbol, and an acceleration indicator. The main difference is that the digital airspeed and altitude indicators of the 1995 LARC.0 HUD could be moved to the airspeed and altitude display tapes. DME distance to the runway threshold can also be displayed if desired. Other minor changes are that the acceleration diamond is now a caret (>) and that it is driven differently. The acceleration caret indications are now dependent on inertial acceleration computed in the airspeed complementary filter section. This computation employs the acceleration of the C.G. of the aircraft resolved along the flight path. A 1-s lag is applied to this signal to improve its motion. In addition, the capability to automatically move the acceleration indicator from the velocity vector cluster to the pitch reference waterline has been implemented. It will move to the reference waterline when the angle of attack is above  $15^\circ$  and back to the velocity

vector cluster when the angle of attack is below 14°. Another feature of the acceleration arrow is that its zero position can be biased to permit its use while maintaining a nonzero acceleration, such as that desired for the entry phase of the recovery from limit flight tasks.

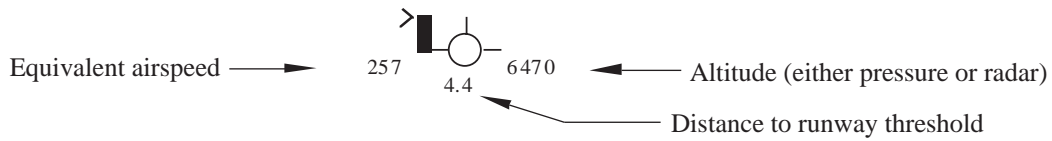


Figure C6. Velocity vector cluster.

6. *Pitch grid, reference waterline, and heading scale.* The pitch grid and reference waterline (white) were changed for the 1996 LARC.0 HUD. The waterline was replaced with a winged-V. Use of the 1995 LARC.0 HUD takeoff rotation brackets (magenta) and expanded reference waterline (item 14) are included in the HUD option. The pitch grid is much wider than the 1995 LARC.0 HUD and has the center open. Only one set of pitch grid labels is indicated for this HUD option and the labels are placed inside the left-side pitch grid tick marks. The horizon line and heading scale are the same as the 1995 LARC.0 HUD. The tail-scrape bar (red and white striped barber pole), which is item 13, is also retained with this HUD option.

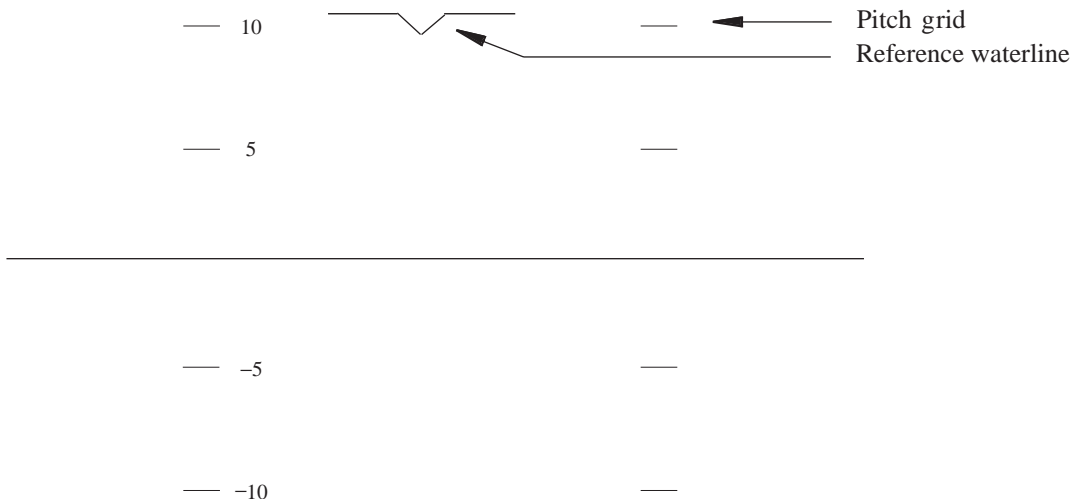


Figure C7. Pitch grid, reference waterline, and heading scale.

7. and 8. *ILS glide-slope and localizer displays.* The ILS glide-slope and localizer displays are colored white with a white moving diamond. When excessive deviation occurs, the white diamond changes to an amber flashing diamond. Excessive deviation is one dot. The glide-slope display is placed just outside the altitude display tape.

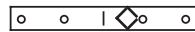


Figure C8. ILS glide-slope and localizer displays.

9. *Analog-digital angle of attack display.* Digital angle of attack moves with the analog pointer on the scale. If the angle of attack is not displayed with this display, digital angle of attack is displayed in the upper left-hand corner of the HUD.

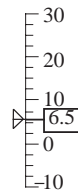


Figure C9. Analog-digital angle of attack display.

10. *Analog-digital acceleration tape (white) display.* Digital normal acceleration moves with the analog pointer on the scale. If the normal acceleration is not displayed with this display, digital normal acceleration is displayed in the upper left-hand corner of the HUD.

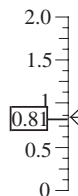


Figure C10. Analog-digital acceleration tape display.

11. *Takeoff climb guidance system.* This system consists of a labeled dashed line with a velocity vector guidance symbol (an open circle). The dashed line (magenta) is displayed when the pilot is commanded to fly a specific climb gradient. The labels of this line represent the climb gradient, in percent. When the velocity vector guidance system is operating in this mode, the velocity vector guidance symbol (also magenta) is constrained to travel across the dashed line and provides the pilot with steering information only to maintain the extended runway centerline. When the takeoff guidance system is in airspeed command mode, the dashed line is removed and the velocity vector guidance symbol provides both longitudinal and lateral information. Longitudinal guidance is a combination of airspeed error and inertial acceleration and is provided to assist the pilot to maintain the desired airspeed when operating in a fixed-thrust mode. The pilot attempts to place the velocity vector symbol on top of the velocity vector guidance symbol. The lateral guidance is the same regardless which mode of the takeoff climb guidance system is selected.



Figure C11. Takeoff climb guidance system.

12. *Depressed glide-slope reference line.* The purpose of this reference line is to provide the pilot with an indication of where to place the velocity vector to fly a flight-path angle equal to the glide slope. It is horizontally slaved to the velocity vector.



Figure C12. Depressed glide-slope reference line.

13. *Tail-scrape bar* (red and white striped barber pole). The tail-scrape bar indicates what pitch attitude the aircraft would have to reach in order to scrape the tail on the ground.



Figure C13. Tail-scrape bar.

14. *Reference waterline (white).* Most of the time the reference waterline is the smaller size, which is indicated by the label normal reference waterline. During takeoff rotations, however, the reference waterline becomes much larger and is used in conjunction with the pitch rate error brackets to precisely control the rotation performance of the aircraft. The pitch rate error brackets are approximately 2° high. A pitch rate error of ±0.5 deg/s will displace the pitch rate error bracket one half the height of the inner pointer with respect to the reference waterline. A pitch rate error of ±1.0 deg/s will displace the pitch rate error bracket one half its total height with respect to the reference waterline.

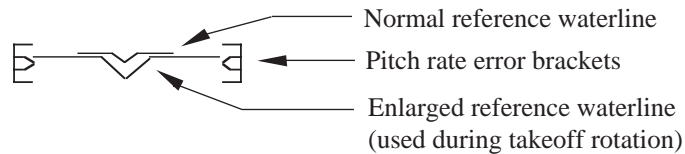


Figure C14. Reference waterline.

15. *Digital information selective display in upper left-hand corner of HUD.* When angle of attack and normal acceleration are being displayed with the analog/digital tape displays, those parameters are removed from this element.

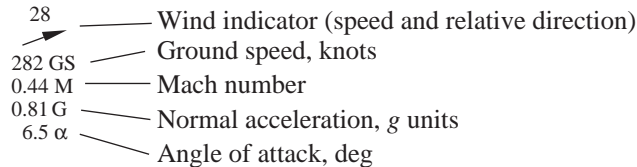


Figure C15. Digital information selective display.

## Appendix D

### Flight Director Implementation for Task 3115

The composite flight director tracking task allowed the pilot to evaluate the ability to accurately maneuver the aircraft by following flight director commands. The flight director was driven with a composite signal containing elements from various maneuver segments that had been examined in previous Ref-H simulations. These maneuver segments included a localizer capture from the nominal approach, glide-slope capture, a descending turn, and a rapid pull-up as found in the landing go-around tasks. Each of these segments are described in this appendix. Flight-path and track angle commands from these segments were combined with varying order and sign to produce a flight director behavior that was not easily anticipated, but which was still representative of actual flight maneuver tasks.

#### Maneuver Segments for Use With Composite Flight Director Tracking Task

##### *Go-Around Plus Spiral Descent*

A sequence of flight-path and heading changes to the flight director was used to create an aggressive pull-up followed by a descending turn. This sequence is shown in table D1 and figure D1.

Table D1. Flight-Path Angle and Heading Angle Command Sequences for Go-Around Plus Spiral Descent Task

Time, s	Flight-path angle command, deg	Heading angle command, deg ( $\times R1$ )
0	0	0
10	15	0
13	15	0
23	5	-15
25	5	-15

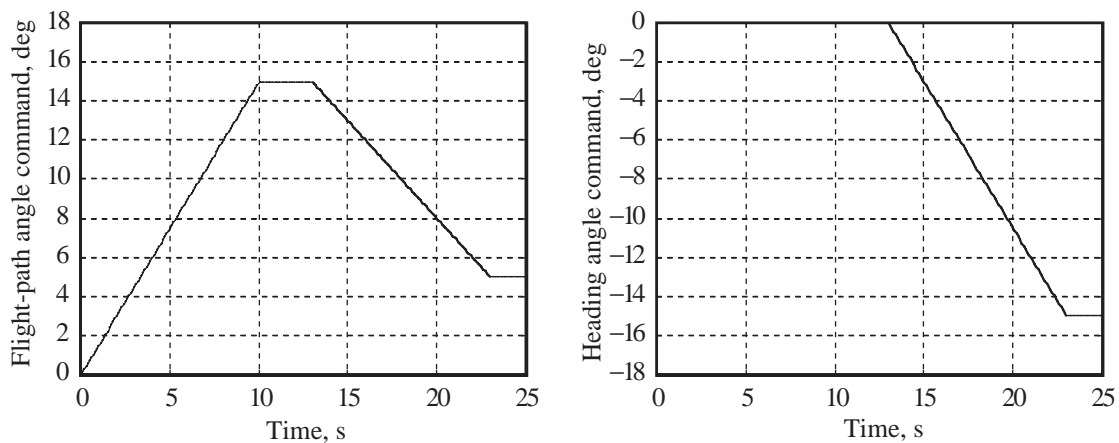


Figure D1. Flight-path angle and heading angle time histories.

***Glide-Slope Intercept***

Another portion of the flight director tracking task included a flight-path change corresponding to a glide-slope intercept, as shown in table D2 and figure D2.

Table D2. Flight-Path Angle and Heading Angle Command Sequences for Glide-Slope Intercept Task

Time, s	Flight-path angle command, deg	Heading angle command, deg
0	0	0
5	-3	0
8	-3	0

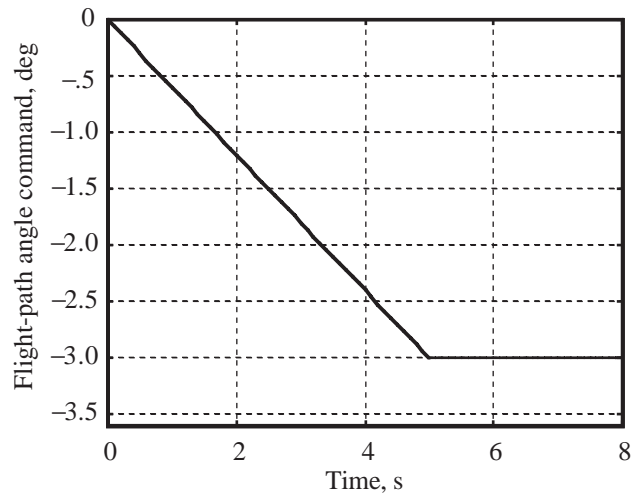


Figure D2. Flight-path angle time history for glide-slope intercept task.

***Localizer Intercept***

The heading angle command change corresponding to a localizer intercept, shown in table D3 and figure D3, constituted the third portion of the flight director tracking task.

Table D3. Flight-Path Angle and Heading Angle Command Sequences for Localizer Intercept Task

Time, s	Flight-path angle command, deg	Heading angle command, deg ( $\times R2$ )
0	0	0
10	0	15
12	0	15

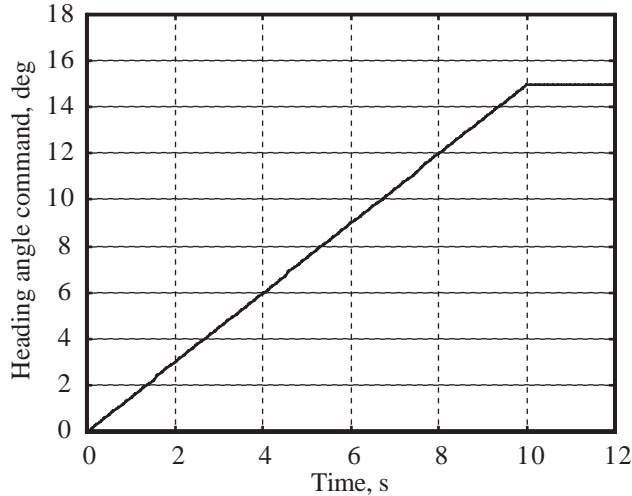


Figure D3. Heading angle command time history for localizer intercept task.

### Random Sense and Sequencing for Maneuver Segments

The sequence of execution of maneuver segments 1, 2, and 3 was randomly chosen prior to the start of a run. If a particular segment ended with a nonzero flight-path or track angle command, then the following segment was executed relative to that nonzero condition. The sequence would always begin with a 3-s interval of straight and level flight before the first of the maneuver segment flight director commands. After this 3-s interval, the flight path and heading command sequence began. The parameters  $R1$  and  $R2$  were integers which had a constant value during a run, but which were randomly chosen to be either  $-1$  or  $+1$  prior to the start of a run. Their values were independent of each another.

### Filtering of Flight Director Signals

Second-order filters were applied to signals that drove the flight director symbol to prevent overly abrupt changes in the target climb rate and turn rate. The second-order filters had the form shown in equation (D1).

$$\frac{1}{As^2 + Bs + 1} \quad (D1)$$

where  $A$  and  $B$  are time constants and  $s$  is the LaPlace operator. The time constants for these filters were separately tuned for the vertical and lateral command paths based on preliminary pilot evaluations. The time constants produced a critically damped second-order behavior with a natural frequency of 1.2 rad/s in the longitudinal path and 0.6 rad/s in the lateral path. The values of the time constants are as follows:

Table D4. Values of Time Constants

Path	$A$	$B$
Vertical	0.70	1.30
Lateral	2.80	2.60

## Performance Tolerances for Flight Director Tracking Task

To compute the task performance for this maneuver, it was necessary to calculate the percentage of time spent with the center of the flight-path marker symbol within  $1^\circ$  and within  $2^\circ$  of the center of the flight director symbol. The flight director symbol consisted of two concentric circles centered on the flight director command as shown in figure D4. The inner circle had a radius of  $1.25^\circ$  and the outer circle had a radius of  $2.25^\circ$ . Desired performance for the flight director tracking task required that the pilot maintain the entire flight-path marker inside the inner circle ( $1.25^\circ$  radius) for at least 70 percent of the duration of the task. Adequate performance required that the pilot maintain the entire flight-path marker inside the blue ( $2.25^\circ$  radius) for at least 90 percent of the duration of the task. The task performance was computed based on the pilot's flight-path command symbol (the output from his stick integrator which appears on the HUD) and not the actual flight path of the vehicle. Therefore, this task provided an indication of the pilot's ability to issue precise maneuver control inputs in the presence of aeroelastic disturbances.

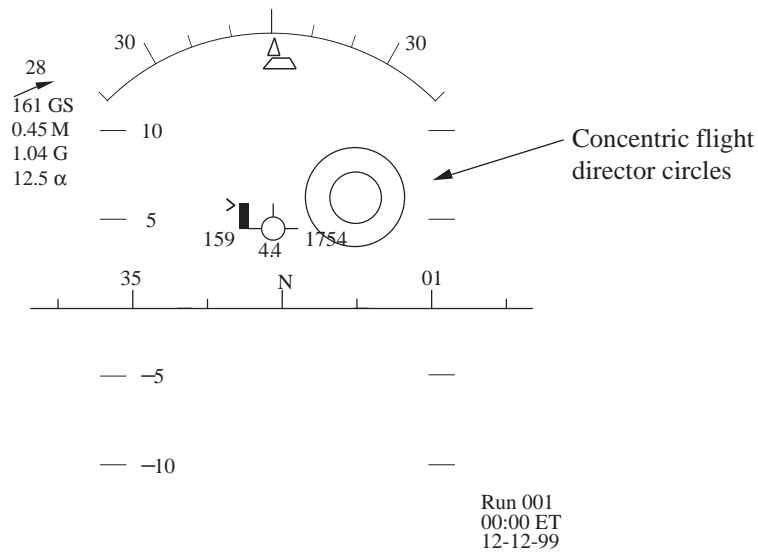


Figure D4. Flight director symbol.

## References

1. Jackson, E. Bruce; Raney, David L.; Hahne, David E.; Derry, Stephen D.; and Glaab, Louis J.: *Reference H Piloted Assessment (LaRC.1) Pilot Briefing Guide*. NASA/TM-1999-209533, 1997.
2. Waszak, Martin R.; Davidson, John B.; and Schmidt, David K.: *A Simulation Study of the Flight Dynamics of Elastic Aircraft—Volumes I and II*. NASA CR-4102, 1987.
3. Churchill, Brett, et al.: High Speed Civil Transport Reference H—Cycle 3 Simulation Data Base. Contract NAS1-20220, Assignment No. 36, WBS 4.3.5.1.2.1, June 1996.
4. Kraft, Raymond; Duffy, Keith S.; Coleman, Edward E.; and Shaw, John L.: *Flight Control System for NASA Simulation*. HSCT-BE49B-L95-013,14 (Contract NAS1-20220), Boeing Co., Aug. 18, 1995.
5. Williams, T. M.; Griffith, M. J.; and Rossitto, K. F.: Description of Lateral-Directional SCAS Control Laws for Ref. H Assessment. Contract NAS1-20220, McDonnell Douglas Aerospace, August 1995.
6. Shweyk, Kamal M.; and Rossitto, Ken F.: Roll Performance and Criteria Development and HSCT Lateral Control Issues. Rep. No. CRAD-9408-TR-3729 (Contract NAS1-20220), Boeing Co., Feb. 6, 1998.
7. Davidson, J. B., Jr.: Lateral-Directional Eigenvector Flying Qualities Guidelines and Gain Weighted Eigenspace Assignment Methodology. Ph.D. Thesis, Purdue Univ., May 1997.
8. Bailey, R. E.; and Knotts, L. H.: *Interaction of Feel System and Flight Control System Dynamics on Lateral Flying Qualities*. NASA CR-179445, 1990.
9. Cooper, George E.; and Harper, Robert P., Jr.: *The Use of Pilot Rating in the Evaluation of Aircraft Handling Qualities*. NASA TN D-5153, 1969.
10. Bailey, Melvin L., ed.: *Pilot Comments From the Boeing High Speed Research Aircraft, Cycle 3, Simulation Study of the Effects of Aeroservoelasticity (LaRC.3)*, NASA/CR-2000-210307, 2000.
11. Parrish, Russell V.; Dieudonne, James E.; Martin, Dennis J.; and Copeland, James L.: *Compensation Based on Linearized Analysis for a Six-Degree-of-Freedom Motion Simulator*. NASA TN D-7349, 1973.
12. Ashkenas, I. L.; Magdaleno, R. E.; and McRuer, D. T.: *Flight Control and Analysis Methods for Studying Flying and Ride Qualities of Flexible Transport Aircraft*. NASA CR-172201, 1983.
13. Smith, John W.; and Montgomery, Terry: *Biomechanically Induced and Controller Coupled Oscillations Experienced on the F-16XL Aircraft During Rolling Maneuvers*. NASA TM-4752, 1996.
14. Ray, Jim; and Rossitto, Ken: HSCT Flight Control System Requirements Specification. NASA Contract NAS1-20220, Boeing Co., Oct. 31, 1997.

REPORT DOCUMENTATION PAGE			Form Approved OMB No. 0704-0188		
<p>The public reporting burden for this collection of information is estimated to average 1 hour per response, including the time for reviewing instructions, searching existing data sources, gathering and maintaining the data needed, and completing and reviewing the collection of information. Send comments regarding this burden estimate or any other aspect of this collection of information, including suggestions for reducing this burden, to Department of Defense, Washington Headquarters Services, Directorate for Information Operations and Reports (0704-0188), 1215 Jefferson Davis Highway, Suite 1204, Arlington, VA 22202-4302. Respondents should be aware that notwithstanding any other provision of law, no person shall be subject to any penalty for failing to comply with a collection of information if it does not display a currently valid OMB control number.</p> <p><b>PLEASE DO NOT RETURN YOUR FORM TO THE ABOVE ADDRESS.</b></p>					
1. REPORT DATE (DD-MM-YYYY)		2. REPORT TYPE		3. DATES COVERED (From - To)	
10-2002		Technical Publication			
4. TITLE AND SUBTITLE Simulation Study of Impact of Aeroelastic Characteristics on Flying Qualities of a High Speed Civil Transport			5a. CONTRACT NUMBER		
			5b. GRANT NUMBER		
			5c. PROGRAM ELEMENT NUMBER		
6. AUTHOR(S) Raney, David L.; Jackson, E. Bruce; and Buttrill, Carey S.			5d. PROJECT NUMBER		
			5e. TASK NUMBER		
			5f. WORK UNIT NUMBER 537-08-23-21		
7. PERFORMING ORGANIZATION NAME(S) AND ADDRESS(ES) NASA Langley Research Center Hampton, VA 23681-2199			8. PERFORMING ORGANIZATION REPORT NUMBER L-18157		
9. SPONSORING/MONITORING AGENCY NAME(S) AND ADDRESS(ES) National Aeronautics and Space Administration Washington, DC 20546-0001			10. SPONSOR/MONITOR'S ACRONYM(S) NASA		
			11. SPONSOR/MONITOR'S REPORT NUMBER(S) NASA/TP-2002-211943		
12. DISTRIBUTION/AVAILABILITY STATEMENT Unclassified - Unlimited Subject Category 08 Availability: NASA CASI (301) 621-0390      Distribution: Standard					
13. SUPPLEMENTARY NOTES Raney, Jackson, and Buttrill, Langley Research Center An electronic version can be found at <a href="http://techreports.larc.nasa.gov/ltrs/">http://techreports.larc.nasa.gov/ltrs/</a> or <a href="http://techreports.larc.nasa.gov/cgi-bin/NTRS">http://techreports.larc.nasa.gov/cgi-bin/NTRS</a>					
14. ABSTRACT A piloted simulation study conducted in NASA Langley's Visual Motion Simulator addressed the impact of dynamic aero-servoelastic effects on flying qualities of a High Speed Civil Transport. The intent was to determine effectiveness of measures to reduce the impact of aircraft flexibility on piloting tasks. Potential solutions examined were increasing frequency of elastic modes through structural stiffening, increasing damping of elastic modes through active control, elimination of control effector excitation of the lowest frequency elastic modes, and elimination of visual cues associated with elastic modes. Six test pilots evaluated and performed simulated maneuver tasks, encountering incidents wherein cockpit vibrations due to elastic modes fed back into the control stick through involuntary vibrations of the pilot's upper body and arm. Structural stiffening and compensation of the visual display were of little benefit in alleviating this impact, while increased damping and elimination of control effector excitation of the elastic modes both offered great improvements when applied in sufficient degree.					
15. SUBJECT TERMS Supersonic transport; Flying qualities; Cockpit vibration; Structural model control; Mode suppression; Ride quality; Biodynamic coupling					
16. SECURITY CLASSIFICATION OF:			17. LIMITATION OF ABSTRACT	18. NUMBER OF PAGES	19a. NAME OF RESPONSIBLE PERSON
a. REPORT	b. ABSTRACT	c. THIS PAGE			STI Help Desk (email: <a href="mailto:help@sti.nasa.gov">help@sti.nasa.gov</a> )
U	U	U	UU	92	19b. TELEPHONE NUMBER (Include area code) (301) 621-0390